Abschlußbericht

BMBF-Verbundvorhaben
Sonderprogramm Geotechnologien
TIPTEQ Teilprojekt 7 - Geothermie

Förderkennzeichen 03G0594F

H. Villinger M. Heesemann

Februar 2008

Fachbereich Geowissenschaften
Universität Bremen

Inhaltsverzeichnis

Abbildungsverzeichnis

Tabellenverzeichnis

1 Einleitung

Das Teilprojekt Geothermie ist eingebunden in das Verbundvorhaben TIPTEQ des BMBF, das im Rahmen des Sonderprogramms Geotechnologien die Untersuchung der Subduktionszone im Bereich des aktiven Kontinentrandes vor Südchile zum Ziel hatte.

Subduktionszonen sind Schlüsselregionen der Plattentektonik. In ihnen findet der energetisch größte Teil der seismischen Aktivität der Erde statt, verbunden mit verheerenden Erdbeben, die sich dabei in relativ geringen Tiefen von weniger als 35-40 km in der Scherzone zwischen der subduzierten Kruste und dem überfahrenden Block ereignen. Dieser Abschnitt einer Subduktionszone wird als Seismogene Zone bezeichnet. In diesen geringen Tiefen werden Erdbeben durch Spannungen und Bruchprozesse im spröden Gestein gesteuert. Mit zunehmender Tiefe wird das Gestein erwärmt und verformt sich plastisch (T > 350-450°C). In geringen Tiefen wird die Scherzone zwischen den Platten durch Tonminerale geschmiert, so dass ein nahezu reibungsfreies Gleiten erfolgt (T < 100-150°C). Tektonische Erdbeben ereignen sich deshalb nur in einem begrenzten „Fenster“, dessen Lage primär durch die Temperatur in der Scherzone gesteuert wird (*Hyndman et al.*, 1995; *Oleskevich et al.*, 1999). Mit den geplanten Untersuchungen soll geklärt werden, inwieweit sich die unterschiedlichen Krustenalter der vor Südchile abtauchenden (subduzierten) ozeanischen Platte auf thermische Strukturen und Prozesse innerhalb der Subduktionszone auswirken.

Ziel der wissenschaftlichen Arbeiten im Teilprojekt Geothermie ist die Untersuchung der Einflussnahme der thermischen Struktur der in die Subduktionszone einfahrenden ozeanischen Lithosphäre auf die Geometrie und Struktur der Subduktionszone und der Lage der seismogenen Zone des chilenischen Kontinentalrandes. Um dieses Ziel zu erreichen sind geothermische Messungen sowohl auf der ozeanischen Platte seewärts des Tiefseegrabens als auch im Fore-Arc Bereich geplant. Der Schwerpunkt der Arbeiten liegt in drei unterschiedlichen Arbeitsgebieten. Die Korridore liegen bei 38°S auf ca. 30 Mio. Jahre alter Kruste (Korridor 1), bei 43°S auf ca. 15 Mio. Jahre alter Kruste (Korridor 2) und nördlich des Tripelpunktes bei 45°S auf ca. 7 Mio. Jahre alter Kruste (Korridor 3). Bedingt durch die großen Altersunterschiede der subduzierten Kruste und die thermischen Steuerungsgrößen der seismogenen Zone sollte sich die Lage der seismogenen Kontaktzone von Süden nach Norden landwärts verlagern. Zusätzliche Messungen südlich der Chile Triple Junction (CJT) sollen den Einfluss der erfolgten Subduktion des Chile Rückens auf das thermische Regime des Kontinentalrandes erkunden.

Alle thermischen Messungen werden analysiert, interpretiert und zusammengestellt und dann dazu verwendet, Randbedingungen für die Berechnung der thermische Modelle in der subduzierten Lithosphäre zu liefern. Die für die Berechnung der thermischen Tiefenstruktur notwendigen strukturellen Informationen werden den seismischen und seismologischen Datensätzen entnommen. Gemeinschaftlich können die kombinierten Datensätze dazu genutzt werden, um die Bedeutung thermischer und struktureller Steuerungsgrößen zu evaluieren.

2 Expeditionsdurchführung

Die geothermischen und reflexionsseimischen Messungen wurden während der Expedition SO181-1b vom 18.12.2004 bis 16.1.2005 mit dem Forschungsschiff FS SONNE durchgeführt. Insgesamt wurden 67 erfolgreiche Wärmestromdichtemessungen und vier reflexionsseismische Vermessungen von insgesamt ca. 870 km Länge durchgeführt. Die technische Durchführung der Messungen verlief ohne Probleme, nur war die Qualität der seismischen Registrierungen wetterbedingt teilweise nicht optimal. Unsere Versuche, Wärmestromdichtemessungen möglichst weit landwärts der Deformationszone den Kontinentalhang hinauf durchzuführen, waren zum großen Teil nicht von Erfolg gekrönt, da sehr wahrscheinlich aufgrund erosiver Prozesse das oberflächennah anstehende Sediment sehr sandig war und ein Eindringen der Wärmestromdichtesonde verhinderte. Dasselbe Schicksal erlitten die Kollegen der marinen Geologie, die auf demselben Fahrtabschnitt mit Hilfe eines Schwerelotes den Kontinentalhang beproben wollten: auch sie hatten große Probleme, erfolgreich Kerne zu ziehen. Details über die Expeditionsdurchführung wie Erläuterungen der verwendeten Messgeräte, technische Details der Vermessungen und erste Ergebnisse sind dem Fahrtbericht (*Flueh and Grevemeyer*, 2005) zu entnehmen.

In den Abbildungen 2.1 und 2.2 ist die plattentektonische Situation und die Lage der seismischen Profile eingezeichnet.

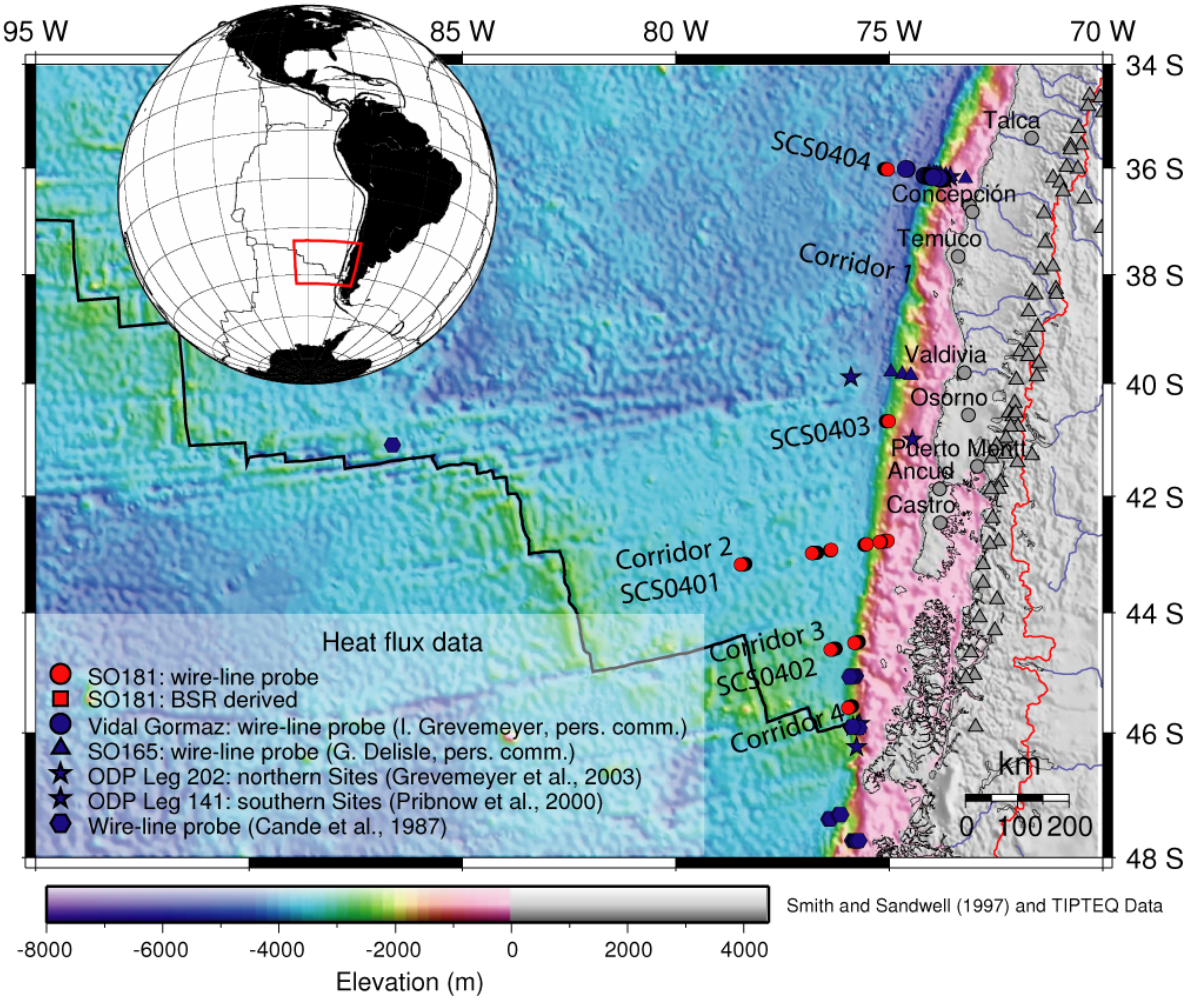

Abbildung 2.1: Wärmestromdichtemessungen im TIPTEQ-Untersuchungsgebiet und Bathymetrie von *Smith and Sandwell* (1997). Das Gebiete wurde von Nord nach Süd in die Korridore 1-4 aufgeteilt, in denen ozeanische Kruste mit unterschiedlichem Alter subduziert wird. Die blauen Symbole repräsentieren die wenigen Wärmestromdichtedaten (*Grevemeyer et al.*, 2005, 2003; *Pribnow et al.*, 2000; *Cande et al.*, 1987), die vor dem TIPTEQ Projekt zur Verfügung standen. Rote Kreise bezeichnen insitu-Wärmestromdichtemessungen, die während der Ausfahrt SO181-1b durchgeführt wurden. Alle neuen Daten liegen auf in Abb. 2.2 markierten reflexionsseismischen Profilen (vgl. auch Tab. A.1, A.2 im Anhang).

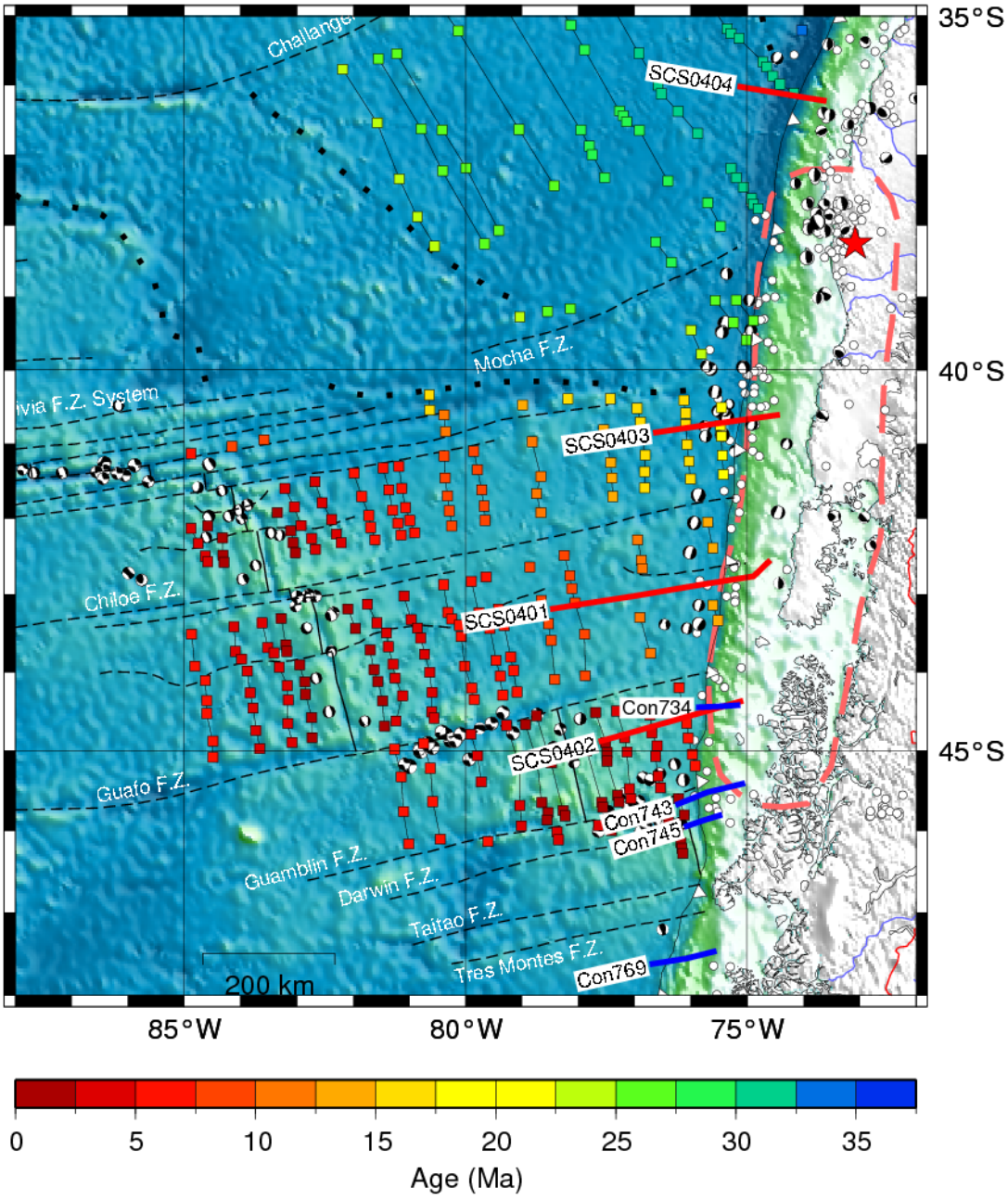

Abbildung 2.2: Bathymetrie aus Fächerlotdaten und von *Smith and Sandwell* (1997) im Untersuchungsgebiet. Das gestrichelte Oval zeigt die Region mit Hebungen und Senkungen (*Plafker and Savage*, 1970), die vom Erdbeben 1960 verursacht wurden. Der rote Stern markiert die Lokation des Epizentrums. Weitere Erdbeben aus Katalogen mit einer Magnitude größer 5 sind als weiße Kreise (ANSS) and Herdflächenlösungen (Harvard) dargestellt. Die farbigen Quadrate zeigen das Alter (siehe Farbskala) der ozeanischen Kruste, das von *Tebbens and Cande* (1997) aus magnetischen Anomalien bestimmt wurde. Weiterhin sind reflexionsseismischen Linien, die während der Fahrt SO-181-1b aufgezeichnet wurden (SCS; rote Linien) und die in *Brown et al.* (1996) beschriebenen Linien (Con; blaue Linien) eingezeichnet.

3 Wissenschaftliche Ergebnisse

3.1 Wärmestromdichtemessungen

Während der Expedition SO181b wurden zwei verschiedene Wärmestromdichtesonden (Typ Violinenbogen nach *Hyndman et al.* (1979)) benutzt: ein 3m lange Sonde und eine 6 m lange Sonde (*Flueh and Grevemeyer*, 2005). Die Messungen erfolgten auf den vermessenen seismischen Profilen im Abstand von ca. 1 km. Die Rohdaten wurden mit dem Programm T2C (*Hartmann and Villinger*, 2002) prozessiert und dargestellt. Die an Bord erfolgte erste Auswertung (siehe *Flueh and Grevemeyer* (2005)) wurde durch ein Nachprozessieren der Daten verfeinert und Schusspunkten auf den entsprechenden seismischen Linien zugeordnet. Die endgültigen Wärmestromdichten sind in Tabelle A.2 im Anhang zu finden.

In Abbildung 3.1 sind zusammenfassend die Wärmestromdichtewerte aller vermessener Profile dargestellt. Im oberen Teil der Abbildung sind alle Werte seewärts, im unteren Teil die Werte landwärts der Deformationsfront gezeigt. Die Farbkodierung kennzeichnet das Alter der ozeanischen Kruste, auf dem die Werte gemessen wurden.

Folgende Schlussfolgerungen lassen sich ziehen:

- Konduktive Abkühlungsmodelle, durch farbige Linien in Abbildung 3.1 gekennzeichnet, überschätzen zumeist die gemessenen Werte, da in den Modellen advektive Kühlung durch zirkulierendes Seewasser nicht berücksichtigt wird; dies ist besonders ausgeprägt bei Station H0402 (Krustenalter ca 15 Mio Jahre), wo durch das Eindringen von kaltem Meerwasser in den Untergrund der Wärmestrom auf Werte um 7 mW/m^2 erniedrigt wird (vgl. Abschnitt 3.3.2).

- Die direkt im Tiefseegraben gemessenen Werte sind signifikant niedriger als aufgrund eines konduktiven Abkühlungsmodell zu erwarten wäre. Dies wird verursacht durch die hohen Sedimentationsraten im Graben, die zu einer Verminderung des Oberflächenwärmestromes führen. Eine Sedimentationskorrektur ist jedoch nur möglich, wenn die Sedimentationsrate und die Zeitdauer der Sedimentation bekannt sind. Da beide Größen nicht zur Verfügung stehen, konnte eine solche Korrektur nicht durchgeführt werden.

- Unsere Versuche, Wärmestromdichtemessungen möglichst weit landwärts der Deformationszone den Kontinentalhang hinauf durchzuführen, waren zum großen Teil nicht von Erfolg gekrönt, da sehr wahrscheinlich aufgrund erosiver Prozesse das oberflächennah anstehende Sediment sehr sandig war und ein Eindringen der Wärmestromdichtesonde verhinderte. Daher gibt es nicht auf allen Profilen wie eigentlich aus wissenschaftlicher Sicht notwendig genügend Messungen auf dem Kontinentalhang, die als Randbedingungen für die Modellierung wichtig sind.

- Die gemessenen Wärmestromdichten wurden ergänzt durch aus BSR-Tiefen abgeleiteten Werten, die nach *Kaul et al.* (2000) berechnet wurden. Wie bei den Modellierungen

(siehe Abb. 3.12) zu sehen stimmen die abgeleiteten Werte sehr gut mit den gemessenen Werten überein.

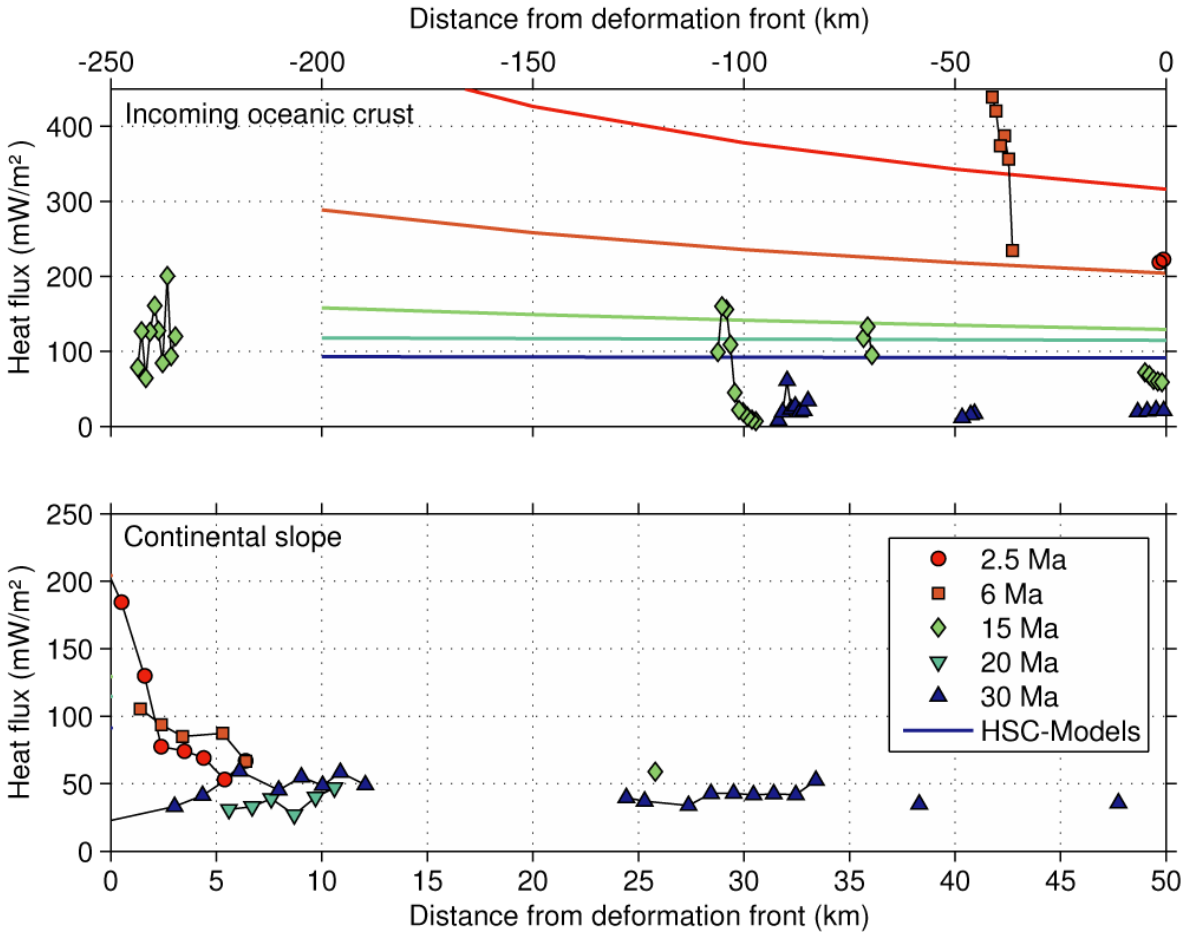

Abbildung 3.1: Übersicht über alle Wärmestromdichtemessungen, die während der Ausfahrt SO181-1b durchgeführt wurden. Es wurden sowohl Daten seewärts der Deformationsfront (oben) als auch am Kontinentalhang (unten) gewonnen. Konduktive Abkühlungsmodelle (*Stein and Stein*, 1992), durch farbige Linien gekennzeichnet, überschätzen zumeist die gemessenen Werte, da advektive Kühlung durch zirkulierendes Seewasser vernachlässigt wird.

3.2 Reflexionsseimische Profile

Die reflexionsseismischen Daten wurden nach Abschluss der Expedition mit Hilfe des Software-Paketes SU (*Cohen and Stockwell Jr.*, 2007) prozessiert. Die einzelnen Prozessingschritte waren:

- Schussnavigation, basierend auf GPS-basierter Schiffsnavigation erstellen
- manuelles Editieren von fehlerhaften Schüsse
- Stack aller 16 Kanäle
- Filterung der Daten
- Auffüllen fehlender Schüsse mit Null-Spuren
- Migration im Zeitbereich
- Darstellung
- Digitalisierung von Sediment- und Basementoberkanten und bodensimulierenden Reflektoren

Die Abbildungen 3.2 bis 3.9 zeigen die Ergebnisse der seismischen Vermessungen. Wegen der Länge der Profile sind sie jeweils in zwei Teile geteilt: der erste Teil umfasst das Profil seewärts der Deformationsfront bis hin zur Deformationsfront, der zweite Teil überdeckt erstreckt sich von der Deformationsfront landwärts den Kontinentalhang hinauf. Allen Profilen gemeinsam sind folgende Beobachtungen:

- Auf allen Profilen ist seewärts des Grabens die Grenze Sediment-Basement klar zu erkennen. Stellenweise wird die Sedimentbedeckung durch Seamounts durchbrochen; an diesen Stellen ist ein direkter Austausch zwischen Ozean und oberer Kruste möglich. Die Sedimentmächtigkeiten auf diesen Profilen sind wichtige Randbedingungen für die Interpretation der refraktionsseismischen Messungen, die vom IfM-GEOMAR seewärts der Deformationsfront durchgeführt wurden.
- Die Grabenfüllung ist auf allen Profilen klar abgebildet; deutlich zu erkennen sind kleinräumige tektonische Störungen wie z.B. auf Profil SCS0401 (Abb. 3.3). Diese Informationen haben Eingang in *Contreras-Reyes et al.* (2007) (siehe Anhang ab Seite 85) gefunden. Die Mächtigkeit der Grabenfüllung beträgt unter Einbeziehung von Geschwindigkeitsinformationen aus der Refraktionsseismik bis zu 2 km.
- Die Deformationsfront ist auf allen Profilen klar identifizierbar. Landwärts der Deformationsfront werden die sedimentären Strukturen am Meeresboden nur noch oberflächennah aufgelöst. Verantwortlich dafür ist höchstwahrscheinlich der hohe Impedanzkontrast am Meeresboden, der mit dem Wechsel von tonreichen (seewärts der Deformationsfront) zu tonärmeren (und damit sandigeren) Sedimenten auf dem Kontinentalhang einher geht. Ein Indiz dafür ist die teilweise sehr kräftig ausgeprägte Multiple (siehe z.B. Abb. 3.4).

- Ein BSR konnte auf allen vier Profilen identifiziert werden. Am klarsten zu sehen ist er auf Profil SCS0402 (Abb. 3.4 bei Schusspunkt 1700 (ca. 0.25 s TWT unterhalb des Meeresbodens). Die Tiefenlage des BSR wurde auf allen Profilen erfasst und zur Abschätzung des Wärmestromes herangezogen (z.B. *Grevemeyer and Villinger* (2001) und *Kaul et al.* (2000).

Zusätzlich zu den während der Expedition vermessenen Linien wurde seismische Vermessungen in die Interpretation eingezogen, die von während der RV Conrad Reise C2901 (*Bangs and Cande*, 1997) im Zusammenhang mit den Vorbereitungen für ODP-Leg 141 geschossen wurden. Auch auf diesen Profilen ist ein BSR zu erkennen und auswertbar (siehe Abb. B.1, B.2).

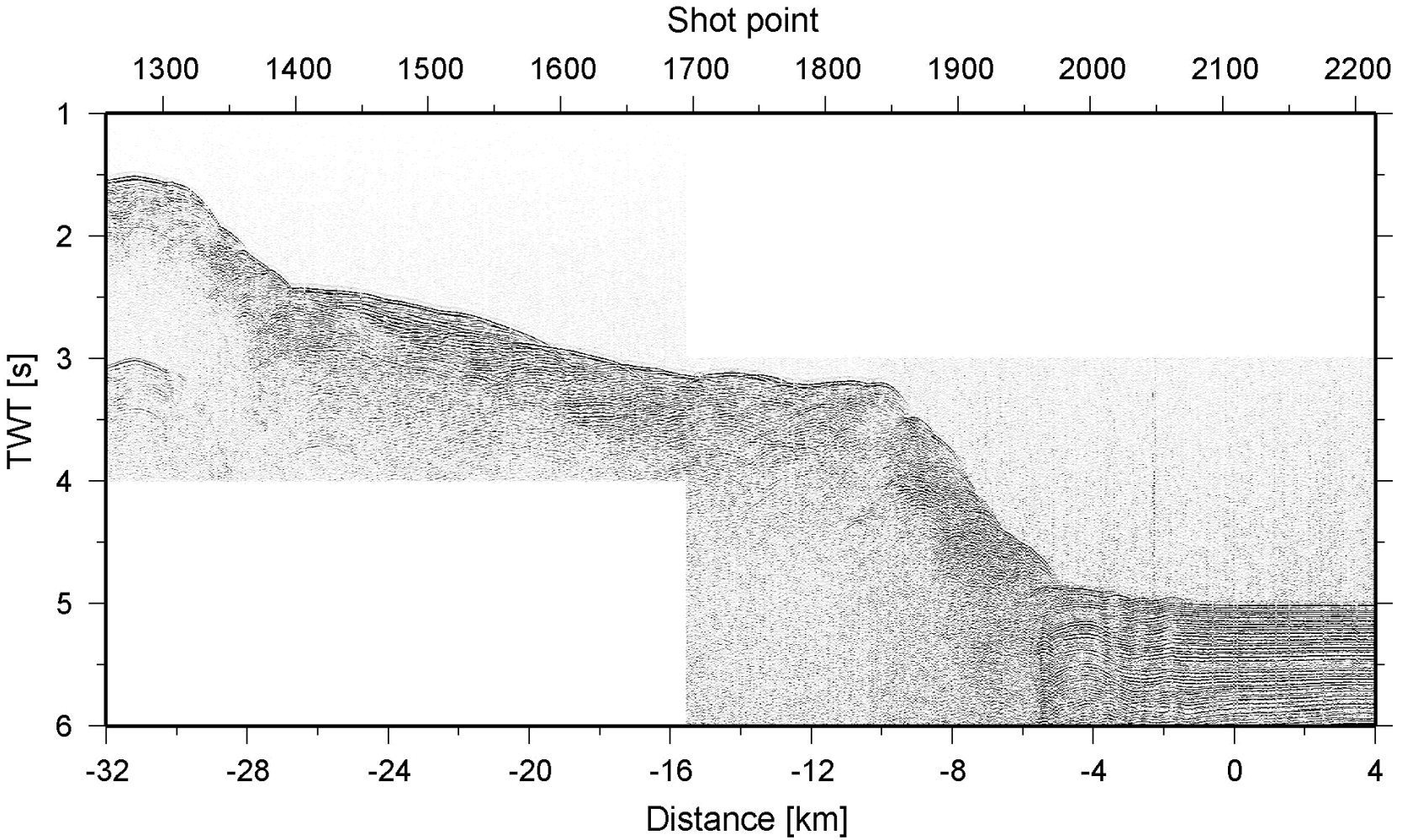

Abbildung 3.2: Reflexionsseismische Daten Profil SCS0401 am Kontinentalhang landwärts der Deformationsfront. Die Lage des Profils ist der Abbildung 2.2 entnehmen.

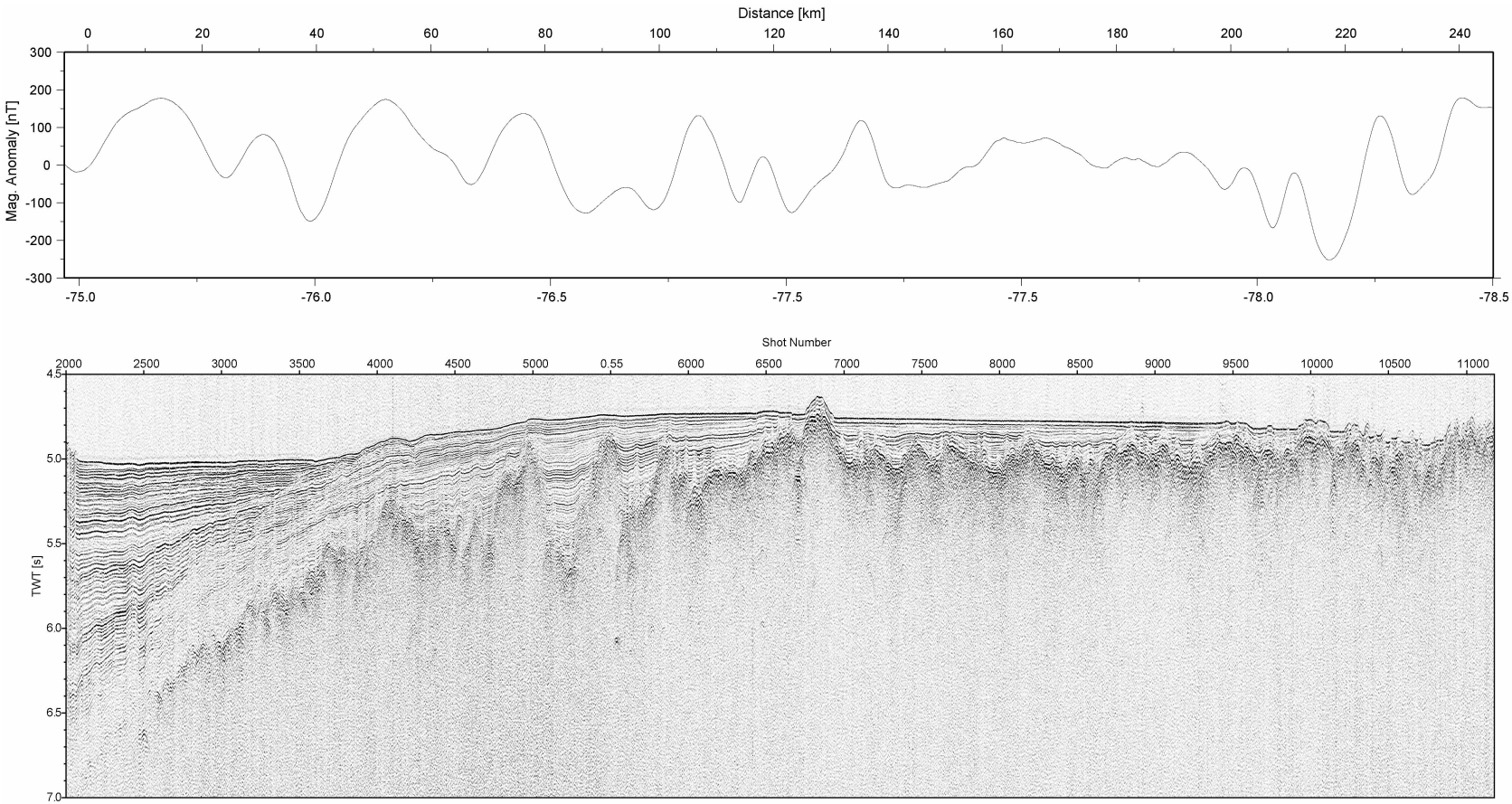

Abbildung 3.3: Reflexionsseismische Daten SCS0401 und magnetische Anomalien seewärts der Deformationsfront. Die Lage des Profils ist der Abbildung 2.2 entnehmen.

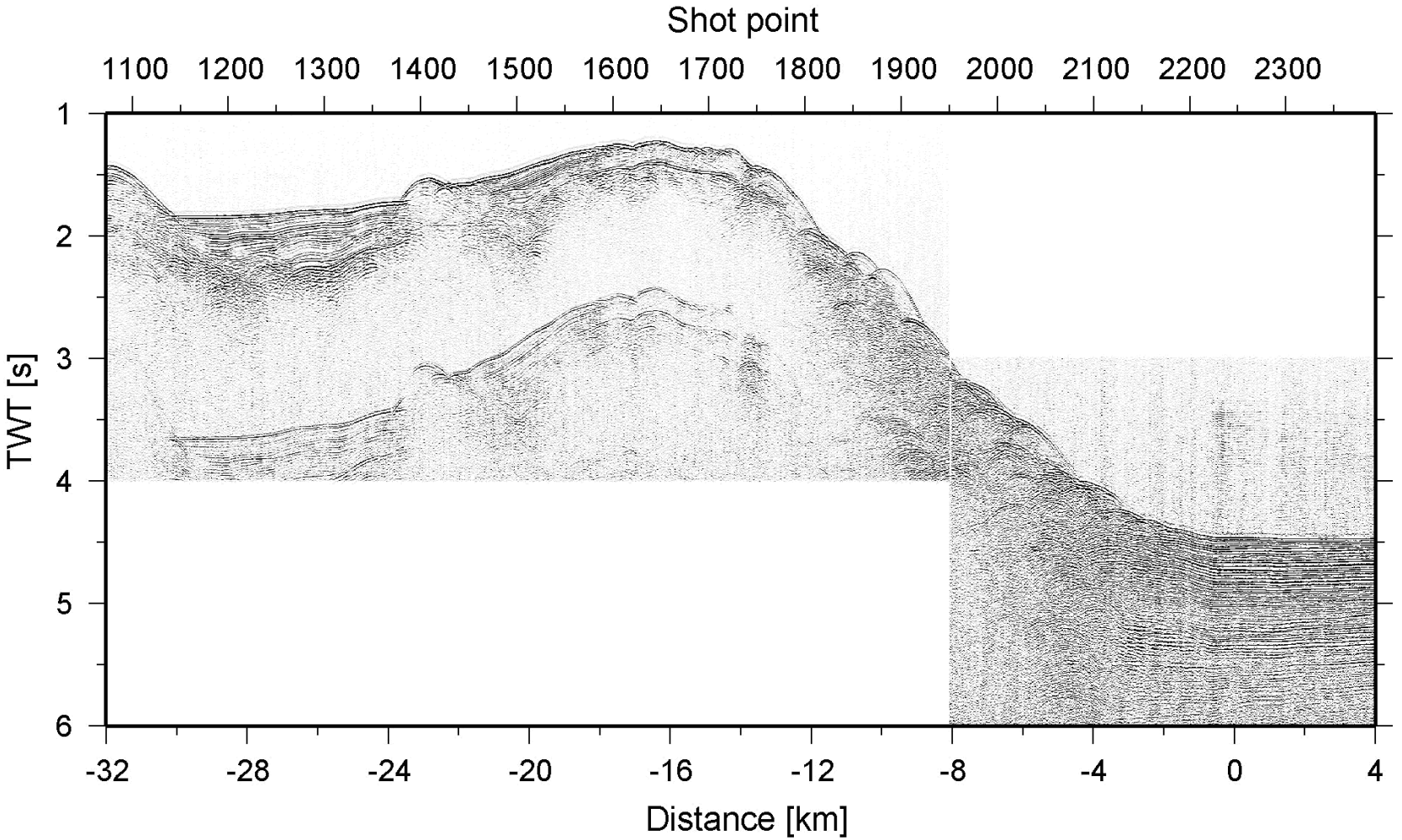

Abbildung 3.4: Reflexionsseismische Daten SCS0402 am Kontinentalhang landwärts der Deformationsfront. Die Lage des Profils ist der Abbildung 2.2 entnehmen.

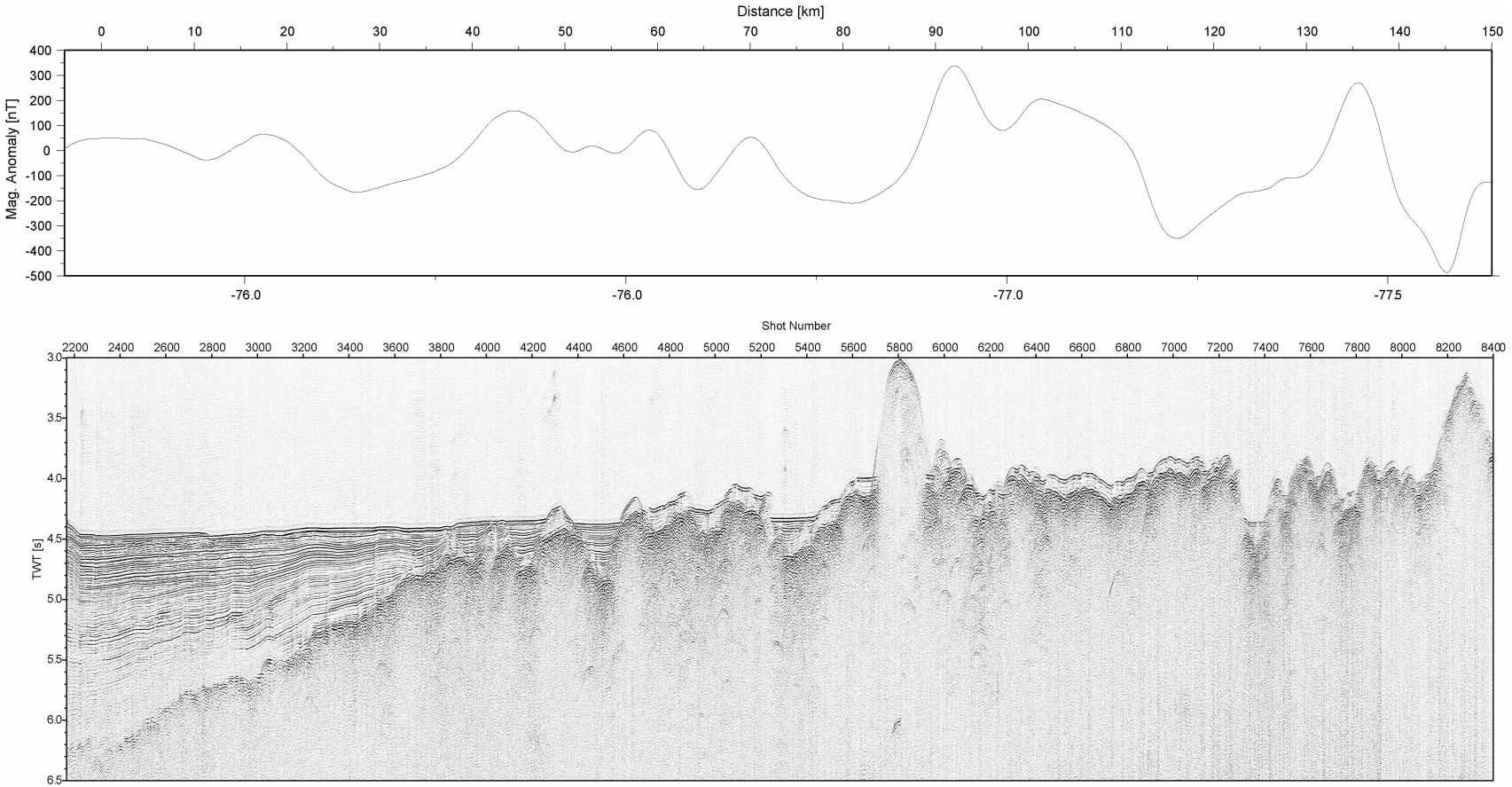

Abbildung 3.5: Reflexionsseismische Daten SCS0402 und magnetische Anomalien seewärts der Deformationsfront. Die Lage des Profils ist der Abbildung 2.2 entnehmen.

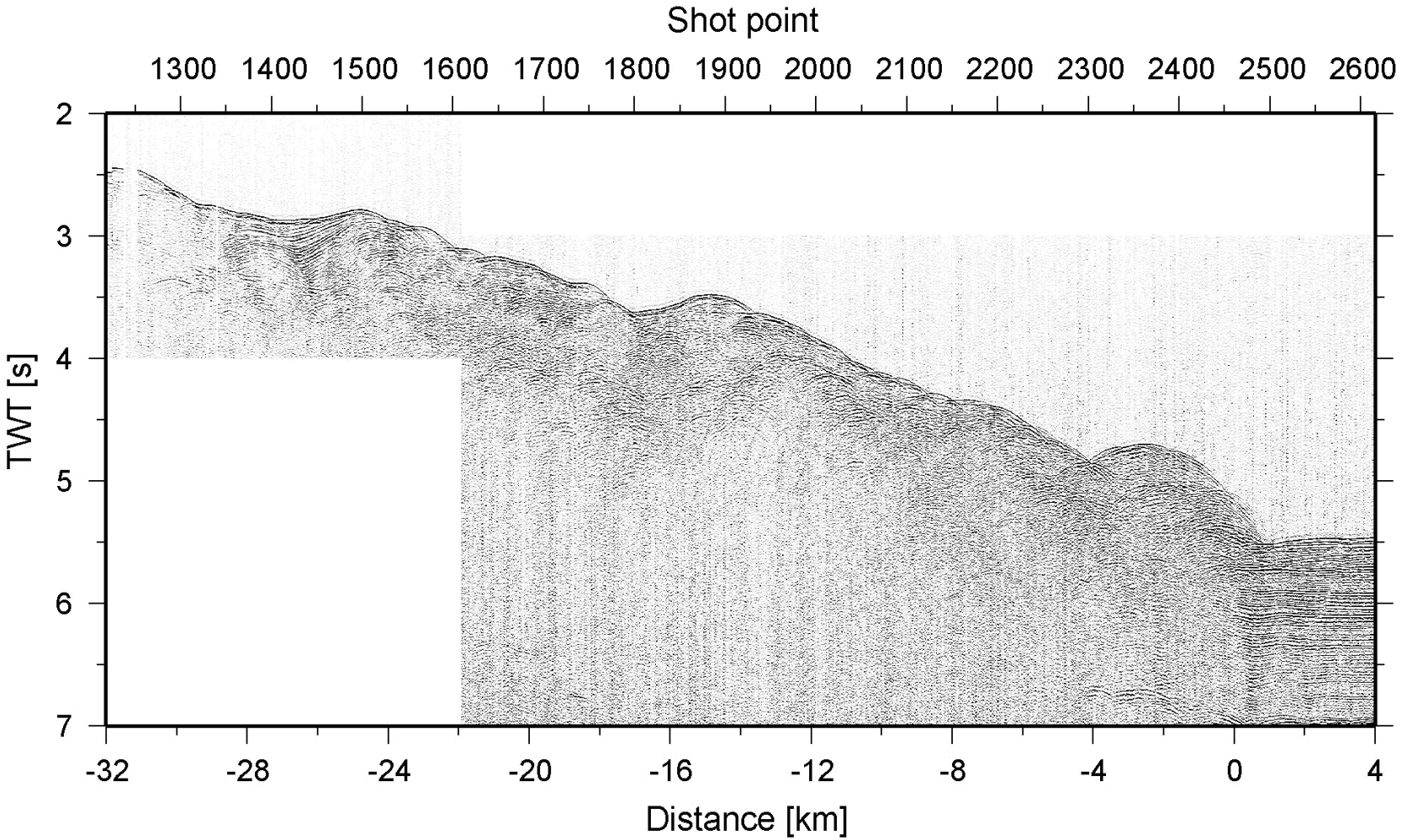

Abbildung 3.6: Reflexionsseismische Daten SCS0403 am Kontinentalhang landwärts der Deformationsfront. Die Lage des Profils ist der Abbildung 2.2 entnehmen.

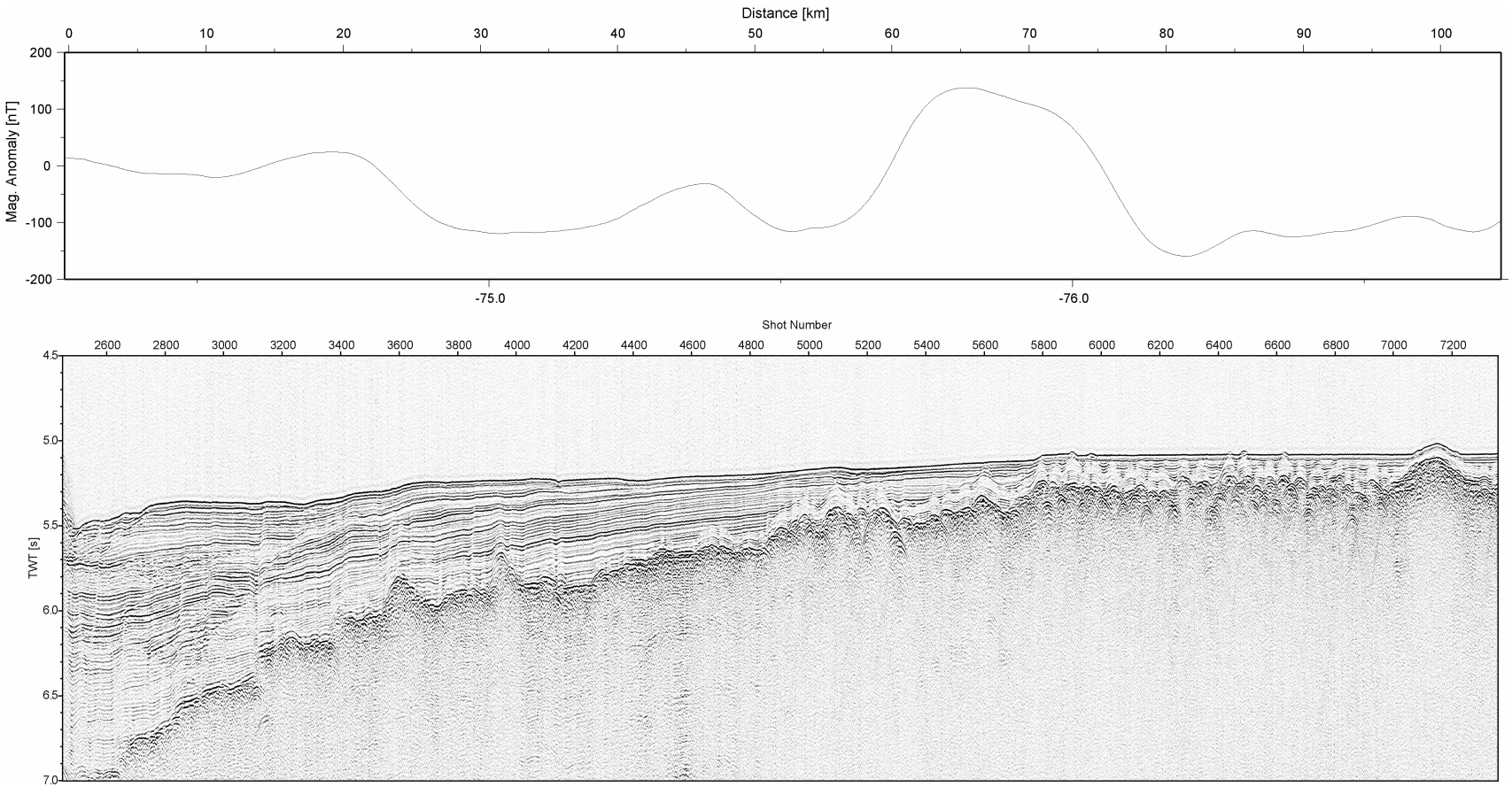

Abbildung 3.7: Reflexionsseismische Daten SCS0403 und magnetische Anomalien seewärts der Deformationsfront. Die Lage des Profils ist der Abbildung 2.2 entnehmen.

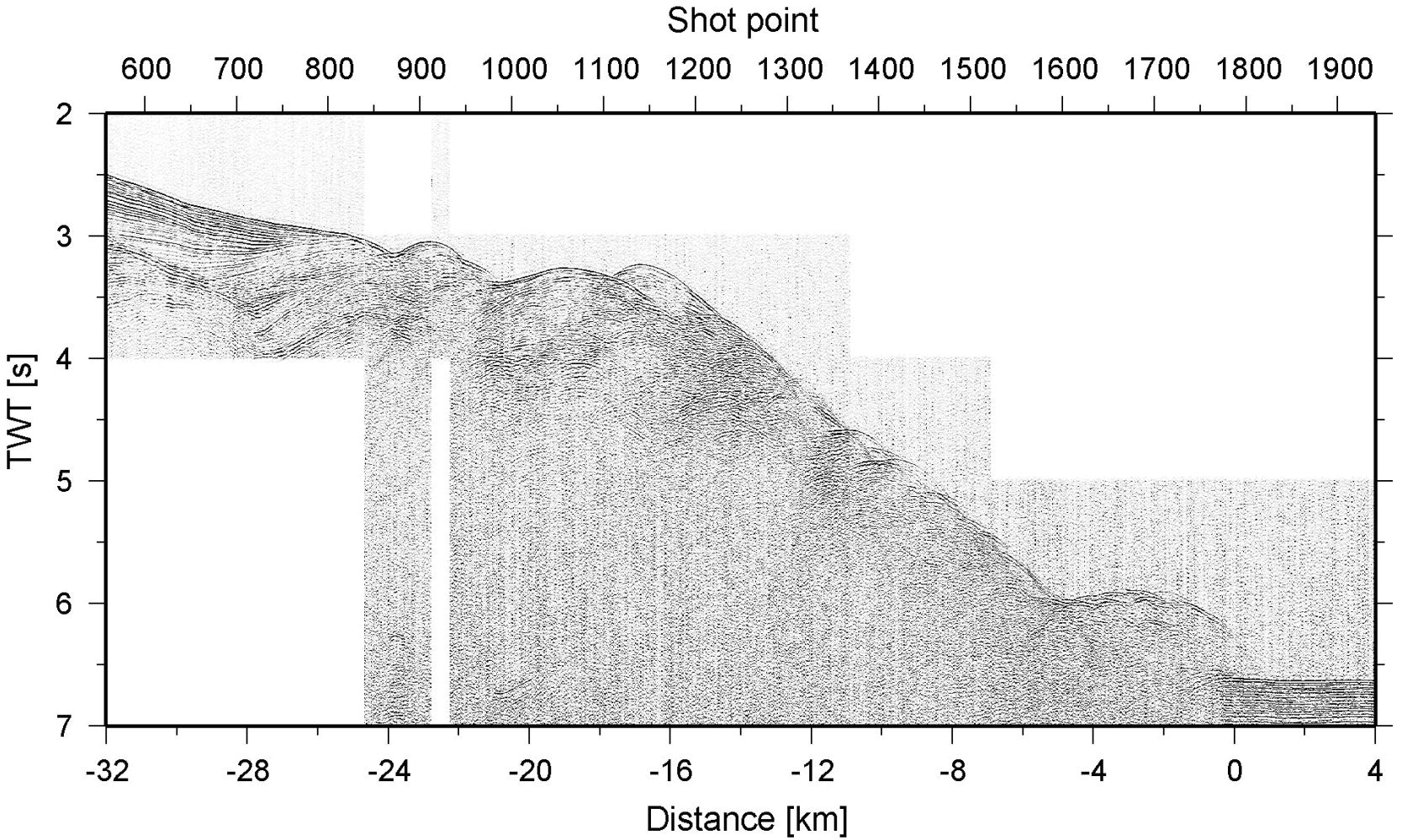

Abbildung 3.8: Reflexionsseismische Daten SCS0404 am Kontinentalhang landwärts der Deformationsfront. Die Lage des Profils ist der Abbildung 2.2 entnehmen.

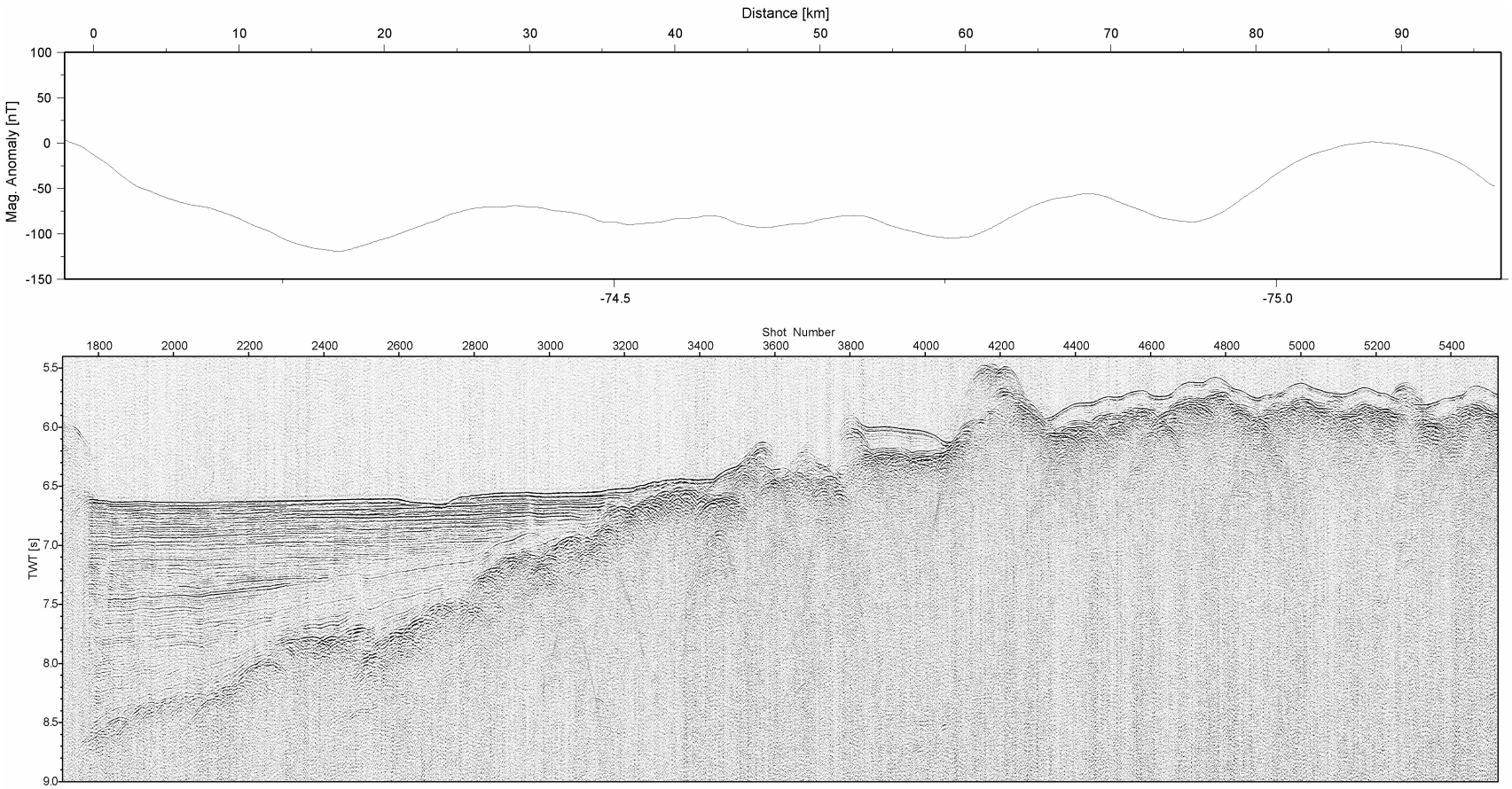

Abbildung 3.9: Reflexionsseismische Daten SCS0404 und magnetische Anomalien seewärts der Deformationsfront. Die Lage des Profils ist der Abbildung 2.2 entnehmen.

3.3 Parameter für Modellierung

Um das Temperaturfeld im oberen Bereich der seismogenen Zone zu berechnen, haben wir ein stationäres Finite Elemente (FE) Modell erstellt, das auf dem FE Softwarepaket Comsol Multiphysics® Toolbox und Matlab® aufbaut. Details zur Implementierung des Modells, das wir auch auf eine ähnliche Fragestellung im Zusammenhang mit Tsunami-Erdbeben vor der Küste Nicaraguas angewendet haben, sind in einer kürzlich eingereichten Veröffentlichung im Anhang ab Seite 55 zu finden.

Das Modell berücksichtigt, abgesehen von dem mit der Konvergenz der abtauchenden Platte zusammen hängenden advektiven Wärmetransport, ausschließlich konduktive Wärmetransport. Daraus ergibt sich, dass die modellierten Temperaturen der Bruchzone von folgenden Parametern abhängt:

- Geometrie der drei Bereiche, in die das Modell unterteilt ist
  - Abtauchende ozeanische Kruste (OcCr)
  - Kontinentales Basement / verfestigte akkretierte Sedimente (CnBs)
  - Unkonsolidierte und semi-konsolidierte Sedimente (Seds)
- Die Randbedingungen an den Außenkanten (West, Ost, oben, unten) des Modells
- Die Wärmeleitfähigkeitsverteilung $k(x, z)$ in allen Unterbereichen
- Die Verteilung der primär radiogenen Wärmeproduktion $Q(x, z)$ in allen Unterbereichen
- Die Geschwindigkeit $\vec{v}$ des OcCr-Bereichs in Bezug auf die anderen Unterbereiche, die als ruhend angenommen werden.
- Die Verteilung der volumetrischen Wärmekapazität $\rho c_p(x, z)$ im OcCr-Bereich

3.3.1 Geometrie der Subduktionszone

Die Geometrien der Modelle ergeben sich im wesentlichen aus den seismischen Geschwindigkeitsmodellen von Martin Scherwath und Eduardo Contreras-Reyes (IfM-GEOMAR, Kiel; siehe Abbildungen B.3 – B.5) und aus Modellen, die aus dem SPOC Projekt (*The SPOC Team and Krawcyzk*, 2003) hervorgingen (Abbildungen B.6 – B.8) sowie der Bestimmung der Tiefenlage der Verwerfung aus Modellierungen des Schwerefelds von *Tassara* (2005).

3.3.2 Randbedingungen

Die Ränder des Modell sind in vier Gruppen mit verschiedenen festgelegten Bedingungen unterteilt:

1. der obere Rand des Seds Bereichs (Sediment – Wasser Kontakt)
2. die landwärtigen (rechten) Begrenzungen aller Bereiche

3. der seewärtige (linke) und untere Rand des OcCr Bereichs

4. der obere Rand des OcCr Bereichs seewärts der sedimentären Grabenverfüllung

Am oberen Rand (1) wird eine konstante Bodenwassertemperatur von 0°C angenommen. Dies entspricht dem allgemeinen Vorgehen für derartige Modellierungen, auch wenn die realen Bodenwassertemperaturen (rezent 2.5°C) geringfügig von dieser Annahme abweichen.

Die konduktive Komponente des Wärmetransports über die landwärtigen (rechten) Rändern (2) wird auf Null gesetzt. Dies spiegelt die Annahme wieder, dass die horizontale Komponente der konduktiven Wärmeflussdichte im Vergleich zur vertikalen Komponente in erster Näherung zu vernachlässigen ist. Dabei können in unmittelbarer Umgebung des Randes unrealistische Modelltemperaturen auftreten. Durch ausgiebige numerische Tests konnte jedoch gezeigt werden, das diese Randeffekte lokal sehr begrenzt sind. Um sicher zu gehen, dass es zu keinen Fehlinterpretationen von numerischen Artefakten kommt, sind bei den Präsentationen der Modellergebnisse die Modelle so am landwärtigen Rand beschnitten, dass nur vertrauenswürdige Daten sichtbar sind.

Die großräumige thermische Struktur der abtauchenden ozeanischen Kruste wird durch den seewärtigen und unteren Rand (3) durch konstante Temperaturen vorgegeben. Diese Temperaturen basieren auf einen globalen Modell für die konduktive Abkühlung von an Spreizungszonen neu gebildeter ozeanischer Kruste von *Stein and Stein* (1992). Dabei hängen die Temperaturen auf dem Rand, neben den thermischen Eigenschaften der Kruste, vom Alter der ozeanischen Kruste und der Tiefe relativ zur Plattenobergrenze ab. Das Modell von *Stein and Stein* (1992) bietet derzeit die beste Abschätzung zur großräumigen thermischen Struktur von ozeanischer Kruste. Ein solches globales Modell kann allerdings die Temperaturentwicklung am oberen Rand der ozeanischen Kruste nicht korrekt wiedergeben, da die ozeanische Kruste in der Realität mit einer Sedimentschicht bedeckt ist und nicht, wie in dem Modell vorausgesetzt, im direkten Kontakt mit dem Seewasser (0°C) steht.

Der thermische Zustand der oberen ozeanischen Kruste ist jedoch einer der wichtigsten Parameter, die das Temperaturfeld einer Subduktionszone in den ersten 100 km landwärts der Deformationsfront bestimmen (*Harris and Wang*, 2002). Da genau dieser Bereich der Subduktionszone im Fokus unserer numerischen Modelle liegt, haben wir die thermische Struktur seewärts der Deformation mit zahlreichen Wärmestromdichtemessungen beprobt. Wie im oberen Teil der Abbildung 3.1 gezeigt, sind die gemessenen Wärmestromdichtewerte systematisch geringer als Vorhersagen des konduktiven Modells. Das liegt daran, dass die poröse obere ozeanische Kruste durch zirkulierendes Seewasser, das z.B. an nur unvollständig mit Sedimenten bedeckten topographischen Erhöhungen eindringen kann, gekühlt wird. Auf Korridor 2 konnten wir ca. 100 km seewärts der Deformationsfront mit unseren Wärmestromdichtemessungen ein solches eindringen von kaltem Seewasser in die obere ozeanische Kruste beobachten (vgl. Abbildung 3.10). Wie in der Abbildung verdeutlicht, ist es möglich aus den Wärmestromdichtemessungen zusammen mit Sedimentmächtigkeiten, die aus den reflektionsseismischen Daten berechneten wurden, auf die Temperatur in der oberen ozeanischen Kruste zu schließen. Die so berechneten Temperaturen fließen in unser Modell ein, in dem wir die nicht nur die Temperatur der Sedimentoberfläche festhalten, sondern auch die Temperatur der oberen ozeanischen Kruste bis zu einem bestimmten Punkt im Graben. D.h. die Oberflächenwärmeströme in unserem Modell seewärts dieses Punktes können sich nicht frei entwickeln, sondern müssen als Randbedingung angesehen werden. Der Punkt, ab dem

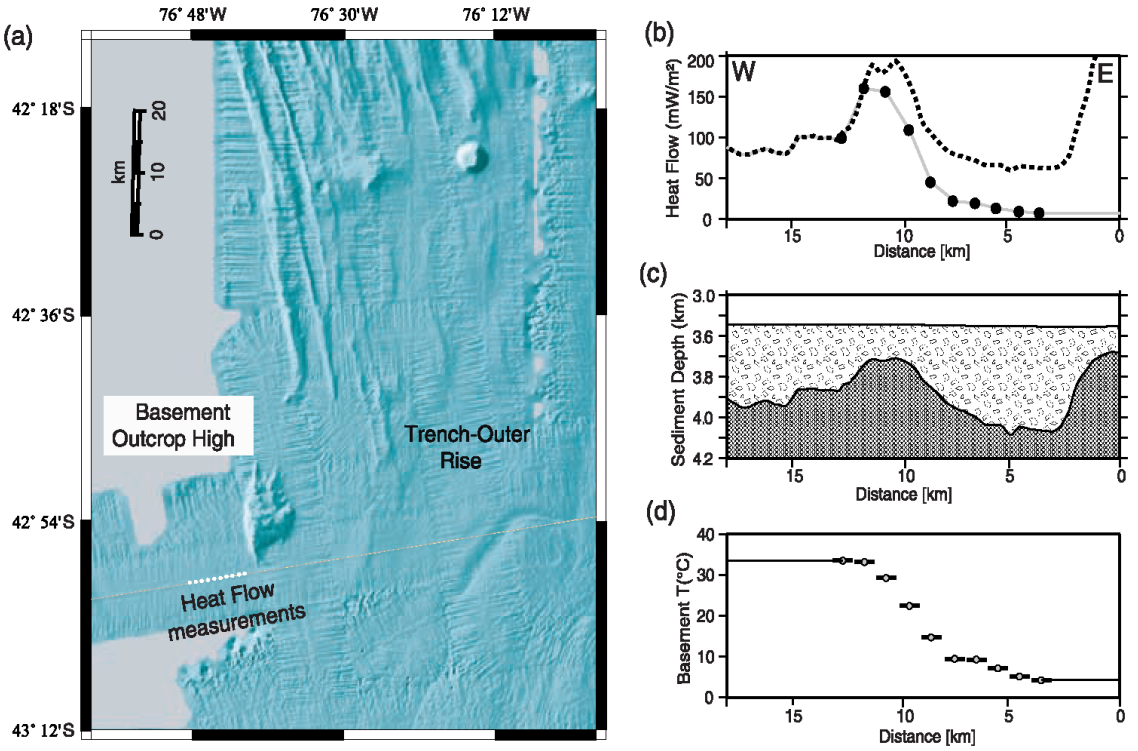

Abbildung 3.10: (a) Lokationen der Wärmestromdichtemessungen der Station H0402 entlang des reflektionsseismischen Profils SCS0401. (b) In der lateralen Änderung der Wärmestromdichte (Punkte) sollte sich bei rein konduktivem Wärmestransport die Basement-Topographie (c) widerspiegeln (gestrichelte Linie). Dabei wird davon ausgegangen, dass der Wärmetransport in den impermeablen Sedimenten im wesentlichen konduktiv ist und dass die Grenzfläche zwischen Sediment und Basement durch zirkulierendes Wasser auf einer konstanten Temperatur gehalten wird. Die Wärmestromdichtemessugen zeigen jedoch, dass sich (d) die Temperatur im oberen Basement der Temperatur des Bodenwassers annähert, je dichter die Messungen an dem Basementhoch liegen, das (a) nordöstlich der Messungen ausbeißt (*Contreras-Reyes et al.*, 2007) (vgl. Anhang ab Seite 85).

die Temperatur der oberen Kruste nicht mehr vorgegeben ist, ist letztendlich ein weiterer Modellparameter. Er wird so gewählt, dass die Sedimentbedeckung im Graben an diesem Punkt mächtig genug ist, um das Eindringen von kaltem Wasser in das Basement zu verhindern.

3.3.3 Konvergenzrate

Die aktuellste Studie zur Konvergenzrate der ozeanischen Nazca Plate relativ zu einer als ruhend angenommen Südamerikanischen Platte ist die von *Kendrick et al.* (2003). Aus dem Eulerpol, der aus langjährigen GPS–Datenreihen bestimmt wurde, haben wir eine rezente Konvergenzrate von ca. 60 mm/a mit einem Azimuth von ca 80° für das TIPTEQ Untersuchungsgebiet berechnet (siehe Tabelle A.3). Der Vergleich mit älteren Studien, die die Konvergenzrate zum Teil auch aus der Datierung des Ozeanbodens über magnetische Anomalien

berechnet haben, zeigt, dass sich die Konvergenzrate über die letzten 10–20 Ma signifikant verlangsamt hat. So liegen z. B. die korrespondierenden Konvergenzraten, die auf dem NUVEL 1A Modell beruhen und basierend auf Informationen der letzten 3 Ma berechnet wurden, bei ca. 80 mm/a (*Kendrick et al.*, 2003). Da unser Modell zeitunabhängig ist, können wir Variationen in der Konvergenzrate, wie auch in allen anderen Parametern, nur über die Wahl von repräsentativen Mittelwerten berücksichtigen.

3.3.4 Wärmeleitfähigkeiten

Da für die meisten Bereiche der Modelle keine Messungen der thermischen Eigenschaften vorliegen, können diese Parameter nur so eingegrenzt werden, dass sie im Rahmen von geophysikalisch sinnvollen Bereichen liegen. Da für alle Korridore detailliert seismische Geschwindigkeiten ermittelt wurden, liegt es nahe, die p-Wellengeschwindigkeit als Proxy für die Wärmeleitfähigkeit zu verwenden, sofern keine direkten Messungen zur Verfügung stehen. Es ist nahe liegend und unmittelbar einleuchtend, dass die Wärmeleitfähigkeit der Gesteine proportional zur Geschwindigkeit ist. Mangels empirischer Untersuchungen der Abhängigkeit $k(v_p)$ wird ein linearer Zusammenhang angenommen (Occam's Razor).

Für den Seds-Bereich liegen im Untersuchungsgebiet Wärmeleitfähigkeiten von Bohrkernen vor, die während der ODP Legs 141 (*Behrmann et al.*, 1992) und 202 (*Mix et al.*, 2003) gewonnen wurden. Die Lokationen der einzelnen ODP-Sites sind Abbildung 2.1 und Tabelle A.4 zu entnehmen. Die ODP–Daten (Abbildung B.9) zeigen in Übereinstimmung mit unseren in situ gemessenen Wärmeleitfähigkeiten (Tabelle A.2), dass die Wärmeleitfähigkeit der Sedimente vom Norden des Untersuchungsgebietes nach Süden hin abnimmt. Im Norden herrschen Werte um 0.8 W/(m K) vor, während im Bereich der CJT für Sedimente vergleichsweise hohe Wärmeleitfähigkeiten von über 1.2 W/(m K) oberflächennah gemessen wurden. Daher ziehen wir in unseren Modellen für den Seds-Bereich mögliche Wärmeleitfähigkeiten von 0.7 – 1.5 W/(m K) in Betracht.

Für den OcCr-Bereich liegen weltweit nur sehr wenige Daten vor, die gut mit den konduktiven Abkühlungsmodell von *Stein and Stein* (1992) übereinstimmen. Daraus ergibt sich für die ozeanische Kruste eine Wärmeleitfähigkeit k von 2.9 W/(m K) und eine Wärmekapazität ρC von 3.3 MJ/m^3.

Im Untersuchungsgebiet ist es schwierig, die Modellbereiche des kontinentalen Basements (CnBs) und der Sedimente (Seds) auf Grund von seismischen Daten eindeutig zu trennen. Zum einen treten schon unmittelbar landwärts der Deformationsfront sehr hohe seismische Geschwindigkeiten von ca 4 km/s in den akkretierten Sedimenten auf. Diese Geschwindigkeiten sind typisch für konsolidierte Silt- oder Sandsteine (*Schön*, 1996, pp. 173, 178). In unkonsolidieren Sedimenten würde man Geschwindikeiten von unter 2.5 km/s erwarten (*Schön*, 1996, pp. 193). Da der kontinentale Backstop im Untersuchungsgbiet aus metamorph überprägten Akkretionsstrukturen besteht (*Behrmann et al.*, 1994), nehmen wir an, dass die thermischen Eigenschaften im CnBs-Bereich und im Seds-Bereich fließend ineinander übergehen. Um dem Rechnung zu tragen haben wir die Wärmeleitfähigkeiten in diesen Modellbereichen in Abhängigkeit von der vorgefundenen seismischen Geschwindigkeit definiert (vgl. Abbildung 3.11). Dabei gehen wir davon aus, dass die Wärmeleitfähigkeiten im CnBs-Bereich zwischen 1.7 W/(m K) für semi-konsolidierte akkretierte Sedimente und maximal

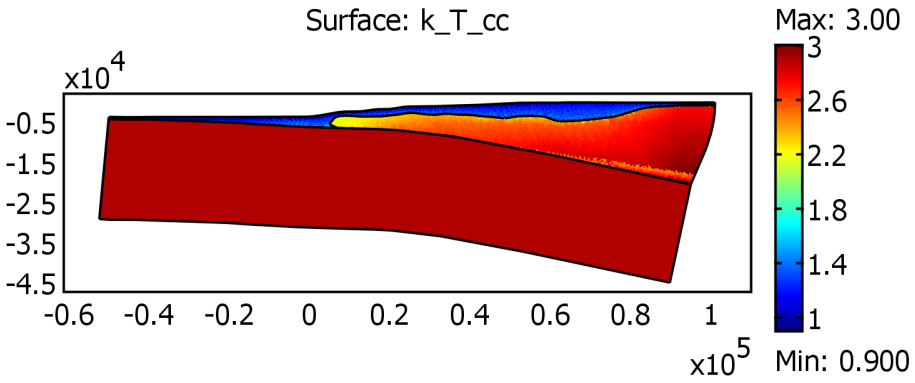

Abbildung 3.11: Beispiel der Wärmeleitfähigkeitsverteilung eines Modells für Korridor 2. Die farbcodierte Wärmeleitfähigkeit in den Seds- und CnBs-Bereichen hängt linear von den seismischen Geschwindigkeiten (siehe Abb. B.3) ab.

3.5 W/(m K) für das kontinentale Basement liegen. Dieser Wertebereich deckt sich mit Annahmen, die auch schon in früheren Studien (z.B. *Oleskevich et al.* (1999)) gemacht wurden.

3.3.5 Wärmeproduktion

Die Abschätzung der radiogenen Wärmeproduktion in den einzelnen Modellbereichen stützt sich auf Messungen der natürlichen Gammastahlung in den Bohrungen von ODP Leg 141 im südlichen Untersuchungsgebiet, da während ODP Leg 202 kein entsprechendes Logging-Programm durchgeführt wurde. *Grevemeyer et al.* (2003) berechneten aus den Leg 141–Daten eine radiogene Wärmeproduktionsrate von 0.5-1.2 μW/m^3 für die erbohrten Fore-arc Sedimente, wobei zu vermuten ist, dass weiter nördlich auch geringere Werte auftreten können. Dieser Wertebereich stimmt mit den Annahmen von *Oleskevich et al.* (1999) überein, die von einer Wärmeproduktion von 0.8 μW/m^3 ausgegangen sind. Auf Grund der Ähnlichkeit des Ausgangsmaterial, nehmen wir an, dass die radiogene Wärmeproduktion im kontinentalen Basement in der gleichen Größenordnung liegt, wie die der vorgelagerten Sedimente.

Die präsentierten Modelle beinhalten ausschließlich eine, für den jeweiligen Modellbereich, homogene Wärmeproduktion, die mit der oben genannten radiogenen Wärmeproduktion gleich zusetzten ist. Unser Modell bietet zwar ohne weiteres die Möglichkeit kompliziertere Verteilungen der Wärmeproduktion zu simulieren, wie z.B. eine an der Scherzone lokalisierte Wärmeproduktion, zur Simulierung von Reibungswärme. Jedoch haben wir davon Abstand genommen, diese Möglichkeiten zu nutzten, da uns keine unabhängigen Daten vorliegen, die quantitavite Aussagen über Menge und Verteilung der Reibungswärme erlauben. Außerdem hat sich im Laufe unserer Modellierungen gezeigt, dass die vorliegenden Daten auch ohne die Annahme von Reibungswärme mit unseren Modellen im Einklang stehen.

3.4 Modellierung

Da sowohl die Modellparameter, als auch die unabhängigen Randbedingungen, die durch die Wärmestromdichtebestimmungen landwärts der Deformationsfront geben sind, zum Teil einen erheblichen Spielraum zulassen, gibt es nicht nur ein richtiges Modell, sondern ein ganzes Spektrum von mehr oder weniger wahrscheinlichen Kandidaten. Um das gesamte Spektrum von wahrscheinlichen Parameterkombinationen und ihre Auswirkungen auf die resultierende Temperaturverteilung entlang der Bruchzone zu untersuchen, haben wir uns eines genetischen Algorithmus bedient, der in der kürzlich eingereichten Publikation im Anhang C.1 (ab Seite 55) beschrieben ist. Dieser Algorithmus lässt iterativ Modelle mit verschiedenen Parameterkombinationen berechnen. Anschließend werden diese Modelle in Hinblick auf ihre Plausibilität bewertet. In diese Bewertung geht zum einen der Vergleich zwischen gemessenen und berechneten Wärmestromdichtewerten am Kontinentalhang ein. Zum anderen wird bewertet, in wieweit alle Modellparameter in dem für sie als wahrscheinlich angesehenen Intervall liegen. Aufgrund dieser Bewertungen, zielt der genetische Algorithmus darauf ab, weitere plausible Parameterkombinationen zu finden.

Abbildung 3.12 zeigt ein Beispiel für ein plausibles Modell in Korridor 2, bei dem alle Parameter in den im vorherigen Abschnitt definierten Grenzen liegen und die Wärmestrommessungen hinreichend gut reproduziert werden. Diese Modell ist eines von über 10,000, das von dem genetischen Algorithmus erzeugt wurde. In Abbildung 3.13 sind die verschiedenen Untersuchten Parameterkombinationen und die daraus resultierenden Temperaturen an der Bruchzone als Histogramme dargestellt. Aus diesen Histogrammen lässt sich abschätzten, mit welcher Genauigkeit sich die Temperaturen modellieren lassen. Dabei sollte man immer beachten, dass der Modellierungsansatz viele Vereinfachungen, z.B. die Vernachlässigung von allen transienten Phänomenen, im Vergleich zur Realität beinhaltet. Mit der Ausnahmen von Korridor 4, wo die gemessenen Wärmestromdichtewerte deutlich von den modellierten Werten abweichen, lassen sich jedoch alle Beobachtungen widerspruchsfrei in unser Modell integrieren.

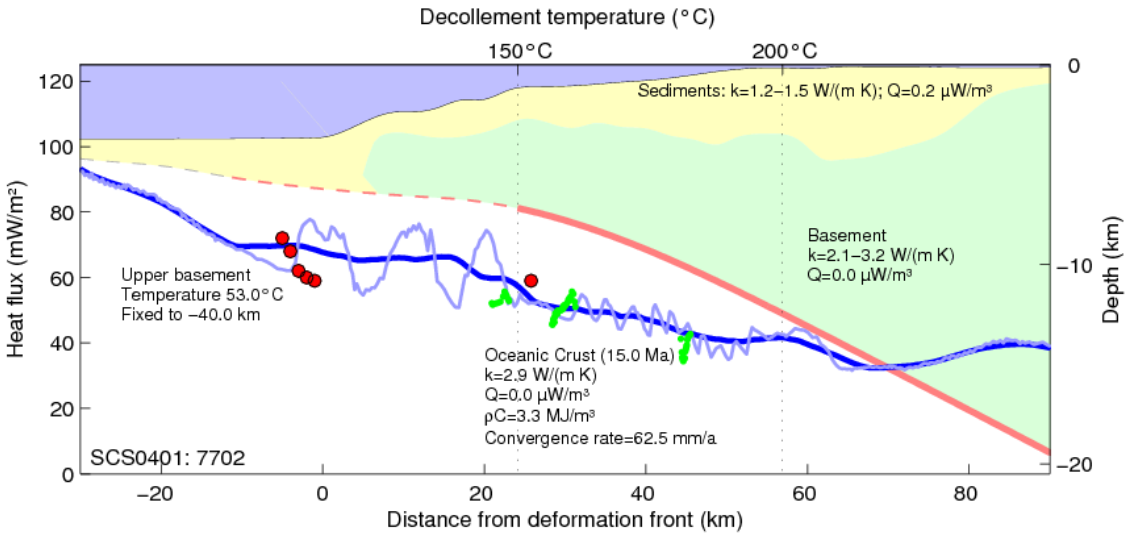

Abbildung 3.12: Detailierte Ergebisse eines FE-Modells auf Korridor 2. Die ober Grenze des OcCr-Bereichs ist unter dem Seds- und CnBs-Bereich (gelb und grün) als gestrichelte Linie dargestellt, die ab einer Bruchzonentemperatur von 150°C (obere Achse) rot und durchgezogen ist. Die blauen Linien geben die berechneten Wärmestromdichtewerte (dunkelblau geglättet) wieder. Rote Kreise zeigen Wärmestromdichtemessungen und Abschätzungen aus BSRs sind als grüne Punkte gekennzeichnet.

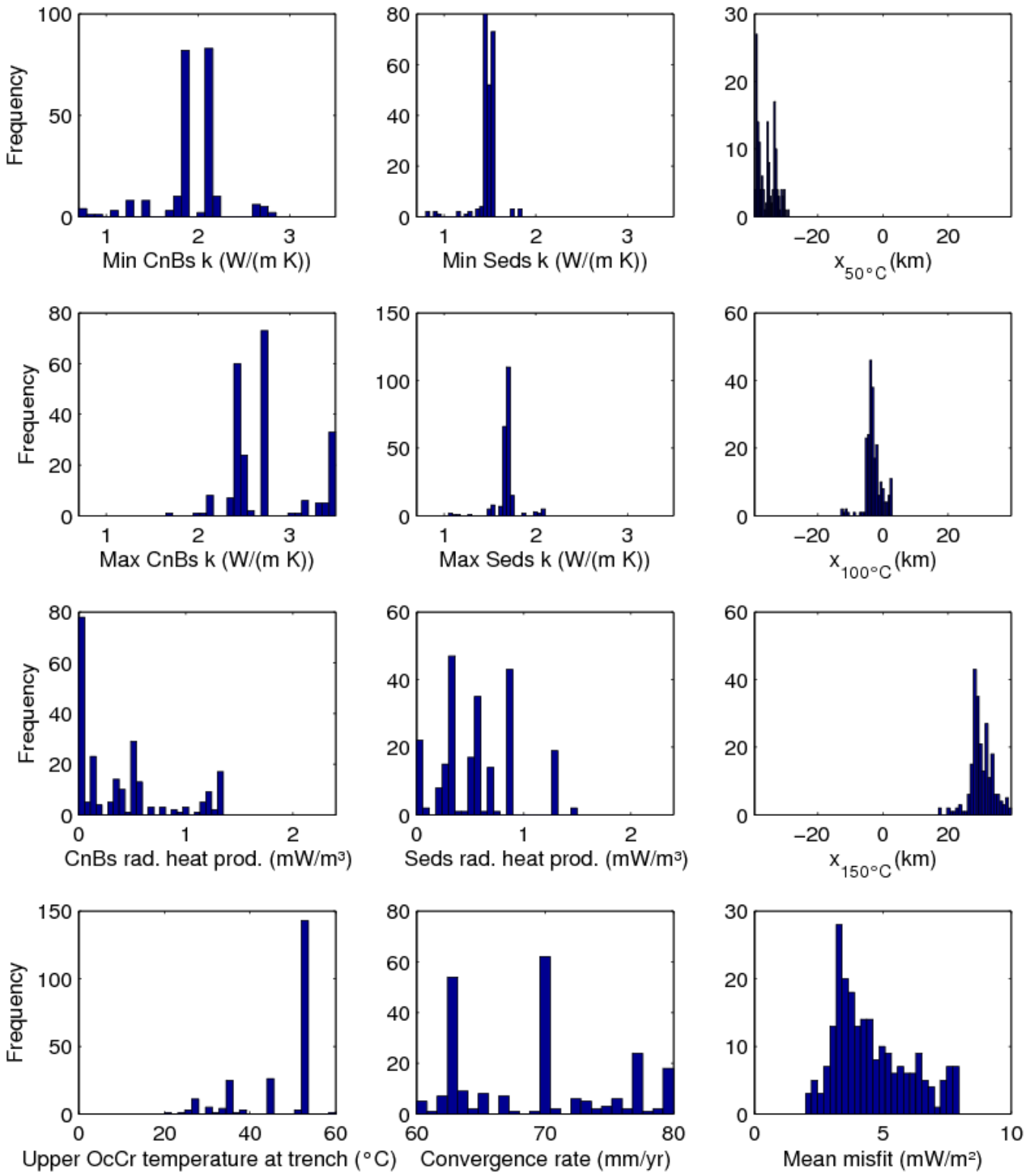

Abbildung 3.13: Parameter (linke und mittle Spalten) und Ergebnisse (rechte Spalte) verschiedener FE-Modelle auf Korridor 2. Alle Modelle basieren auf plausiblen Parameterkombinationen und stehen in Übereinstimmung mit den gemessenen Wärmestromdichtedaten.

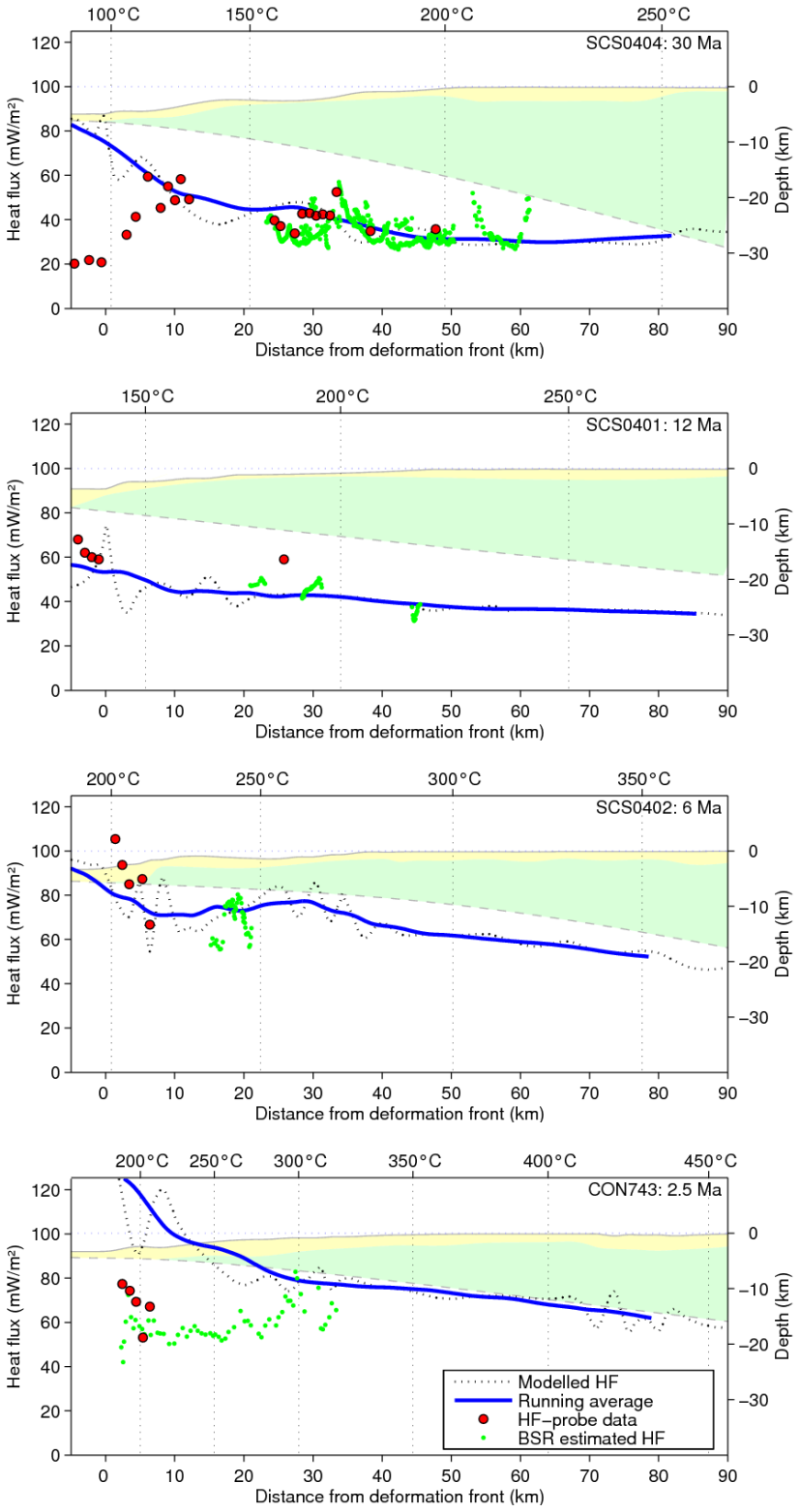

Abbildung 3.14: Modellbeispiele von Korridor 1–4 (von oben nach unten). Zur besseren Vergleichbarkeit wurden für alle Modelle die Parameter in Tabelle 3.1 verwendet.

Tabelle 3.1: Vereinheitlichte Modellparameter für die Modelle in Abbildung 3.14.

	OcCr	CnBs	Seds
k (W/m K)	2.9	2.15	1.1
Q (μW/m^2)	-	1.1	-
ρC (MJ/(K m^3))	3.3	-	-
v (mm/a)	75-79	-	-
Age (Ma)	2-30	-	-

Die Modellergebnisse auf den Korridoren 1–4 sind in Abbildung 3.15 zusammengefasst. Der Beginn der seismogenen Zone fällt in Korridor 3 und 4 im wesentlichen mit der Deformationsfront zusammen, verschiebt sich dann in Richtung Norden immer weiter landwärts der Deformationszone. Wie zu erwarten nimmt die Breite der seismogenen Zone von Korridor 4 bis 2 mit zunehmendem Krustenalter zu. Die seismogene Zone in Korridor 1, wo etwa doppelt so alte Kruste wie in Korridor 2 subduziert wird, unterscheidet sich allerdings nicht wesentlich von der in Korridor 2. Die Lage der seismogenen Zone, abgeleitet aus den Modellierungen, ist in guter Übereinstimmung mit der genauen Lokalisierung von lokalen Erdbeben (vgl. Abbildung 3.16 aus *Lange et al.* (2007)) und den Daten des globalen Kataloges (ANSS) für Beben mit einer Magnitude > 5: die Bebentätigkeit beginnt in etwa an der Deformationsfront (der 150°C-Grenze) und erstreckt sich dann von dort aus landwärts. Es ist auffällig, dass von *Lange et al.* (2007) kaum Seismizität im Bereich zwischen 0–70 km landwärts der Deformationsfront lokalisiert wurde (siehe (2) in Abb. 3.16 unten). Dieses aseismische Verhalten im oberen Bereich der seimogenen Zonen, die nach unseren Modellierungen schon ca. 20 km landwärts der Deformationsfront beginnen sollte, wird mit dem großen Versatz (ca. 17 m) der durch das große Chile Erdbeben von 1960 verursacht wurde und zu einem Spannungsabbau führte, erklärt (*Lange et al.*, 2007; *Barrientos and Ward*, 1990).

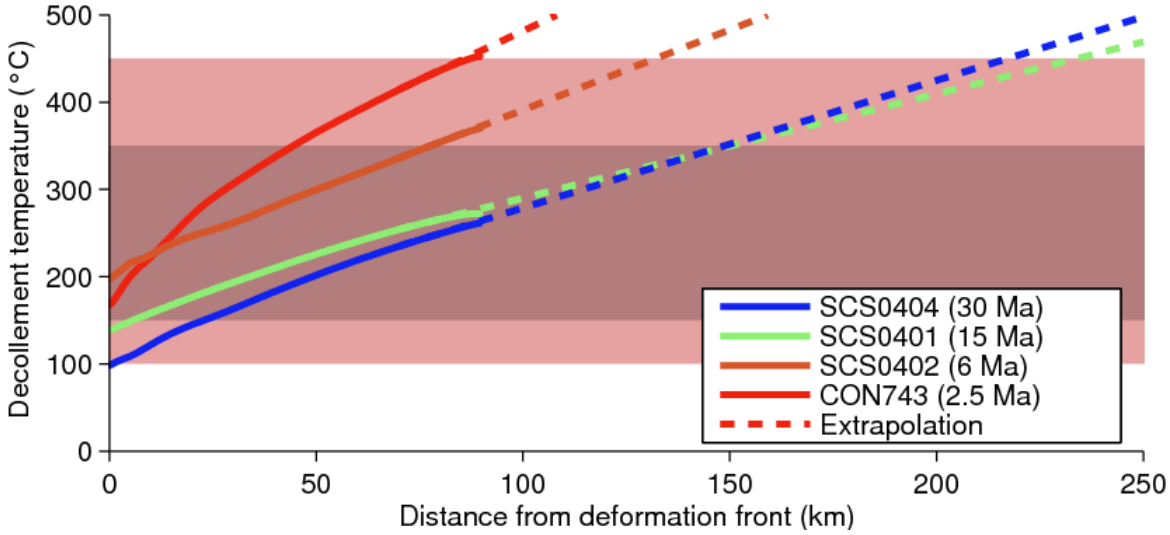

Abbildung 3.15: Temperaturen in Korridor 1–4 entlang der Bruchzone des 1960 Erdbebens in Abhängigkeit von der Entfernung zur Deformationsfront. Die Temperaturen sind linear zu größeren Entfernungen extrapoliert (gestrichelt). Der thermisch definierte Bereich der seismogenen Zone (100 bis 350° C; e.g. *Hyndman and Wang* (1993)) ist dunkelrot hinterlegt und der Temperaturbereich (100 bis 450°C), an dem es unter bestimmten Voraussetzungen zu bruchhaften Verhalten kommen kann ist hellrot gekennzeichnet.

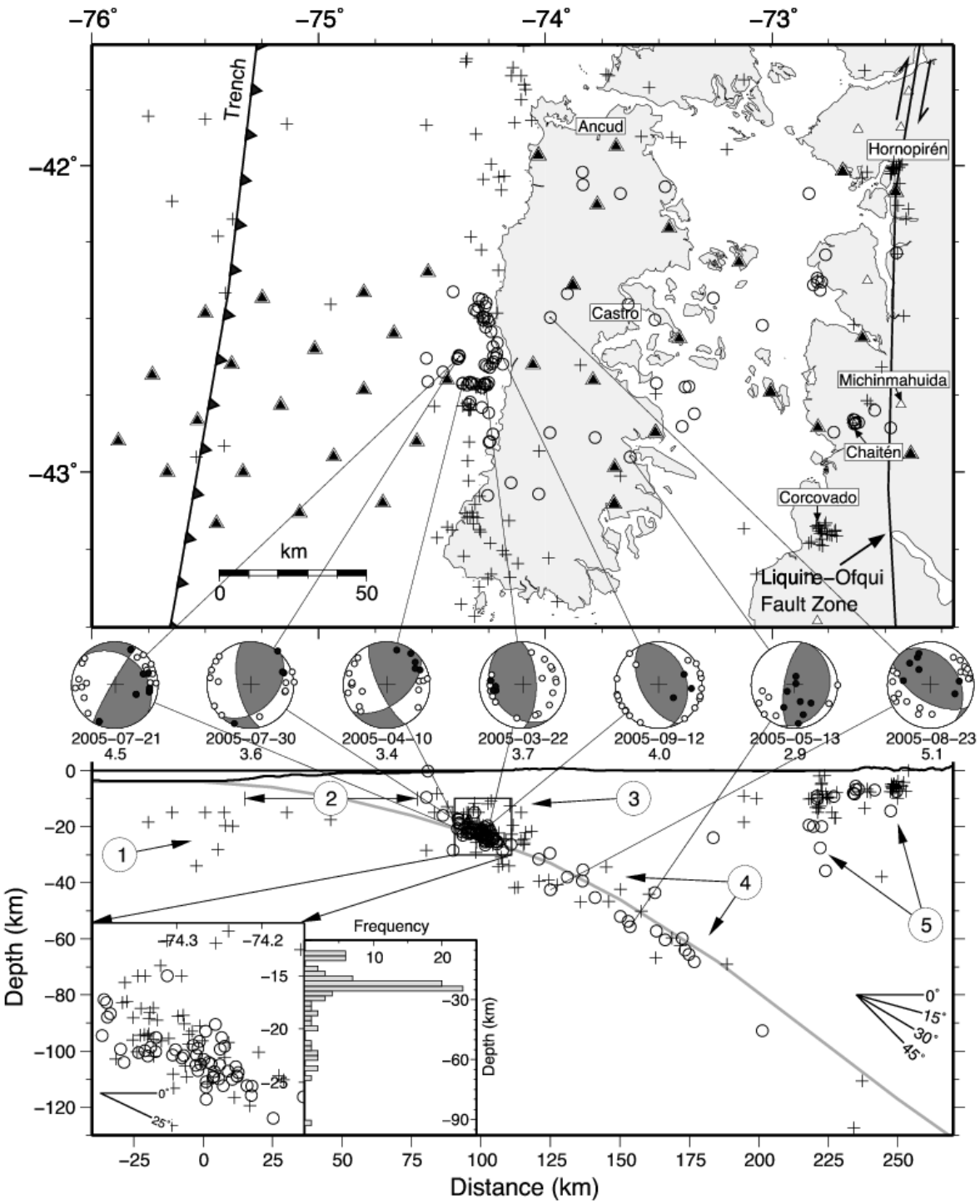

Abbildung 3.16: Lokationen von 245 von *Lange et al.* (2007) lokalisierten Erdbeben (Kreise und Kreuze) auf Korridor 2. Die Positionen von Seismometerstationen sind durch schwarze Dreiecke (oben) gekennzeichnet. Die auf den Tiefenschnitt (unten) projezierten Hypozentren zeigen klar den Verlauf der Wadati-Benioff Zone (*Lange et al.*, 2007).

4 Erfolgskontrollbericht

4.1 Beitrag zu den förderpolitischen Zielen

Die Ergebnisse der Forschungsreise sind ein wichtiger und international anerkannter Beitrag zur Erforschung von Subduktionszonen.

4.2 Wissenschaftliche Erfolge

Die wissenschaftlichen erfolge des Teilprojekts 7 – Geothermie – können wie folgt zusammen gefasst werden:

- Auf vier Profilen nördlich der Chile-Triple Junction wurden reflexionsseismische Messungen durchgeführt, um zum einen die Sediment-Basement-Grenze seewärts der Deformationsfront zu kartieren und um zum anderen die Geometrie der Sedimentfüllung des Grabens zu erfassen, die für die Interpretation der refraktionsseismischen Messungen als Zusatzinformation wichtig ist. Zusätzlich wurde der BSR auf dem Kontinentalhang kartiert.

- Auf insgesamt fünf Profilen nördlich der Chile-Triple Junction wurden Wärmstromdichtemessungen von der Nazca-Platte über Tiefseegraben hinweg hinauf auf den Kontinent durchgeführt. Advektive Effekte auf der einfahrenden Platte führen zu einer Erniedrigung des Wärmestromes, relativ zu einem konduktiven Abkühlungsmodell. Die Messungen werden ergänzt durch Abschätzungen des Wärmestromes aus BSR-Tiefen auf dem Kontinentalhang.

- Das Temperaturfeld im oberen Bereich der seismogenen Zone wurde mit einem stationären Finite Elemente (FE) Modell berechnet, das auf dem FE Softwarepaket Comsol Multiphysics® Toolbox und Matlab® aufbaut. Das Modell berücksichtigt, abgesehen von dem mit der Konvergenz der abtauchenden Platte zusammen hängenden advektiven Wärmetransport, ausschließlich konduktive Wärmetransport. Die Vorgabe der Modell-Geometrie basierte zum überwiegenden Teil auf den Ergebnissen der Refraktionsseismik, die im Projekt TIPTEQ durchgeführt wurde. Die Randbedingungen für die Modellierungen stützen sich ganz entscheidend auf die Wärmestromdichtemessungen, die während der Expedition SO181-1b durchgeführt wurden.

- Um den Einfluss der Wahl der Parameter und ihrer Kombination auf das modellierte Temperaturfeld erfassen zu können, wurden mittels eine genetischen Algorithmus für jeden Korridor ca. 10,000 Modelle berechnet. Als richtigeModelle wurden diejenigen ausgewählt, die zum einen in Übereinstimmung mit den gemessenen Wärmeströmen

sind, zum anderen deren Parameter in geologisch/geophysikalisch sinnvollen Grenzen sind.

- Der Beginn der seismogenen Zone fällt in Korridor 3 und 4 im Wesentlichen mit der Deformationsfront zusammen, verschiebt sich dann in Richtung Norden immer weiter landwärts der Deformationszone. Wie zu erwarten nimmt die Breite der seismogenen Zone von Korridor 4 bis 2 mit zunehmendem Krustenalter zu. Die Lage der seismogenen Zone, abgeleitet aus den Modellierungen, ist in guter Übereinstimmung mit der genauen Lokalisierung von lokalen Erdbeben *Lange et al.* (2007) und den Daten des globalen Kataloges (ANSS) für Beben mit einer Magnitude > 5: die Bebentätigkeit beginnt in etwa an der Deformationsfront (der 150°C-Grenze) und erstreckt sich dann von dort aus landwärts.

4.3 Zeit- und Finanzierungsplan

Der durch die Bewilligung vorgegebene Zeit- und Finanzierungsplan wurde eingehalten.

Literaturverzeichnis

Bangs, N. L., and S. C. Cande, Episodic development of a convergent margin inferred from structures and processes along the southern chile margin, *Tectonics*, *16*, 489–503, 1997.

Barrientos, S. E., and S. N. Ward, The 1960 chile earthquake - inversion for slip distribution from surface deformation, *Geophysical Journal International*, *103*, 589–598, 1990.

Behrmann, J., Lewis, S.D., and R. Musgrave (Eds.), *Proc. ODP, Init. Repts*, vol. 141, College Station, TX (Ocean Drilling Program), 1992.

Behrmann, J. H., S. D. Lewis, and S. C. Cande, Tectonics and geology of spreading ridge subduction at the chile triple junction: a synthesis of results from leg 141 of the ocean drilling program, *International Journal of Earth Sciences*, *V83*, 832–852, 1994.

Brown, K. M., N. L. Bangs, P. N. Froelich, and K. A. Kvenvolden, The nature, distribution, and origin of gas hydrate in the chile triple junction region, *Earth and Planetary Science Letters*, *139*, 471–483, 1996.

Cande, S. C., R. B. Leslie, J. C. Parra, and M. Hobart, Interaction between the Chile Ridge and Chile Trench: Geophysical and geothermal evidence, *J. Geophys. Res.*, *92*, 495–520, 1987, artikel in Bib bestellt.

Cohen, J., and J. Stockwell Jr., *Seismic Unix Release 40, a free package for research and processing*, Center for Wave Phenomena, Colorado School of Mines, 2007.

Contreras-Reyes, E., I. Grevemeyer, E. R. Flueh, M. Scherwath, and M. Heesemann, Alteration of the subducting oceanic lithosphere at the southern central chile trench-outer rise, *Geochem. Geophys. Geosyst.*, *8*, Q07,003, 2007.

Flueh, E. R., and I. Grevemeyer (Eds.), *RV Sonne Fahrtbericht / Cruise Report SO 181 TIPTEQ (from The Incoming Plate to mega Thrust EarthQuakes) 06.12.2004.-26.02.2005*, 2, 2005, 533 pp.

Grevemeyer, I., and H. Villinger, Gas hydrate stability and the assessment of heat flow through continental margins, *Geophysical Journal International*, *145*, 647–660, 2001.

Grevemeyer, I., J. L. Diaz-Naveas, C. R. Ranero, and H. W. Villinger, Heat flow over the descending nazca plate in central chile, 32[deg]s to 41[deg]s: observations from odp leg 202 and the occurrence of natural gas hydrates, *Earth and Planetary Science Letters*, *213*, 285–298, 2003.

Grevemeyer, I., N. Kaul, J. L. Diaz-Naveas, H. W. Villinger, C. R. Ranero, and C. Reichert, Heat flow and bending-related faulting at subduction trenches: Case studies offshore of nicaragua and central chile, *Earth and Planetary Science Letters*, *236*, 238–248, 2005.

Harris, R. N., and K. Wang, Thermal models of the Middle America Trench at the Nicoya Peninsula, Costa Rica, *Geophys. Res. Lett.*, *29*, 6–1, 2002.

Hartmann, A., and H. Villinger, Inversion of marine heat flow measurements by expansion of the temperature decay function, *Geophysical Journal International*, *148*, 628–636, 2002.

Hyndman, R. D., and K. Wang, Thermal constraints on the zone of major thrust earthquake failure - the cascadia subduction zone, *J. Geopyhs. Res.*, *98*, 2039–2060, 1993.

Hyndman, R. D., E. E. Davis, and J. A. Wright, The measurement of marine geothermal heat flow by a multipenetration probe with digital acoustic telemetry and insitu thermal conductivity, *Marine Geophysical Researches*, *V4*, 181–205, 1979.

Hyndman, R. D., K. Wang, and M. Yamano, Thermal constraints on the seismogenic portion of the southwestern Japan subduction thrust, *J. Geophys. Res.*, *100*, 15,373–15,392, 1995.

Kaul, N., A. Rosenberger, and H. Villinger, Comparison of measured and bsr-derived heat flow values, makran accretionary prism, pakistan, *Marine Geology*, *164*, 37–51, 2000.

Kendrick, E., M. Bevis, R. Smalley, B. Brooks, R. B. Vargas, E. Lauria, and L. P. S. Fortes, The nazca-south america euler vector and its rate of change, *Journal of South American Earth Sciences*, *16*, 125–131, 2003.

Lange, D., A. Rietbrock, C. Haberland, K. Bataille, T. Dahm, F. Tilmann, and E. R. Flüh, Seismicity and geometry of the south chilean subduction zone (41.5° s – 43.5° s): Implications for controlling parameters, *Geophys. Res. Lett.*, *34*, L06,311, 2007.

Mix, A., R. Tiedemann, and P. Blum (Eds.), *Proc. ODP, Init. Repts*, vol. 202, College Station, TX (Ocean Drilling Program), 2003.

Oleskevich, D. A., R. D. Hyndman, and K. Wang, The updip and downdip limits to great subduction earthquakes: Thermal and structural models of cascadia, south alaska, sw japan, and chile, *J. Geophys. Res.*, *104*, 14,965–14,992, 1999.

Plafker, G., and J. C. Savage, Mechanism of the chilean earthquakes of may 21 and 22, 1960, *Geol Soc Am Bull*, *81*, 1001–1030, 1970.

Pribnow, D., M. Kinoshita, and C. Stein, Thermal data collection and heat flow recalculations for ODP Legs 101-180, *Tech. rep.*, Institute for Joint Geoscientific Research, Institute for Joint Geoscientific Research, GGA, Hannover, Germany, 0120432., 2000.

Schön, J. H., *Physical properties of rocks: fundamentals and principles of petrophysics*, vol. 18 of *Handbook of geophysical exploration: seismic exploration*, Elsevier Science, 1996.

Smith, W. H., and D. T. Sandwell, Global sea floor topography from satellite altimetry and ship depth soundings, *Science*, *277*, 1956–1962, 1997.

Stein, C. A., and S. Stein, A model for the global variation in oceanic depth and heat flow with lithospheric age, *Nature*, *359*, 123–129, 1992.

Tassara, A., Structure of the andean continental margin and causes of its segmentation, Ph.D. thesis, Freie Universität Berlin, 2005.

Tebbens, S. F., and S. C. Cande, Southeast Pacific tectonic evolution from early Oligocene to Present, *J. Geophys. Res.*, *102*, 12,061–12,084, 1997.

The SPOC Team, and C. Krawcyzk, Amphibious Seismic Survey Images Plate Interface at 1960 Chile Earthquake, *EOS Transactions*, *84*, 301–304, 2003.

A Tabellen

Tabelle A.1: Reflektionsseismische Linien auf denen von uns Wärmestromdichtemessungen durchgeführt wurden

Line	Corridor	Deformation Front		Pole (great circle)		Azimuth	Age
		Lon	Lat	Lon	Lat		Oc. crust
	#	°	°	°	°	°	Ma
SCS0404	1	-74.1103	-36.1552	-58.8687	52.8623	100.1	32
SCS0403	1	-75.1537	-40.6887	-86.7094	48.7306	82.6	19
SCS0401	2	-75.5016	-42.8424	-90.0058	46.2396	81.7	15
SCS0402	3	-75.8107	-44.5164	-98.1232	43.2549	74.9	6
CON743	4	-75.9461	-45.5851	-106.5110	40.1517	73.0	2.5

Tabelle A.2: SO-181-1b Wärmestromdichtemessungen

Station	Pen	Lon		Lat		Depth	N_{Sens}	Tilt	Grad	k	q	Dist	Shot	Line
	#	°	'	°	'	m	#	°	mK/m	W/(m K)	mW/m^2	km	#	
H0401	1	-78	21.952	-43	10.451	-3544	10	0.7	136.2	0.87	119.9	234.7	10974	SCS01
H0401	2	-78	22.693	-43	10.523	-3672	11	1.6	108.6	0.86	93.4	235.7	10994	SCS01
H0401	3	-78	23.400	-43	10.620	-3595	11	3.7	229.8	0.86	200.6	236.6	11012	SCS01
H0401	4	-78	24.142	-43	10.685	-3612	11	1.6	98.1	0.86	84.4	237.7	11031	SCS01
H0401	5	-78	24.881	-43	10.760	-3573	10	6.3	146.6	0.86	127.5	238.7	11050	SCS01
H0401	6	-78	25.581	-43	10.865	-3534	11	2.2	182.5	0.87	160.9	239.6	11067	SCS01
H0401	7	-78	26.347	-43	10.964	-3567	11	1.9	146.5	0.86	126	240.7	11086	SCS01
H0401	8	-78	27.082	-43	11.047	-3595	9	7.2	79.1	0.83	64.4	241.7	11105	SCS01
H0401	9	-78	27.806	-43	11.149	-3574	10	9.1	147.7	0.86	126.9	242.7	11124	SCS01
H0401	10	-78	28.518	-43	11.235	-3585	11	4.9	90.5	0.86	78.6	243.6	11142	SCS01
H0402	1	-76	41.731	-42	58.538	-3533	11	0.7	7	0.86	7	97.2	5623	SCS01
H0402	2	-76	42.422	-42	58.561	-3530	11	5.5	9	0.87	9	98.1	5654	SCS01
H0402	3	-76	43.192	-42	58.657	-3530	11	12.3	13	0.89	13	99.2	5689	SCS01
H0402	4	-76	43.913	-42	58.720	-3528	11	5.0	19	0.93	19	100.2	5721	SCS01
H0402	5	-76	44.630	-42	58.784	-3528	11	13.0	23	0.95	22	101.2	5755	SCS01
H0402	6	-76	45.342	-42	58.909	-3530	11	6.6	50	0.94	45	102.2	5789	SCS01
H0402	7	-76	46.087	-42	58.984	-3525	11	7.6	115	0.94	109	103.2	5822	SCS01
H0402	8	-76	46.844	-42	59.088	-3526	11	6.7	166	0.94	156	104.2	5858	SCS01
H0402	9	-76	47.552	-42	59.167	-3527	11	15.8	169	0.94	160	105.2	5891	SCS01
H0402	10	-76	48.278	-42	59.256	-3522	11	8.3	118	0.89	99	106.2	5925	SCS01
H0403	1	-75	11.660	-42	47.710	-1583	NaN	NaN	NaN	NaN	NaN	NaN	1358	SCS01
H0403	2	-75	10.930	-42	47.610	-1423	NaN	NaN	NaN	NaN	NaN	NaN	1339	SCS01
H0403	3	-75	10.200	-42	47.500	-1236	NaN	NaN	NaN	NaN	NaN	NaN	1320	SCS01
H0403	4	-75	9.480	-42	47.430	-1146	7	4.5	NaN	NaN	NaN	NaN	1301	SCS01
H0403	5	-75	8.770	-42	47.350	-1121	3	4.7	NaN	NaN	NaN	NaN	1282	SCS01
H0403	6	-75	8.030	-42	47.300	-1123	3	5.5	NaN	NaN	NaN	NaN	1262	SCS01
H0403	7	-75	7.290	-42	47.210	-1121	NaN	NaN	NaN	NaN	NaN	NaN	1242	SCS01
H0403	8	-75	6.530	-42	47.110	-1071	NaN	NaN	NaN	NaN	NaN	NaN	1223	SCS01

Fortsetzung Tabelle A.2

H0403	9	-75	5.790	-42	47.000	-1076	NaN	NaN	NaN	NaN	NaN	NaN	1204	SCS01
H0403	10	-75	5.060	-42	46.910	-1106	NaN	NaN	NaN	NaN	NaN	NaN	1185	SCS01
H0403	11	-75	4.400	-42	46.820	-1092	NaN	NaN	NaN	NaN	NaN	NaN	1168	SCS01
H0403	12	-75	3.670	-42	46.740	-1062	5	0.7	NaN	NaN	NaN	NaN	1149	SCS01
H0403	13	-75	2.960	-42	46.640	-999	NaN	NaN	NaN	NaN	NaN	NaN	1129	SCS01
H0403	14	-75	2.240	-42	46.570	-900	NaN	NaN	NaN	NaN	NaN	NaN	1108	SCS01
H0404	1	-75	34.670	-42	50.449	-3743	17	0.7	84	0.86	72	5.00	2252	SCS01
H0404	2	-75	33.954	-42	50.369	-3742	17	2.2	80	0.84	68	4.00	2214	SCS01
H0404	3	-75	33.241	-42	50.280	-3744	17	3.6	75	0.81	62	3.00	2175	SCS01
H0404	4	-75	32.498	-42	50.191	-3736	17	1.9	71	0.84	60	2.00	2135	SCS01
H0404	5	-75	31.786	-42	50.118	-3736	17	1.1	68	0.87	59	1.00	2103	SCS01
H0404	6	-75	31.773	-42	50.108	-3736	17	1.0	66	0.88	59	1.00	2103	SCS01
H0405	1	-75	52.343	-45	33.854	-2524	9	0.9	72.9	0.92	67.1	-6.4	NaN	CON743
H0405	2	-75	53.044	-45	34.059	-2436	13	2.9	50.4	1.04	53.1	-5.4	NaN	CON743
H0405	3	-75	53.757	-45	34.256	-2558	3	3.5	60.2	1.16	69.3	-4.4	NaN	CON743
H0405	4	-75	54.434	-45	34.419	-2707	10	2	59.6	1.25	74.3	-3.5	NaN	CON743
H0405	5	-75	55.192	-45	34.685	-3058	10	8.4	60.1	1.33	77.4	-2.4	NaN	CON743
H0405	6	-75	55.781	-45	34.856	-3191	8	3.6	101.4	1.28	129.8	-1.6	NaN	CON743
H0405	7	-75	56.527	-45	35.083	-3262	9	4.6	148.2	1.24	184.6	-0.5	NaN	CON743
H0405	8	-75	57.365	-45	35.299	-3333	9	5.2	188.5	1.18	222.4	0.6	NaN	CON743
H0405	9	-75	58.060	-45	35.527	-3317	8	4.2	196.2	1.13	218.6	1.6	NaN	CON743
H0406	1	-76	15.180	-44	36.370	-3275	9	1	223.1	1.06	234.3	36.4	3613	SCS02
H0406	2	-76	15.880	-44	36.510	-3281	9	3.8	342.6	1.04	356.3	37.3	3652	SCS02
H0406	3	-76	16.610	-44	36.680	-3281	8	15.7	395.7	0.98	387.4	38.3	3694	SCS02
H0406	4	-76	17.355	-44	36.830	-3332	9	6.5	385.6	0.97	374.0	39.3	3735	SCS02
H0406	5	-76	18.076	-44	36.968	-3333	8	14.4	434.5	0.96	420.6	40.3	3775	SCS02
H0406	6	-76	18.744	-44	37.074	-3321	8	6	457.1	0.96	438.8	41.2	3812	SCS02
H0406	7	-76	19.533	-44	37.281	3259	NaN	NaN	NaN	NaN	NaN	NaN	3856	SCS02
H0406	8	-76	20.255	-44	37.423	-3247	NaN	NaN	NaN	NaN	NaN	NaN	3898	SCS02
H0406	9	-76	20.985	-44	37.567	-3238	NaN	NaN	NaN	NaN	NaN	NaN	3941	SCS02
H0406	10	-76	21.658	-44	37.636	-3231	NaN	NaN	NaN	NaN	NaN	NaN	3980	SCS02
H0406	11	-76	22.432	-44	37.872	-3235	NaN	NaN	NaN	NaN	NaN	NaN	4026	SCS02
H0407	1	-75	42.605	-44	29.779	-2355	NaN	NaN	NaN	NaN	NaN	NaN	1953	SCS02
H0407	2	-75	43.300	-44	29.900	-2510	NaN	NaN	NaN	NaN	NaN	NaN	1987	SCS02
H0407	3	-75	44.082	-44	30.043	-2637	9	5.8	63.3	1.05	66.7	-6.4	2026	SCS02
H0407	4	-75	44.845	-44	30.265	-2957	4	2.3	83.1	1.05	87.3	-5.3	2064	SCS02
H0407	5	-75	45.489	-44	30.345	-3044	NaN	NaN	NaN	NaN	NaN	NaN	2096	SCS02
H0407	6	-75	46.270	-44	30.480	-3218	8	10.3	73.5	1.15	85.0	-3.4	2134	SCS02
H0407	7	-75	46.945	-44	30.665	-3242	12	2.6	78.1	1.2	93.7	-2.4	2168	SCS02
H0407	8	-75	47.665	-44	30.799	-3333	10	4.2	90.3	1.18	105.4	-1.4	2204	SCS02
H0407	9	-75	48.390	-44	30.953	-3317	NaN	NaN	NaN	NaN	NaN	NaN	2239	SCS02
H0407	10	-75	49.110	-44	31.092	-3319	NaN	NaN	NaN	NaN	NaN	NaN	2274	SCS02
H0408	1	-76	23.2	-42	56.29	3582	10	0.3	129.5	0.89	118	71.7	4799	SCS01
H0408	2	-76	22.47	-42	56.22	3588	10	3.7	126.2	1.05	133	70.7	4765	SCS01
H0408	3	-76	21.74	-42	56.11	3592	9	3.9	94.4	1.01	95	69.7	4730	SCS01
H0409	1	-75	11.643	-42	47.472	1558	NaN	NaN	NaN	NaN	NaN	NaN	1356	SCS01
H0409	2	-75	12.37	-42	47.56	1665	3	22.1	56.4	1.03	59	-25.8	1376	SCS01
H0409	3	-75	13.109	-42	47.656	1799	NaN	NaN	NaN	NaN	NaN	NaN	1396	SCS01
H0410	1	-75	4.44	-40	40.81	3470	9	1.7	34.6	0.9	31	-5.6	2246	SCS03
H0410	2	-75	3.74	-40	40.76	3342	9	4	36.7	0.91	33	-6.7	2209	SCS03
H0410	3	-75	3.03	-40	40.69	3238	8	4	42.6	0.92	39	-7.6	2172	SCS03
H0410	4	-75	2.3	-40	40.62	3206	11	4.8	37.5	0.91	27	-8.7	2132	SCS03
H0410	5	-75	1.58	-40	40.52	3159	9	5	45.4	0.9	40	-9.7	2093	SCS03
H0410	6	-75	0.9	-40	40.47	3076	6	4.5	51.3	0.91	47	-10.6	2056	SCS03

Fortsetzung Tabelle A.2

H0411	1	-75	6.7	-36	1.249	4342	7	1.4	9.6	0.82	8	NaN	5321	SCS04
H0411	2	-75	6.05	-36	1.340	4331	5	1.6	24.2	0.8	19	NaN	5281	SCS04
H0411	3	-75	5.36	-36	1.432	4297	5	3.9	73.7	0.83	61	NaN	5239	SCS04
H0411	4	-75	4.75	-36	1.524	4267	8	1.4	29.1	0.8	23	NaN	5201	SCS04
H0411	5	-75	4.08	-36	1.610	4231	7	5.6	32.2	0.83	27	NaN	5160	SCS04
H0411	6	-75	3.45	-36	1.706	4263	8	2.8	23.8	0.8	19	NaN	5123	SCS04
H0411	7	-75	2.77	-36	1.795	4273	7	1.2	25.4	0.81	21	NaN	5082	SCS04
H0411	8	-75	2.11	-36	1.879	4247	8	2.2	41.1	0.8	34	NaN	5041	SCS04

Tabelle A.3: Rezente und paläo Plattenkonvergenzraten im Untersuchungsgebiet. Berechnungen basieren auf Eulerpolen von *Kendrick et al.* (2003).

Line	Deformation front		Convergence		
	Lon	Lat	Recent	2 Ma B.C.	Azimuth
	°	°	mm/a	mm/a	°
SCS0404	-74.11	-36.16	62.6	73.6	80.2
SCS0403	-75.15	-40.69	61.7	72.5	80.6
SCS0401	-75.5	-42.84	61.1	71.9	80.7
SCS0402	-75.81	-44.52	60.6	71.3	80.7
CON743	-75.95	-45.59	60.3	70.9	80.7

Tabelle A.4: Übersicht über ODP-Sites, die Randbedingungen für die thermischen Modelle lieferten.

Leg	Site	Lon	Lat	Bathym.	# of measurements		Downhole logging	
		°	°	m	k	T	Gamma-ray	Density
141	859	-75.8542	-45.8955	2745	60	9	Yes	Yes
141	860	-75.7517	-45.8860	2146.9	54	3	Yes	No
141	861	-75.6921	-45.8500	1660.1	44	9	No	No
141	862	-75.8265	-46.5083	1257.4	12	0	No	No
141	863	-75.7729	-46.2370	2564.2	82	10	Yes	Yes
202	1232	-75.9013	-39.8909	4072.3	30	5	No	No
202	1233	-74.4499	-41.0001	838	23	7	No	No
202	1234	-73.6817	-36.2192	1014.7	21	4	No	No
202	1235	-73.5664	-36.1599	488.9	60	7	No	No

B Abbildungen

B.1 Reflexionsseismische Linien

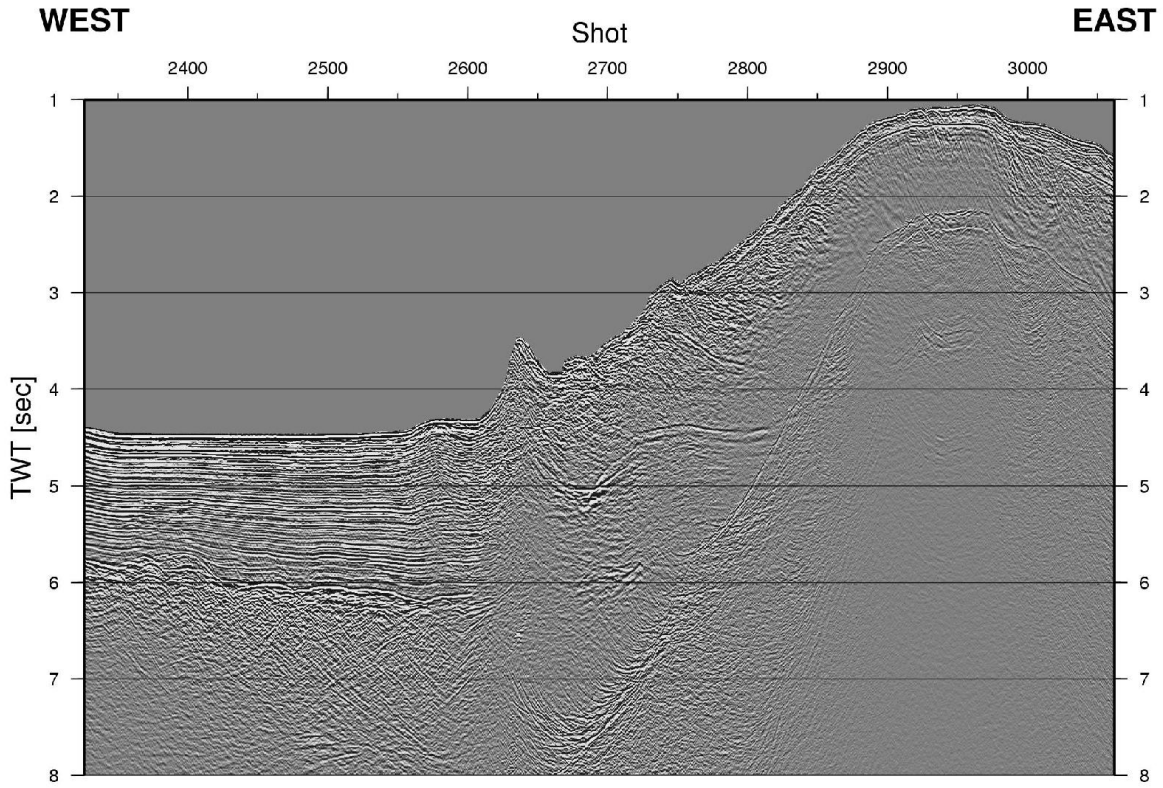

Abbildung B.1: Conrad 734 (Korridor 3)

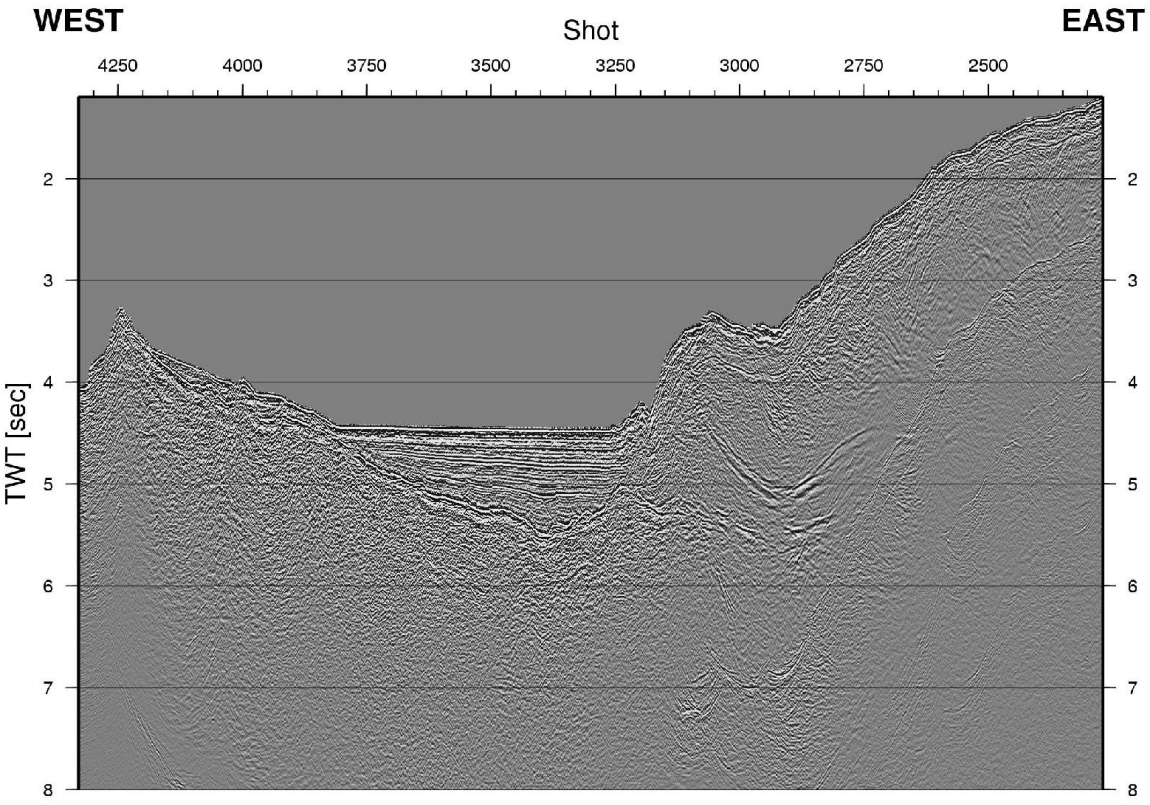

Abbildung B.2: Conrad 743 (Korridor 4)

B.2 Geschwindigkeitsmodelle

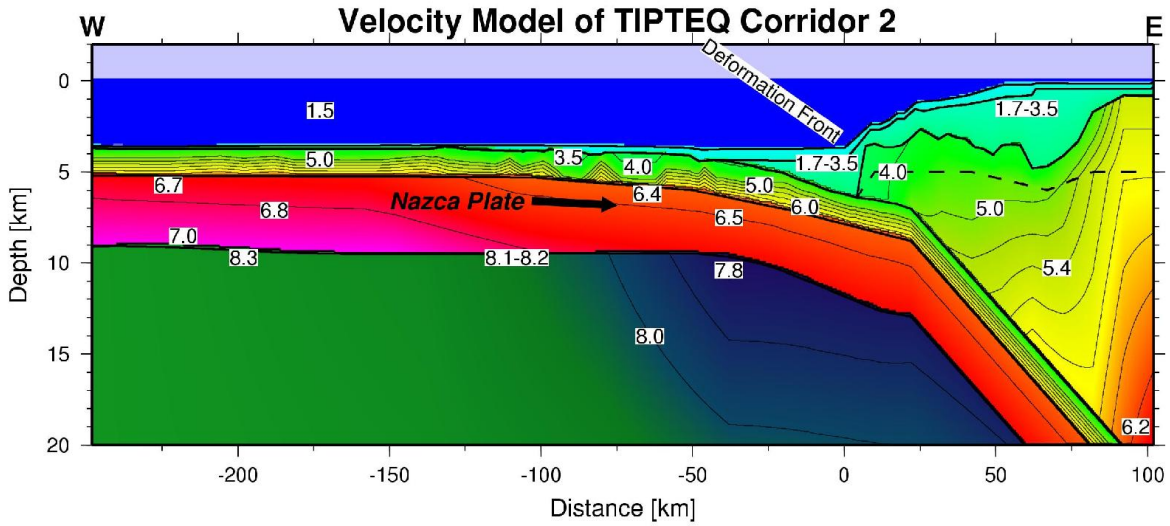

Abbildung B.3: Corridor 2 Geschwindingkeitsmodell (Martin Scherwarth pers. comm.)

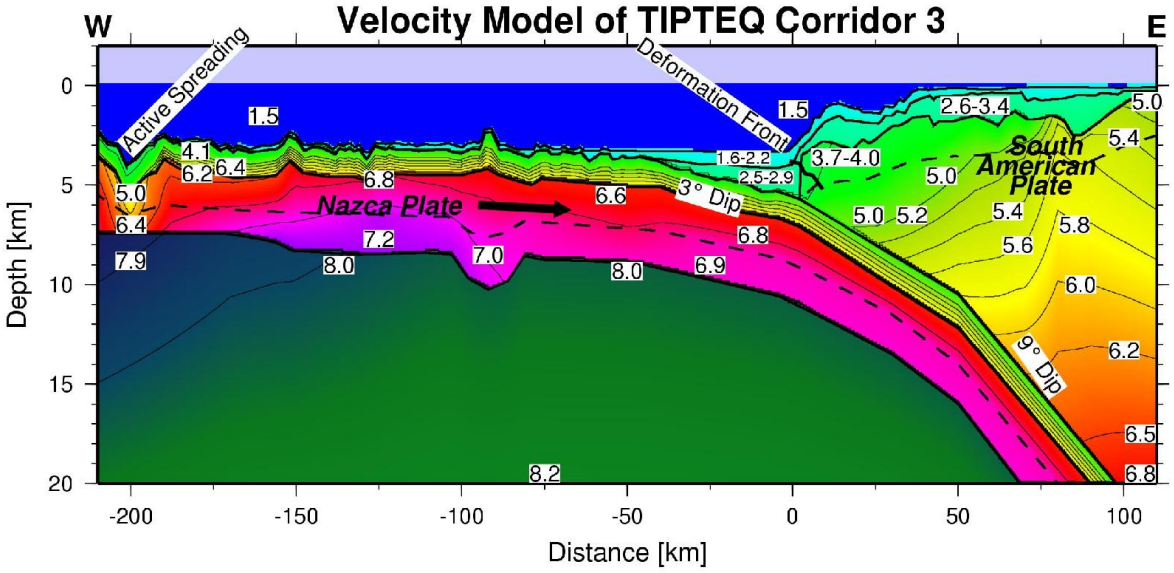

Abbildung B.4: Corridor 3 Geschwindingkeitsmodell (Martin Scherwarth pers. comm.)

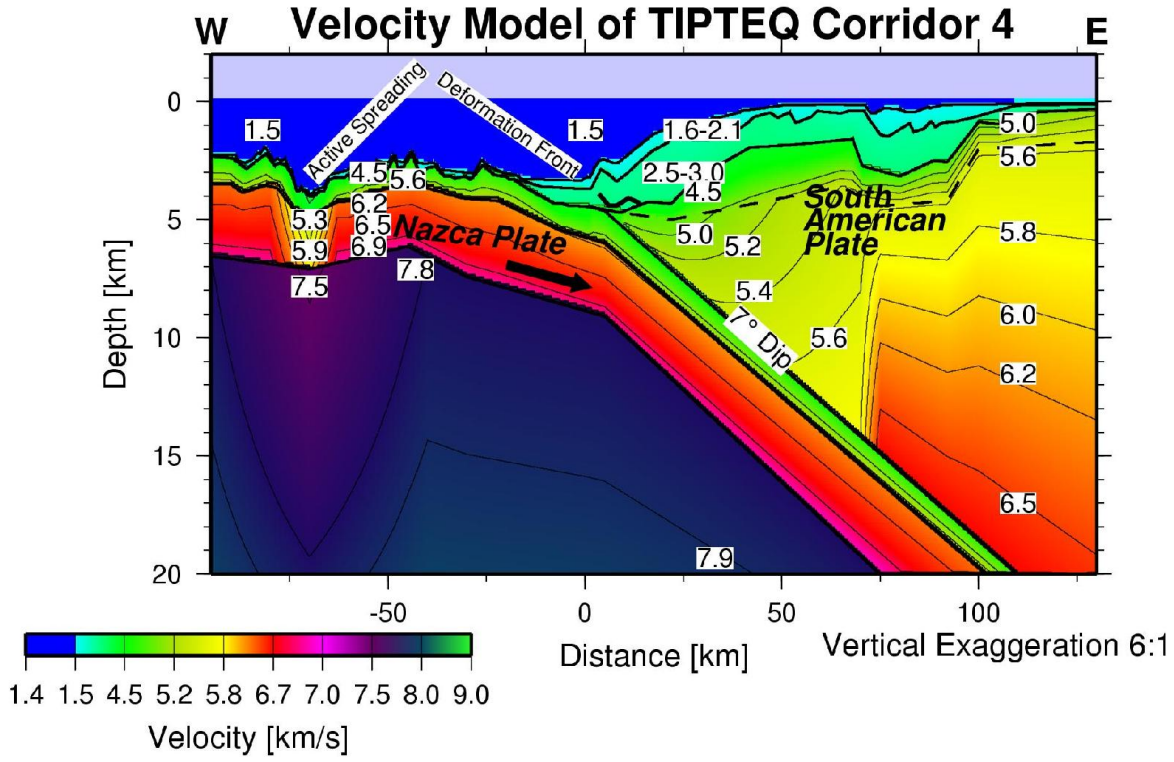

Abbildung B.5: Corridor 4 Geschwindingkeitsmodell (Martin Scherwarth pers. comm.)

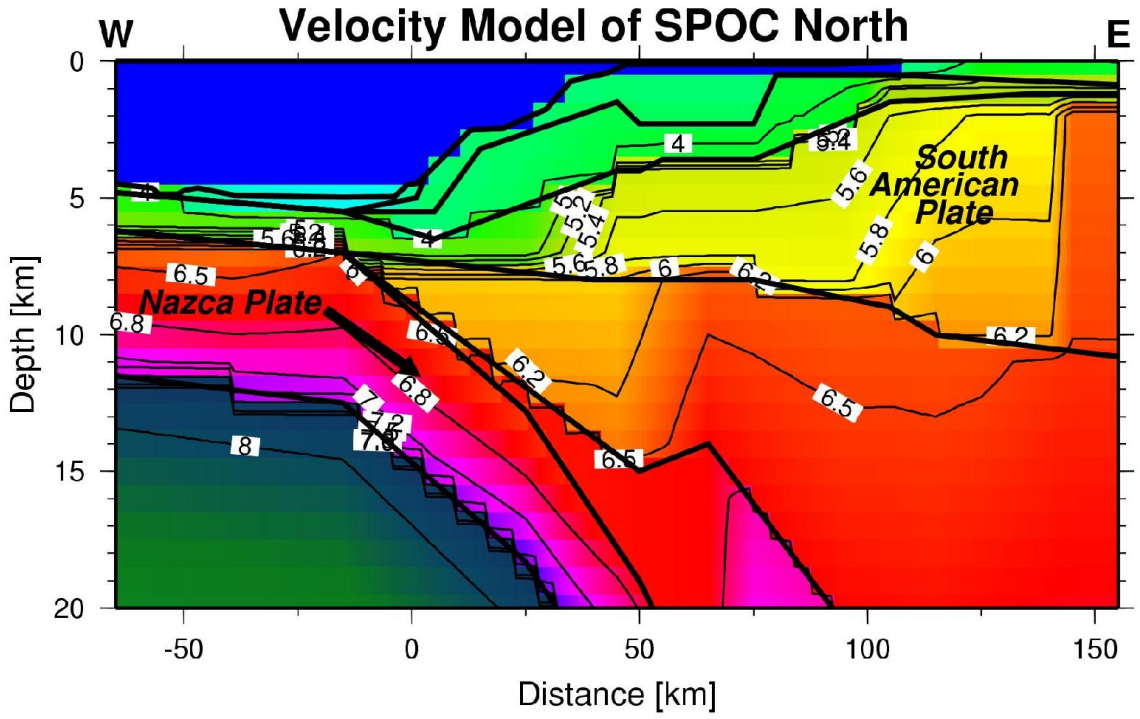

Abbildung B.6: Nördliches SPOC Profil bei 36.2°S (*The SPOC Team and Krawcyzk*, 2003)

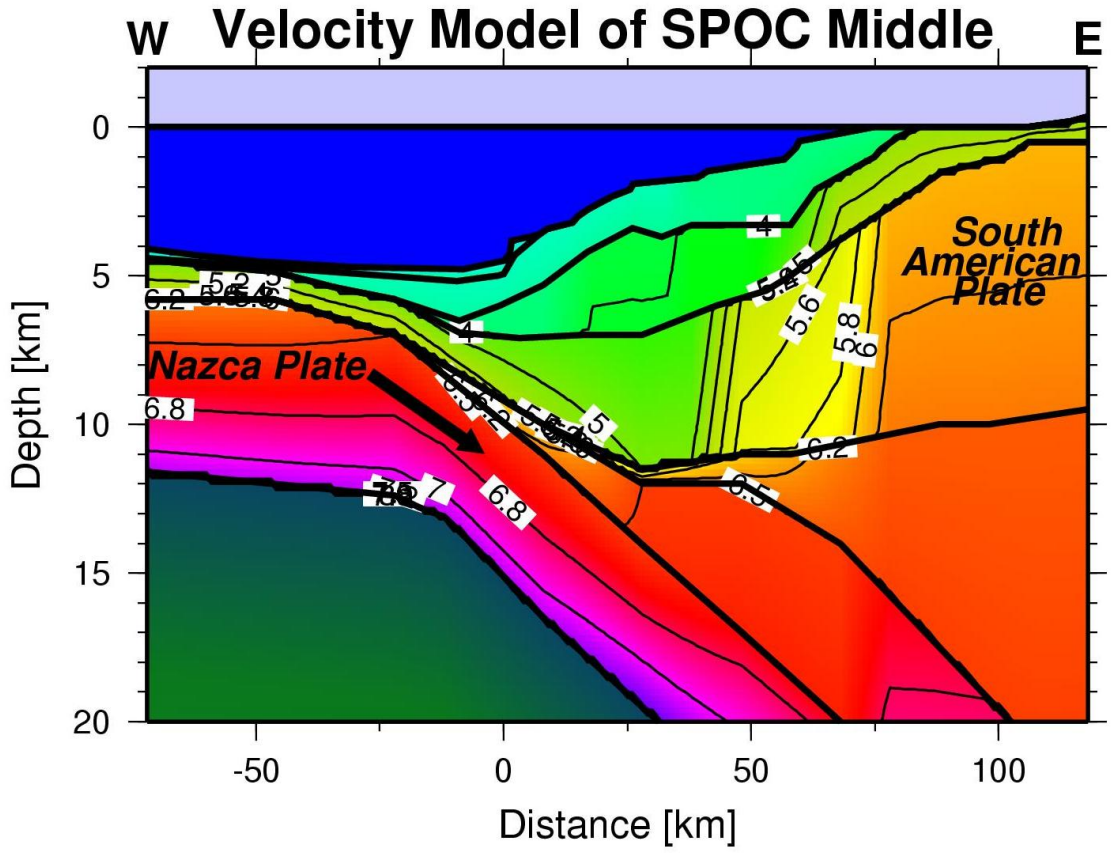

Abbildung B.7: Mittleres SPOC Profil bei 37.2°S (*The SPOC Team and Krawcyzk*, 2003)

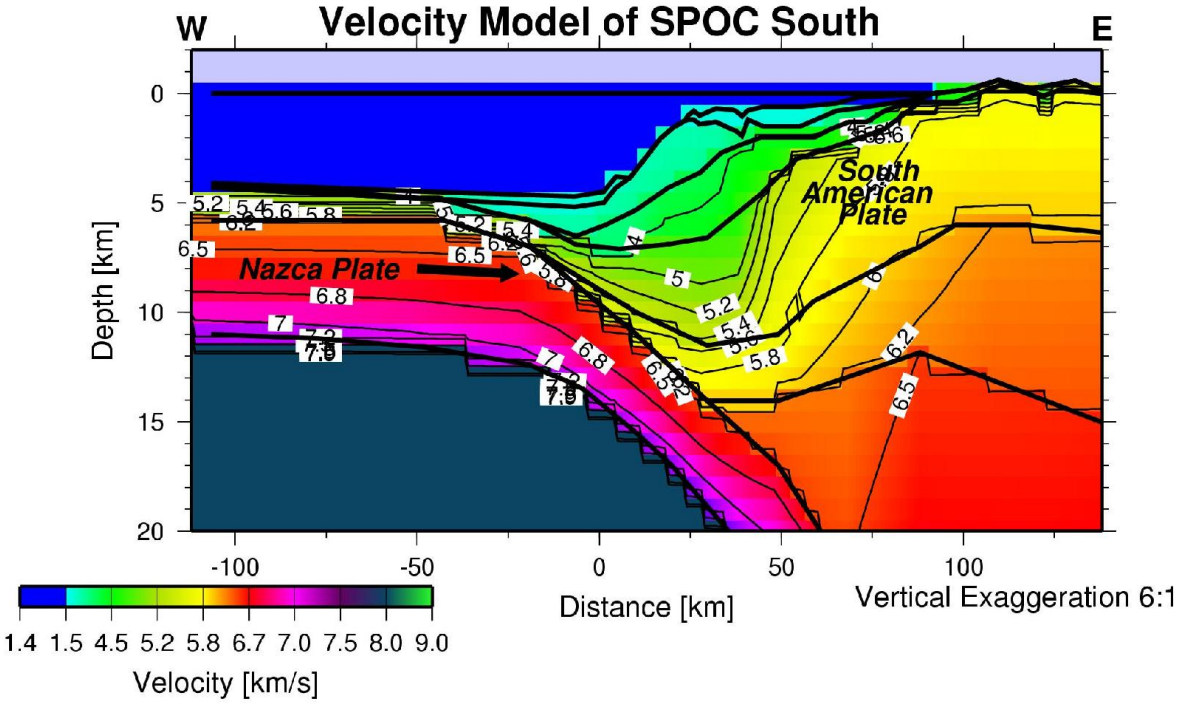

Abbildung B.8: Südliches SPOC Profil bei 38.2°S (*The SPOC Team and Krawcyzk*, 2003)

B.3 ODP Daten

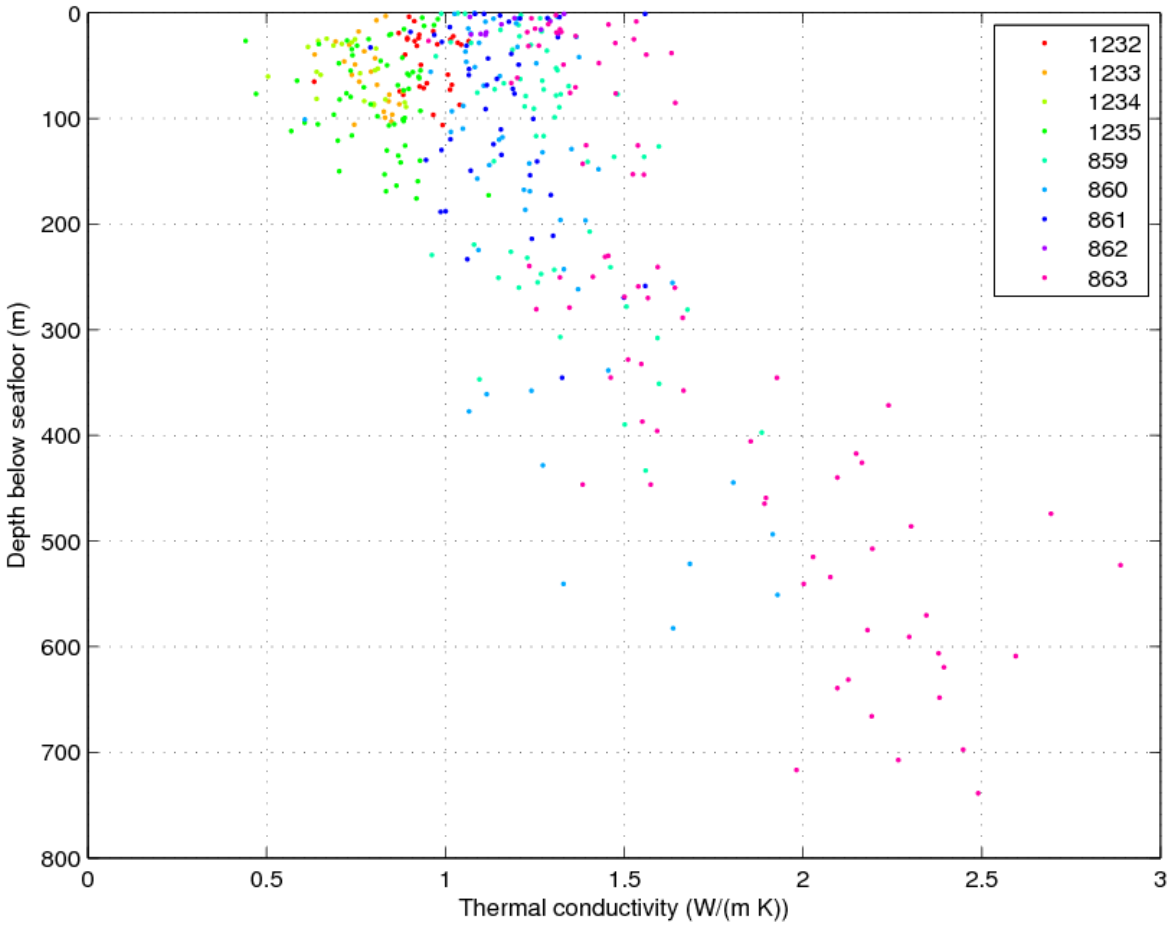

Abbildung B.9: Wärmeleitfähigkeiten an ODP Sites von Leg 141 und 202

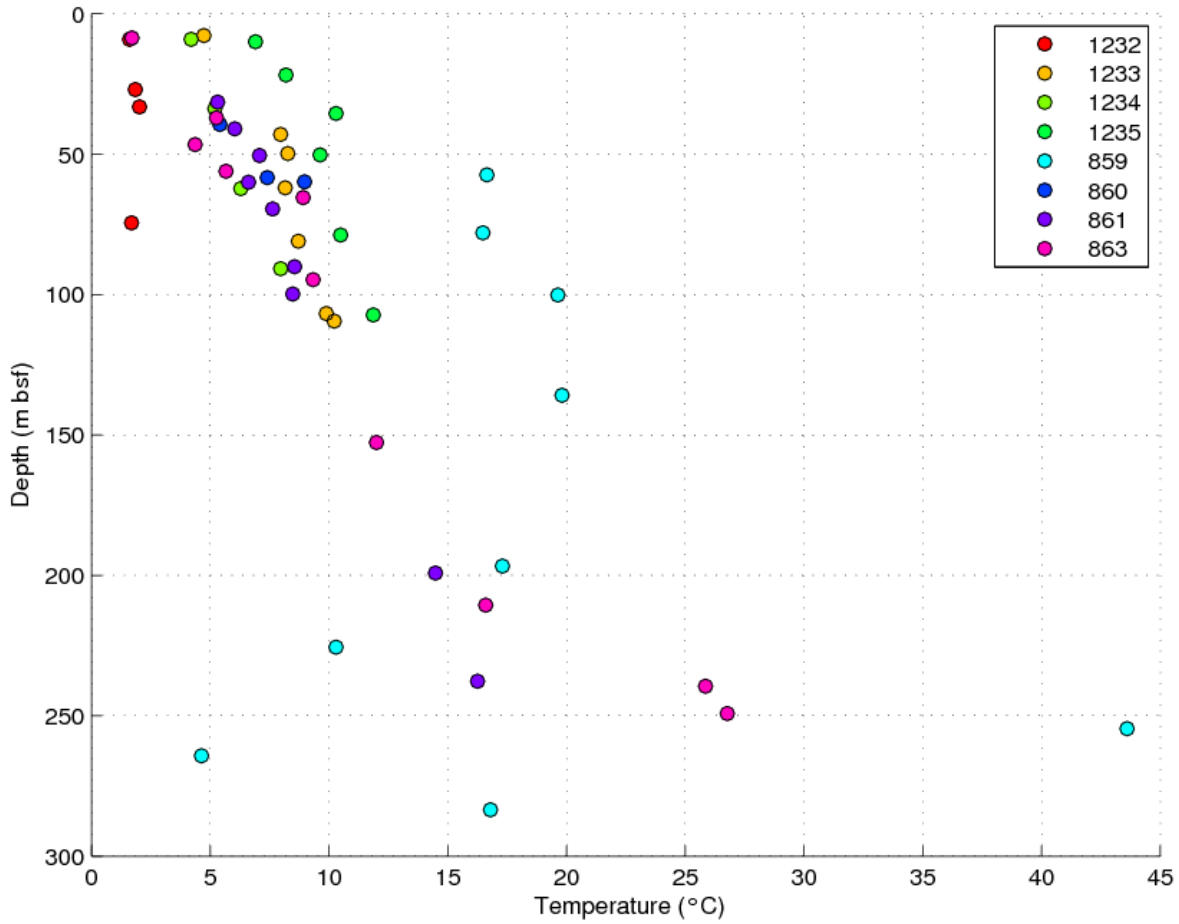

Abbildung B.10: Insitu Temperaturmessungen an ODP Sites von Leg 141 und 202

C Veröffentlichungen

C.1 Thermal constraints on the frictional conditions of the nucleation and rupture area of the 1992 Nicaragua tsunami earthquake

Artikel zur Veröffentlichung beim Geophysical Journal International eingereicht.

Thermal constraints on the frictional conditions of the nucleation and rupture area of the 1992 Nicaragua tsunami earthquake

Martin Heesemann [a,*], Ingo Grevemeyer [b], Heinrich Villinger [a]

[a] *University of Bremen*
Department of Geosciences
Klagenfurter Strae
28359 Bremen
Germany

[b] *IFM-GEOMAR*
Leibniz-Institute of Marine Sciences
Wischhofstr. 1-3
24148 Kiel
Germany

Abstract

The 1992 Nicaragua earthquake was a tsunami earthquake, which generated tsunamis disproportionately large for its surface wave magnitude $M_s = 7.2$. Seismological studies and tsunami simulation indicated that the event was a slow earthquake which occurred on the plate boundary between the subducting Cocos plate and the overriding Caribbean plate. We present a finite element model that enables us to estimate for the first time the temperature and inferred frictional conditions in the rupture area of a tsunami earthquake. Direct and indirect observations are used to constrain all model parameters, and surface heat flux measurements provide independent information to verify the model results. Furthermore, we used a genetic algorithm to perform a sensitivity analysis of all model parameters and to define the spatial range of thermally defined updip limit of the seismogenic zone. The earthquake nucleated in the seismogenic zone at temperatures of ∼150 °C and propagated up-dip toward the trench axis. The centroid or center of mass of moment release was located in a region characterized by temperatures of ∼50 °C. Thus, the rupture propagated through a region with velocity strengthening properties, where plate motion is normally accommodated by aseismic creep. Our observations support a model in which tsunami earthquakes nucleate in the seismogenic zone near its up-dip limit. However, in such an environment coupled asperities are perhaps too small to cause large earthquakes. Seamounts, however, are abundant on the incoming Cocos plate. Therefore, in addition to temperature-dependent metamorphic induration of sediments, increased normal stress by seamount subduction may contribute to accu-

mulate stress sufficiently large to release enough energy near the up-dip limit of the seismogenic zone to promote dynamic slip along a normally aseismic décollement all way to the ocean.

Key words: subduction, seismogenic zone, thermal state, genetic algorithm, finite elements

1 Introduction

Any great shallow subduction zone earthquake is expected to be followed by a substantial tsunami caused by the large displacement of water near the seafloor. However, a subclass of events called tsunami earthquakes excites considerably larger tsunamis than expected from its seismic magnitude Kanamori (1972). For instance, although they were much smaller in seismic moment magnitude (M_w), the tsunamis generated by two historic tsunami earthquakes, the 1946 Aleutian earthquake ($M_w = 8.2$) and the 1896 Sanriku earthquake ($M_w = 8.0$), produced devastating tsunamis of similar magnitudes as the 1960 Chile ($M_w = 9.6$), the 1964 Alaska ($M_w = 9.2$), and the 2004 Sumatra ($M_w > 9$) earthquakes (Geist, 2002; Geist et al., 2006).

Because of the discrepancy between seismic and tsunami magnitude, tsunami earthquakes are particularly dangerous. The 1896 Sanriku earthquake, for example, was felt only moderately along the Japanese coast, but very large tsunamis hit the coast ca. 30 minutes later and drowned more than 22,000 people. Due to the absence of strong ground motion, people did not evacuate to safe areas. Consequently, for disaster mitigation, it is particularly important to understand the processes governing tsunamigenic earthquakes.

To study tsunami earthquakes, the 1992 Nicaragua event is particularly well suited since it is the largest tsunami earthquake ($M_w = 7.7$, $M_t = 7.9$) ever recorded by global seismic broadband networks (Kanamori and Kikuchi, 1993; Satake and Tanioka, 1999). Digital data have been a treasure trove for detailed studies of seismic body waves, surface waves and tsunami simulation to calculate the nucleation and rupture history of the slow earthquake (Ide et al., 1993; Velasco et al., 1994; Satake, 1994; Ihmle, 1996a). Moreover, the convergent margin off Nicaragua and Costa Rica is well studied e.g. by numerous

* Corresponding author.
Email addresses: heesema@uni-bremen.de (Martin Heesemann), igrevemeyer@ifm-geomar.de (Ingo Grevemeyer), vill@uni-bremen.de (Heinrich Villinger).

deep sea drilling sites, active and passive seismic surveys, surface heat flux measurements, and GPS installations.

Compared to other thrust earthquakes, tsunami earthquakes usually have a longer source time function, and a slower and smoother rupture. Seismic body waveform inversions of tsunami earthquakes indicate shallow dipping thrust fault mechanisms (dip angle ∼6-10°), occurring at shallow depth (<15-20 km) near the trench axis and seaward of most other thrust zone events (Pelayo and Wiens, 1992). Overall, these observations suggest that the slow rupture results from seismic slip along a weak basal décollement cutting through shallow sedimentary rocks (Pelayo and Wiens, 1992). Due to the low rigidity of these sedimentary rocks, shallow thrust faulting will cause larger seismic slip and hence increase tsunami amplitudes (Geist and Bilek, 2001).

This interpretation contradicts the concept that subduction thrust earthquakes result from stick-slip frictional instability, as proposed by Scholz (1998). At shallow depth, unconsolidated sediments in the subduction thrust should cause stable sliding and hence prevent earthquake nucleation and rupture propagation. There is a transition from stable sliding to unstable stick-slip behavior at greater depths. This transition, defining the updip limit of the seismocenic zone, occurs when either the backstop of competent continental rock is reached (Byrne et al., 1988) or dehydration and metamorphic induration of the subducting sediments takes place at temperatures of 100-150 °C (Hyndman and Wang, 1993; Moore et al., 2001). Thrust earthquakes are expected in the stick-slip condition environment below the updip limit.

Accordingly, tsunami earthquakes may nucleate below the seismogenic updip limit with enough energy to dynamically propagate up-dip and cause slip along the normally aseismic basal décollement (Scholz, 1998; Seno, 2002). Alternatively, they may nucleate at shallow non-sedimentary asperities where seamounts or abyssal hills cause contact zones with the overriding plate (Polet and Kanamori, 2000; Bilek and Lay, 2002).

We developed a thermal finite element (FE) model to yield the thermal state of the coupling zone and hence to constrain the thermally defined updip limit of the rupture area. Firstly, we used the reported results of seismic and GPS surveys to constrain the model geometry. Secondly, model parameters were derived from physical properties measured at several Ocean Drilling Program (ODP) drill sites, previously reported seafloor heat flux data, and the sediment distribution on the subducting oceanic crust. Finally, new heat flux data, measured on the continental slope off Nicaragua, provided independent constraints for a genetic algorithm (GA), which we used to find model parameters in agreement with our data and to estimate the uncertainties in the computed thermal state of the rupture zone.

2 The 1992 Nicaragua Earthquake

The September 2, 1992 Nicaragua earthquake, which originated at the coupling zone between the subduction Cocos Plate and the overriding Caribbean Plate (cf. Figure 1), generated tsunamis that caused extensive damage on the Pacific coast of Nicaragua despite its moderate seismic surface wave magnitude of $M_s = 7.2$. Field surveys for seismic intensity and tsunami run-up height showed that the seismic intensity was small (III of the Modified Mercalli scale), but the tsunami run-up was ∼10 m above mean sea level (Baptisa et al., 1993; Satake et al., 1993) and caused at least 170 causalities.

The epicenter of the 1992 Nicaragua event, computed by the National Earthquake Information Center (NEIC), using short-period teleseismic data, is located near the shelf break, approximately 65-70 km from the trench axis (red star Figures 1, 2, and 6). Seismic body waveform inversion indicates a thrust faulting mechanism with a dip of 14-15° and a depth of ∼21 km (Ide et al., 1993). This corresponds roughly to the depth and dip of the plate interface as derived from reflection and refraction seismic data (cf. Figure 2) (Walther et al., 2000; Ranero et al., 2000). Due to the long duration and slow rupture velocity of the earthquake, seismologists observed differences of 45-52 s between the centroid time and the NEIC origin time (Kanamori and Kikuchi, 1993; Ide et al., 1993). Centroids represent the center of mass of moment release and are calculated from long-period surface waves. While short-period data indicates the nucleation area of the tsunami event, long-period data can be used to study the propagation of seismic slip. Ihmle (1996a) studied different wave bands and found that with decreasing frequencies centroids move toward the trench. The center of lowest frequency radiation is situated closest to the trench, about 40 km seaward of the NEIC epicenters, while intermediate frequencies centroids range between low frequency centroids and the epicenter (Figure 1B). Spectral inversion of long-period Rayleigh and Love waves (157-288 s) yield similar results, indicating a centroid location 54 km SW of the NEIC epicenter, at <10 km depth, with a fault zone dipping at ∼6° (blue star Figures 1, 2, and 6), and a predominant rupture azimuth of 140° (Velasco et al., 1994). The shallow depth and low dip angle correspond roughly to the geometry of the plate interface up-dip from the NEIC epicenters and supports rupture propagation toward the trench (Figure 2). Tsunami simulation supports the fact that rupture reached into the trench (Bilek and Lay, 2002; Satake, 1994).

Most aftershocks occur in a 40 km wide zone parallel to the trench (Figure 1), which stretches 100 km to the NW and 150 km to the SE of the epicenter (Ihmle, 1996a). Only a few events occurred seaward of the epicenter near the trench axis and available Harvard centroid moment tensor (CMT) solutions indicate normal faulting mechanisms. Thus, earthquakes near the trench axis

may represent intraplate events being related to bending of the subducting lithosphere rather than being related to earthquake processes in the subduction thrust. Nevertheless, large interplate earthquakes may affect the regional stress field and may therefore trigger intraplate earthquakes (Christensen and Ruff, 1983). Harvard CMT solutions of aftershocks further landward indicate thrust faulting mechanisms. In contrast to the mainshock, the aftershock distribution suggests that most events ruptured down-dip. It is important to note that the location of the aftershocks correspond well with the seismic front (Byrne et al., 1988; Newman et al., 2002), which marks the up-dip limit of the seismogenic zone. Byrne et al. (1988) suggest that the shallow subduction thrust seaward of the seismic front is velocity strengthening. Therefore, the mainshock propagated into a regime expected to be characterized by stable sliding (Scholz, 1998) and hence slip occurred along a normally aseismic and weak décollement.

3 The numerical model

To constrain the thermal updip limit of the seismogenic zone, we study the temperature of the décollement zone using a steady state FE model, which is based on the Comsol Multiphysics® toolbox, and Matlab®. The geometry of the FE model (Figure 2) is derived from time migrated and depth converted reflection seismic data, using velocities from focusing analysis (Ranero et al., 2000) and seismic refraction work (Walther et al., 2000). These data indicate two different main units building the continental margin: slope sediments and an underlying basement consisting of oceanic igneous rocks. Therefore, the model geometry is divided into three domains: a sedimentary layer (Seds), the continental basement (CnBs), and the subducting oceanic crust (OcCr).

The upper boundaries of the domains are approximated by cubic B-splines using a modified version of the "splinefit" script implemented by Nielsen (2005). B-splines offer a high level of flexibility during geometry assembly and avoid geometric singularities at the same time, by ensuring smooth boundaries (existence of continous second derivative). Then, a method described by Casciola and Romani (2004) is used to transform the B-splines into an equivalent series of cubic Bézier curves that can directly be handled by Comsol Multiphysics®. See Figure 2 for an illustration of the complete meshed geometry with 40914 degrees of freedom, and 20289 triangular elements.

The 2D-model is based on the non-conservative steady state heat conduction and advection equation

$$\nabla \cdot (-k\,\nabla T) = Q - \rho c_p\,\vec{v} \cdot \nabla T \tag{1}$$

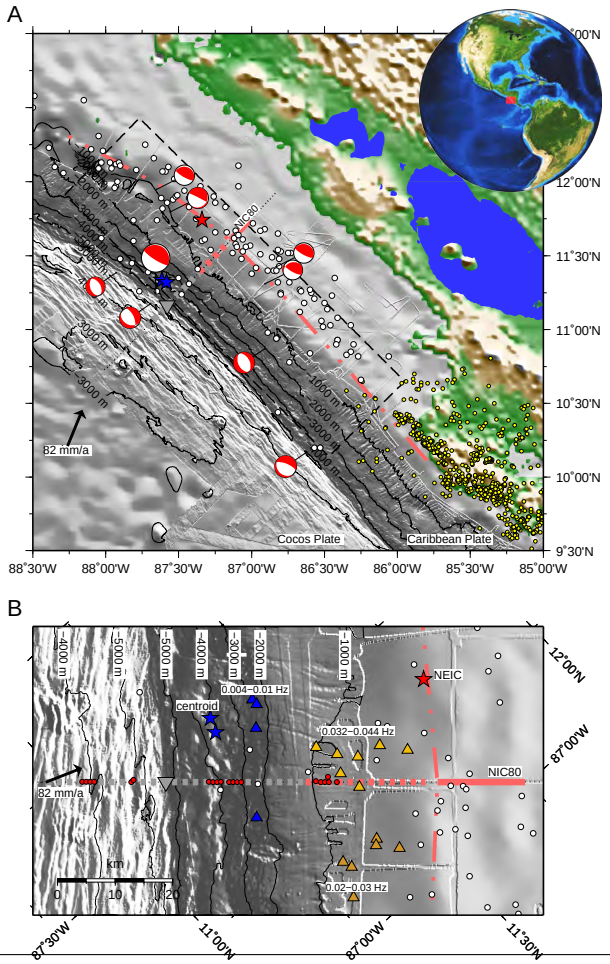

Final figure should cover whole page with caption on opposite page

Fig. 1. Artificially illuminated seafloor relief in the area of the 1992 Nicaragua tsunami event. The red star is the NEIC epicenter, indicating the area where the rupture started. Blue stars are centroids (Newman et al., 2002; Velasco et al., 1994). The aftershocks (white circles) relocated by Ihmle (1996a) occurred in a three-month period following the main event. The first part of model transect (NIC80) is marked by dashed gray line. At model temperatures >100 °C the line turns red and model temperatures >150 °C are marked by a solid red line. The 150 °C isotherm is extrapolated to both sides of the transect. A. The moment release within the slip area (boxed region) (Ihmle, 1996b) was used for tsunami simulation (Geist and Bilek, 2001). Harvard CMT solutions, which have been assigned to relocated events, are shown for the main shock and largest aftershocks. Yellow dots are earthquakes relocated by (Newman et al., 2002). B. The triangles are spatial centroids (Ihmle, 1996a), illustrating the slow rupture process; with decreasing frequency spatial centroids moved further trenchward. Small red dots on the seismic profile (Walther et al., 2000) mark locations where heat flux measurements were obtained during the RV Meteor cruise M54-2. The arrow illustrates the velocity of the Cocos Plate with respect to the Caribbean Plate.

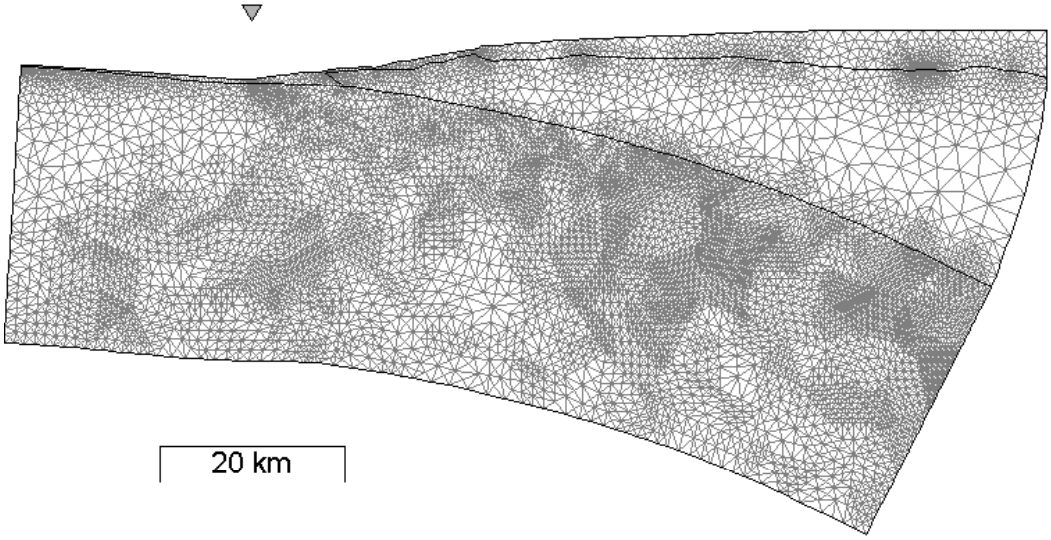

Fig. 2. Complete geometry and mesh of the FEM model. The mesh, shown without vertical exaggeration, consists of 20289 triangular elements and has 40914 degrees of freedom. The triangle above the geometry marks the location of the deformation front.

which assumes incompressible flow and ensures that no unphysical source term arises from a flow field where the incompressibility constraint is not absolutely fulfilled (Comsol, 2005, pp. 162). Hence, the temperature distribution in the model domains depends not only on the geometry but also on the boundary conditions at the edges of the domains, the thermal conductivity (k), the volumetric heat capacity (ρc_p), the heat production (Q), and the velocity ($\vec{v}$) determining the advective heat transport.

3.1 Parameter constraints

Since all model parameters interact and influence the temperature distribution at the décollement, it is important to constrain them as good as possible by direct and indirect observations. Defining the velocity field, we assume that the Cocos Plate subducts beneath a stationary Caribbean Plate and computed a convergence rate of 82 mm/a, using the Plate Motion Calculator (UNAVCO, 2006) and the corresponding rotation pole published by DeMets (2001). Accordingly, the OcCr is the only domain with advective heat transport and the magnitude of its velocity (78 mm/a) is given by plate velocity component that is parallel to the model transect (cf. Figure 1B). The direction of the modeled velocity field is parallel to the upper boundary of the oceanic crust.

The thermal properties and the boundary conditions of the OcCr domain are based on global models of oceanic crust cooling histories evaluated by Stein

and Stein (1992). We chose the half space cooling model

$$T(t,\ z) = (T_i - T_{sf})\mathrm{erf}\left(\frac{z}{2\sqrt{\kappa\ t}}\right) \tag{2}$$

with

$$\kappa = k/(\rho c_p)$$

to prescribe the temperature field at the seaward and lower boundaries of the 24 Ma old (Barckhausen et al., 2001) subducting oceanic crust. Following values for the model parameters were reported by Stein and Stein (1992): $k = 3.138\,\mathrm{W/(m\,K)}$, $c_p = 1.171\,\mathrm{kJ/(kg\ K)}$, and $\rho = 3330\,\mathrm{kg/m^3}$. Furthermore, no heat production in the OcCr domain, and an initial crust temperature T_i of 1450 ℃ and a constant seafloor temperature T_{sf} of 0 ℃ are assumed.

We adopted these parameter values, constrained by global heat flux and bathymetry data (Stein and Stein, 1992), except for the temperature of the upper oceanic crust. Harris and Wang (2002) found that it is important to modify this simple half space cooling model to account for advective cooling of the upper oceanic crust by circulating seawater. This is especially important in models that are designed to investigate the frontal part of the subduction zone including the updip limit of the seismogenic zone. Having a closer look at the oceanic crust – seawater interface, there are two facts that deviate from the assumption of a constant temperature of 0 ℃. Firstly, we observed bottom water temperatures of 2 ℃ during our heat-flux measurements. Secondly, the oceanic crust is not in direct contact with the water column but insulated with a blanket of sediments and cooled by fluid advection beneath the cover at the same time. To account for the first observation, one can add 2 ℃ to all temperatures in the model. To include the second observation, we calculated the temperature difference between bottom water and oceanic crust - sediment interface (ΔT), assuming the heat transfer in the sediments to be purely conductive, by using Fourier's law of conduction:

$$q = k\,\Delta T/\Delta z \iff \Delta T = q\ I \tag{3}$$

Here, k is the thermal conductivity, Δz the thickness of the sediments, q the surface heat-flux, and I the thermal insulance, the quotient of Δz and k. The depth dependency of I (Fig. 3B) was computed based on the geometric mean thermal conductivities (Fig. 3A) of sediments covering the subducting oceanic crust segment. The thermal conductivities were measured on split cores from ODP Sites 844, 845 (Mayer et al., 1992), and 1256 (Wilson et al., 2003), the locations of which are shown in Figure 4. Along with abundant heat-flux data from (Vaquier et al., 1967; Bookman et al., 1972; Sclater et al., 1970; Langseth

et al., 1971) that is included in the global heat-flux compilation of Pollack et al. (1992) (Fig. 3C), and sediment thickness data (Fig. 3D) published by Divins (2005), the local thermal insulance was used to compute temperatures at the sediment – basement interface (Fig. 3D), assuming a constant bottom water temperature of 0 °C.

Estimated averages over time of the computed temperatures are used to prescribe the temperature of the upper OcCr boundary until it reaches the deformation front. Past the deformation front, a continuous boundary condition is applied, assuming the ceasing of advective circulation in the upper oceanic crust when it is subducted. Note that in the model surface heat flux values seaward of the deformation front are used as boundary conditions and cannot be used to verify the model by comparison to field measurements.

The thermal properties of the Seds and CnBs domains are derived from measurements at three ODP Sites (Fig. 5). Thermal conductivities were directly measured on cored material whereas the rate of radiogenic heat production (Q_r) is computed using downhole logging data and the empiric equation

$$Q_\mathrm{r}\,[\mu\mathrm{W/m^3}] = 10^{-5}\rho(9.51c_\mathrm{U} + 2.56c_\mathrm{Th} + 3.48c_\mathrm{K}).$$

Here, ρ is the rock density (kg/m^3), c_U (ppm), c_{Th} (ppm), and c_K (wt%) are radioactive-element contents (Buecker and Rybach, 1996; Grevemeyer et al., 2003). Density data is provided by the Hostile Environment Lithodensity Tool (HLDT), and the contents of the radioactive-elements were measured using the Natural Gamma Ray Spectrometry Tool (NGT).

In the data, the Seds domain is represented by a ∼150 m thick section of slope sediments which is probed ∼1 km landwards of the Middle America Trench off Costa Rica at ODP Site 1040 (Kimura et al., 1997) (cf. inset Fig. 4). The CnBs domain, which presumably consists of oceanic igneous rocks, is represented by two ∼70 m and ∼390 m thick sections of oceanic basement penetrated at ODP Sites 1253 (Morris et al., 2003), and 1256 (Wilson et al., 2003), respectively. The oceanic rocks at Site 1253 are recovered from two different intervals: a 30 m thick upper igneous unit (gabbro sill), and a 40 m lower igneous, separated by a 30 m thick sedimentary unit.

3.2 Initial model

We used the parameter constraints, derived in the previous section and summarized in Figures 3 and 5, to define a set of parameters for an initial model and a constraining range for each model parameter both shown in Table 1. Surprisingly, all values of our initial model parameters are notably lower than used

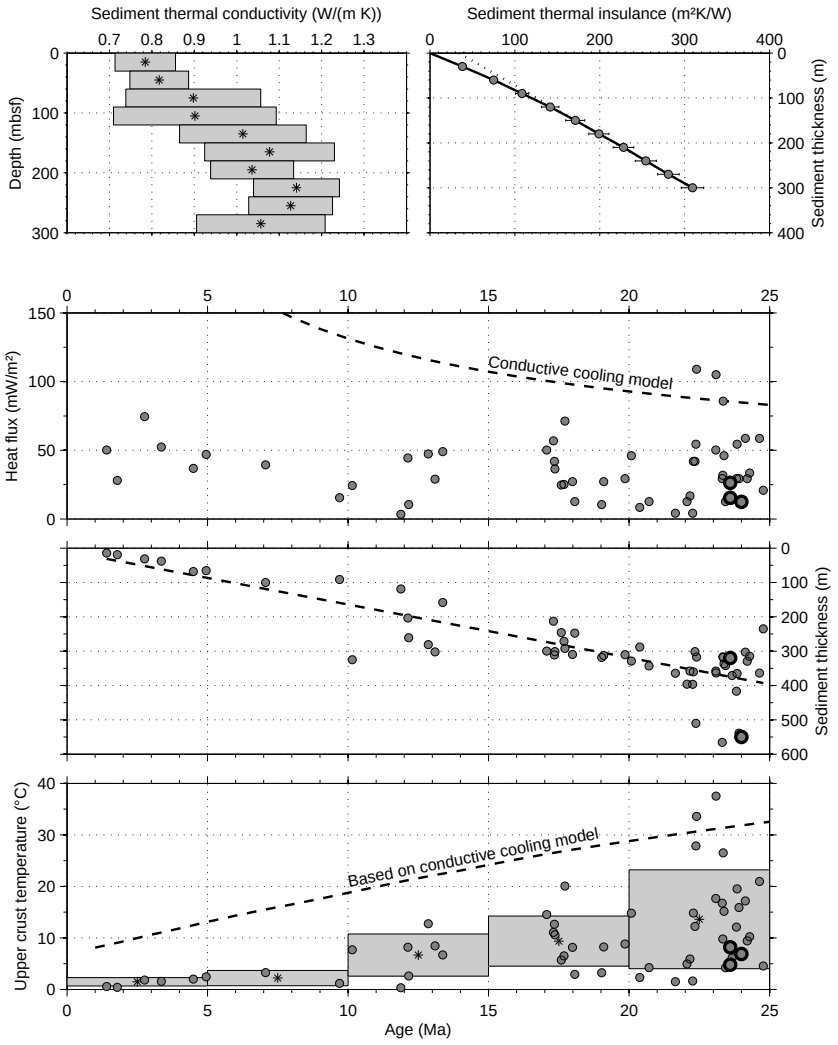

Fig. 3. A. Mean (stars) and standard deviation (boxes) of thermal conductivities measured in sedimentary sections of ODP Sites 844, 845 (Mayer et al., 1992), and 1256 (Wilson et al., 2003). B. Mean thermal insulance of the sedimentary column at the ODP Sites. Errors are derived from standard deviation of thermal conductivities. The fit of dotted line is used for linear extrapolation of the thermal insulation to greater sediment thicknesses. C. Heat-flux measurements on the subducting Cocos Plate, reported by Pollack et al. (1992) (plain symbols) and Grevemeyer et al. (2005) (bold symbols), vs. the crustal age (Barckhausen et al., 2001). D. Thickness of sediment cover at the locations of the heat-flux measurements. If not otherwise available the sediment cover is interpolated using global data published by Divins (2005). E. Temperatures at the sediment-basement interface (filled symbols) are the product of the conductive surface heat flux (C.) and the thermal insulance of the sedimentary column (B.) with the thickness (D.) at the specific location. Stars and boxes show the binned mean values and standard deviations of the upper crust temperatures. The dashed line represents the temperatures that would results from a conductive cooling model (C.) and a linearly increasing sedimentary column (D.).

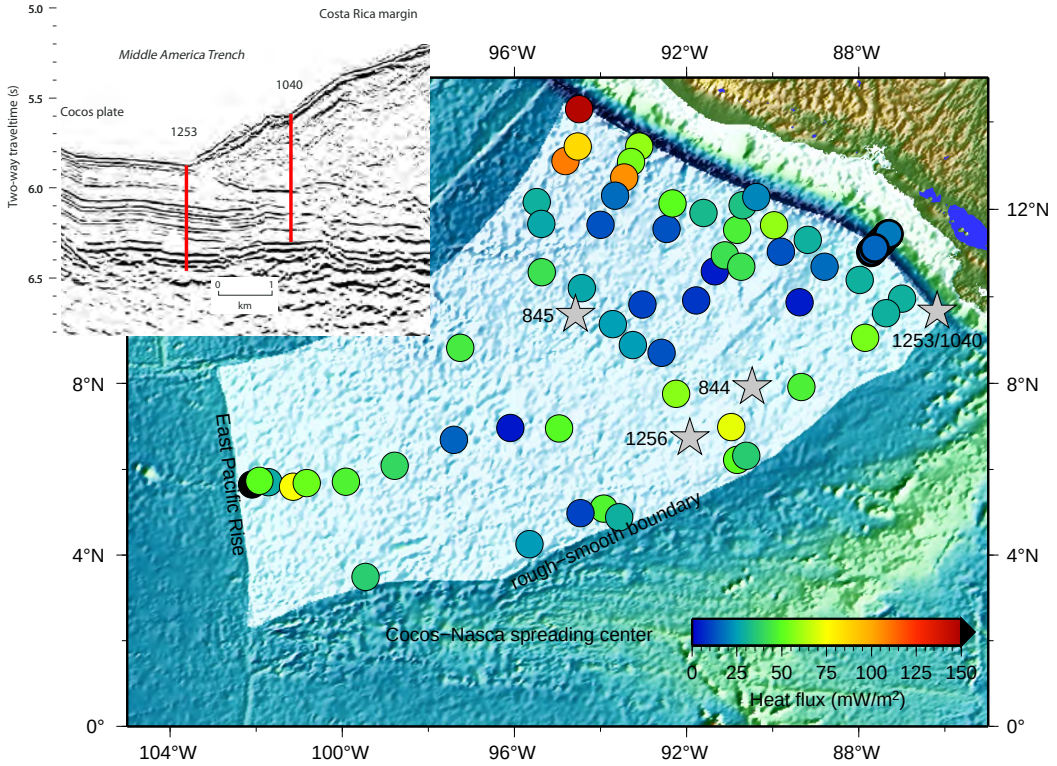

Fig. 4. Locations of ODP Sites and seafloor heat flux measurements over elevation model (NGDC, 2005). Inset shows detailed locations of ODP Sites 1253 and 1040 off Costa Rica. The oceanic crust segment that originates from the East Pacific Rise and subducts off Nicaragua is highlighted.

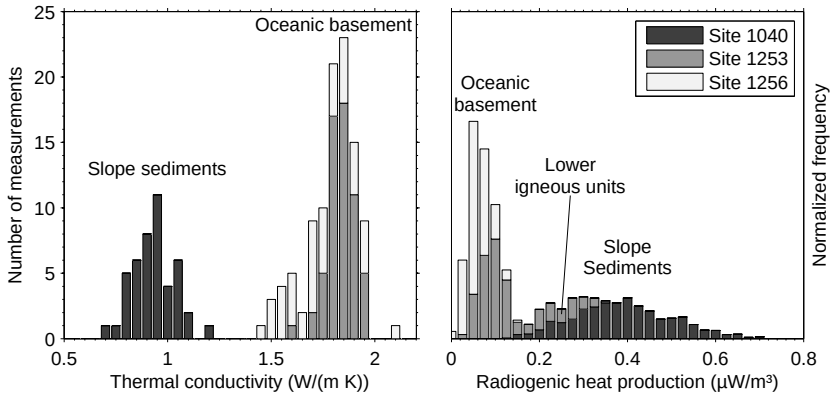

Fig. 5. Thermal conductivies measured on core-samples (A) and radiogenic heat production derived from downhole logging data (B) at three ODP Sites (cf. Fig. 4).

by other authors in similar models. As an example, the parameters used by Harris and Wang (2002) for a thermal model of the subduction zone off Nicoya Peninsula, Costa Rica, are listed in Table 1. Measured surface heat flux values on the subduction plate are exceptionally low (Langseth and Silver, 1996), signaling low upper oceanic crust temperatures, and new measurements on our modeled transect are even below the regional average (see Fig. 3). More-

over, average sediment thermal conductivies below 1 W/(m K) are lower than usually found in ODP boreholes (cf. supplementary material Figure A.1), and finally the thermal conductivity and radiogenic heat production values of the igneous oceanic rocks that are believed to build the continental basement are much lower than found in usual continental basement. Therefore, parameter values for the CnBs domain often used by other authors are beyond of our constrained range. To verify the chosen parameters, we compared surface heat flux values computed with our initial parameter set (Fig. 6A), as well as with the parameters used by Harris and Wang (2002) (Fig. 6B), to new heat flux data from the continental slope.

During RV Meteor cruise M54-2 in summer 2002, we obtained 25 surface heat flux measurements on the continental slope off Nicaragua (Grevemeyer et al., 2005). 15 of these measurements are located on our modeled transect, the seismic multi-channel line NIC80, shot with a 6-km steamer in 2000 by the University of Texas at Austin. Two different heat flux probes of violin bow design (Hyndman et al., 1979) were used to acquire the data. The instruments have 11 and 22 thermistors, which are spaced in 0.27 m intervals and mounted inside an oil filled hydraulic tube that penetrates into a sedimented seafloor. Thus, the probes are able to obtain thermal gradients over a length of 3 and 6 m, respectively. Both probes are equipped with on-line data transmission for operation control and independent data storage inside the instrument for double data security. During every other probe penetration, in situ thermal conductivity measurements were made by applying a 20 s pulse of electric current along heater wires within the tubing. The recorded temperature decays caused by this calibrated heat pulse allow to estimate the thermal conductivities of the sediments surrounding temperature sensor (Hartmann and Villinger, 2002).

In addition to measurements with the heat-flux probes, thermal gradients were measured by autonomous temperature loggers (Pfender and Villinger, 2002) mounted on gravity corers. Thermal conductivities from the recovered core material have been measured using needle probes von Herzen and Maxwell (1959), which were inserted into undisturbed areas of split cores. After penetration into the sedimented seabed, the sensors record a pulse of frictional heating which decays while the tools remains in the seafloor for 7–10 min. Then, temperatures and thermal conductivity measurements are jointly inverted to obtain the surface heat flux. Individual heat flux values and the number of temperature measurements used to derive the thermal gradients are published in Grevemeyer et al. (2005).

In addition to the measured heat flux data, we calculated seafloor heat flux values from bottom simulating reflectors (BSR), which were imaged on the middle part of the slope off Nicaragua. Due to the uncertainties in the absolute magnitude of the BSR-derived heat flux values, we used the procedure

Table 1
Parameters and results of selected models. Numbers in parentheses in the highlighted lines result from the other given ranges. All misfit values, except for the Harris and Wang (2002) model, are in respect to the scenario with low BSR derived heat-flux values.

Domain	Variable parameters					Results			Reference
	OcCr	CnBs		Seds					
	T_{in} (°C)	k (W/(m K))	Q (μW/m³)	k (W/(m K))	Q (μW/m³)	$x_{100°C}$ (km)	$x_{150°C}$ (km)	Misfit (mW/m²)	ID #
Constraints	0 – 20	1.8 – 2.2	0 – 0.4	0.8 – 1.2	0.2 – 0.6	(30.0 – 38.5)	(60.7 – 73.9)	0 – 2.5	
Initial model	7.0	1.90	0.1	1.00	0.4	35.0	68.9	2.1	1
Best Model	10.0	1.90	0.1	1.15	0.5	34.6	68.4	1.2	1986
Shallow model	18.0	1.80	0.3	0.90	0.5	30.0	60.7	1.6	534
Deep model	0.0	2.15	0.1	1.00	0.4	38.5	73.9	1.9	1173
GA range	0 – 40	0.6 – 3	0 – 2.5	0.6 – 3	0 – 2.5	(16.3 -45.6)	(39.3 – 79.7)	(0.9 – 21.5)	
Best fit	21.5	1.60	0.2	1.80	0.0	31.3	62.8	0.9	3795
Harris & Wang	7.0	2.70	1.5	1.20	0.6	35.5	62.2	7.9	2039

described by Grevemeyer and Villinger (2001) to calibrate the data with heat flux probe measurements at the same location. Unfortunately, this calibration is ambiguous since our relevant heat flux probe measurements, located ∼40 km landward from the deformation front, can be categorized into two distinct groups. Consequently, we considered two calibrations with surface heat flux values which represent endmembers of the measured data: scenario one based on the lower heat flux values (6A), and scenario two based on higher values (6B).

Our initial model provides an excellent fit to the first scenario (Fig. 6A), while the model parameters used by Harris and Wang (2002) favor the second scenario (Fig. 6B). The good fit with the initial model and the fact, that the spatially spread out group of lower heat flux values is more likely to represent an undisturbed background, whereas the group of higher heat flux values appears to be a localized anomaly, support the first scenario. Nevertheless, we designed a set of numerical experiments based on a genetic algorithm (GA) to test each scenario and to determine the uncertainties in the modeled temperature distribution on the plate interface.

3.3 Genetic algorithm

The term genetic algorithm (GA) refers to a family of computational codes that are inspired by evolutionary processes. GAs are often used in function optimization, even though the range of possible uses is much broader (Whitley, 1994). We chose a GA, because it allows us to find a whole range of optimized solutions while exploring the parameter space in a relatively short period of time. To solve a problem using a GA, a chromosome-like data structure has to be defined which is capable to represent all possible solutions. Then, evolutionary operators are applied to consecutive generations of chromosome sets in order to iteratively increase the overall fitness of the generations. We defined a chromosome as a vector of five floating point numbers containing the variable model parameters, namely the temperature of the upper oceanic crust seawards of the deformation front (T_{in}), the thermal conductivities and heat

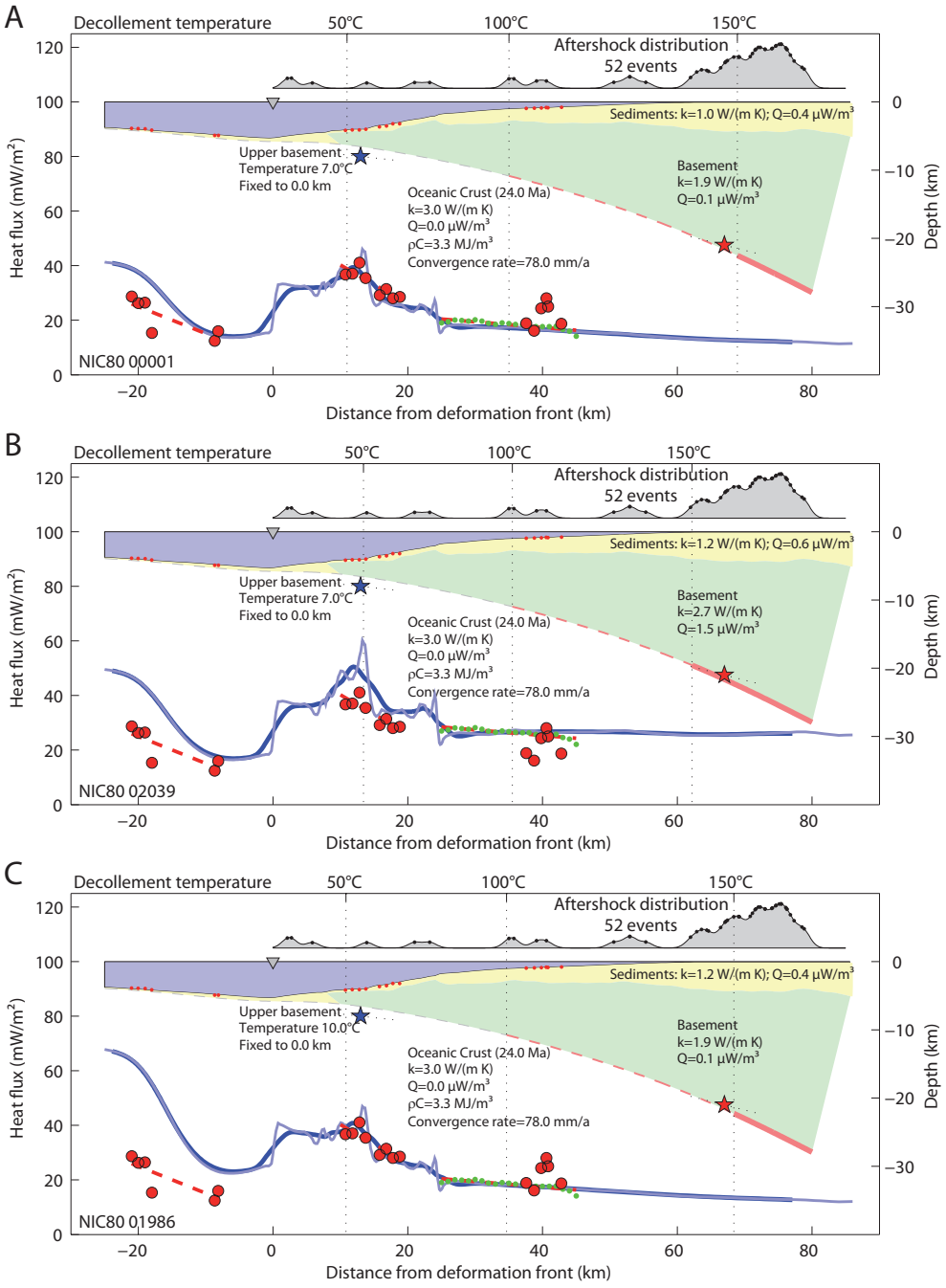

Fig. 6. Results from model runs using different sets of parameters used for the three model domains. Smoothed model surface heat-flux values (dark blue line) are compared to measured values (red circles) and estimates from BSR depth (green dots). Locations of the heat flux measurements with respect to the model geometry are shown as red dots. A. Initial model based on parameters constrained by parameter observation. B. Model with parameters chosen by Harris and Wang (2002). C. Model found by GA which keeps all parameters in the constrained range and provides a good fit with surface heat-flux data at the same time

production rates of the Seds and the CnBs domains. The allowed range for each parameter (cf. GA range in Table 1) is intentionally chosen much wider than we expect from the parameter constraints provided above. This allows the GA to test solutions that deviate from our expectations.

The algorithm starts with a random initial generation consisting of 100 chromosomes which is subdivided into 5 populations of 20 chromosomes each (Fig. 7). Consecutively, the fitness of each chromosome is evaluated by the subprocess "Compute objectives". The returned objective value depends on the intention with which each of the experiments, described below, is designed. However, the misfit between measured heat flux data and the heat flux values computed using the FE model is always a basic component of the objective value. The fit is done using pieces of linear approximations (red dashed lines in Figure 6) of the measured surface heat-flux data to prevent weighting effects of unevenly distributed data and "locking" of spikes, present in the modeled data between measured data points. An example for "locking" being an issue are the heat flux probe measurements at ∼10 km from the deformation front shown in Figure 6A. The subprocess also keeps a record of evaluated chromosomes in order to avoid multiple evaluations of a FEM model with the same set of parameters, since the model runs, lasting ∼30 s each, are demanding most of the computational time.

Choosing parameters controlling the evolutionary operators provided by the Genetic Algorithm Toolbox for use with Matlab (Chipperfield et al., 1994) involves a trade off between fast convergence of the GA with a single possibly locally optimal solution, and a broader exploration of the parameter space. In our experiments, we favored a broader exploration, since we are interested in the whole range of parameter combinations that solve our problem within the given constraints rather than in a single theoretically best solution.

As shown in Figure 7, each iteration starts with a ranking of the individual chromosomes which is based on their objective value. Using this ranking, individuals within the different subpopulations of the current generation are selected and recombined to produce a pool of 80 children. Following, some of the generated children are randomly changed by the mutation operator to enhance the genetic diversity. The newly generated children are then rasterized, by rounding, to a discrete parameter grid so that negligible parameter variations are mapped onto the same chromosome. After several iterations, this procedure dramatically reduces the number of new FE models that have to be evaluated in each iteration, without loosing a significant amount of information.

Then, a number of children is selected which is reinserted into the parent generation by replacement. Conditionally, some individuals are exchanged between subpopulations by the migration operator in case the generation counter,

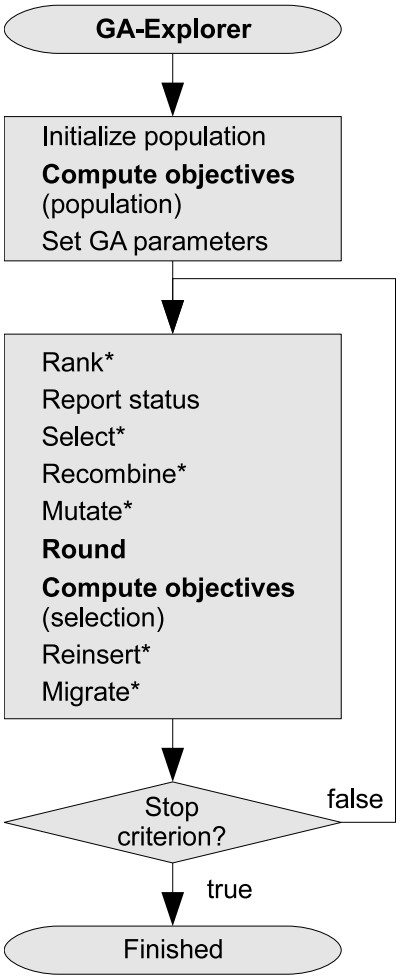

Fig. 7. Genetic algorithm used to explore the parameter space of the finite element forward model. Standard evolutionary operators (e.g. Whitley, 1994), which are tagged above (*), are based on functions from the genetic algorithm toolbox by Chipperfield et al. (1994), while we specifically developed the operators in bold font to reduce the number of forward model evaluations.

which is increased with every iteration, reaches predefined levels. Finally, the next iteration step is initiated unless a stop criteria is fulfilled. The stop criteria used by us depend on the amount of computational time has passed, and on the generation diversity. A diversity below a certain threshold indicates that the GA converged against a single solution.

4 Numerical experiments

In a first numerical experiment, we tried to discriminate the two scenarios where the BSR derived heat flux values are calibrated with the lower or the higher heat flux probe measurements. To do this, we applied the GA two consecutive times with different objective functions. The two objectives were to

minimize the misfit between the modeled surface heat flux and the observed values in respect to the different scenarios. The parameter and result distributions of this and the following numerical experiment are jointly shown in Figure 8.

Models that represent the low heat flux scenario are represented by white and black bar segments. Black segments contain models that fit the scenario with a maximum average misfit of 2.5 $\mathrm{mW/m^2}$ (gray area in the Fit panel), while white bar segments represent the models that additionally fall into the constrained range of all model parameters (highlighted areas in the parameter panels correspond to constraints listed in Table 1). One example for a model that is represented by a white bar segment (good model) is our initial model, which is marked by solid vertical lines in Figure 8. The solid lines are within the gray areas of all panels. Also the two models that result in smallest and biggest distance of the 150 °C isotherm from the deformation front (listed as deep and shallow in Table 1) while meeting all constraints at the same time are therefore represented by white bar segments.

Having a look at the black segments, it appears that the low heat flux scenario is satisfied by a wide range of models within the parameter constraints as well as going much beyond them. Actually, the model that provides the best fit to the low heat flux scenario (cf. Table 1) is represented by a black bar segment, since it is based on a very unlikely parameter combination, where the Seds thermal conductivity (1.8 $\mathrm{W/(m\,K)}$) is higher than of the CnBs (1.6 $\mathrm{W/(m\,K)}$). Moreover, it is evident that the low heat flux scenario is best satisfied by models with low CnBs thermal conductivities. Values exceeding 2.5 $\mathrm{W/(m\,K)}$, expected for regular continental basement, are not conform with the low heat flux scenario.

Models that meet the high heat flux scenario within a maximum mean misfit of 2.5 $\mathrm{mW/m^2}$ are symbolized by dark gray bar segments, and models with a misfit exceeding 2.5 $\mathrm{mW/m^2}$ in respect to either heat flux scenario (i.e. the model represented by the dashed lines (Harris and Wang, 2002)) are shown as light gray bar segments. Having a look at the dark gray bar segments, it turns out that models satisfying the high heat flux scenario generally provide a slightly poorer fit to measured data than models that represent the low heat flux scenario (white and black segments). Moreover, the high heat flux scenario requires unreasonable Seds thermal conductivities which are greater than 2.5 $\mathrm{W/(m\,K)}$. Since there are no known sediments with thermal conductivities exceeding 2.5 $\mathrm{W/(m\,K)}$ (cf. A.1 in supplementary materials), we reject this scenario.

Having rejected the high heat flux scenario and verified that models that comply with our parameter constraints are able to reproduce the measured surface heat flux values, we modified the objective function to study the uncertainty

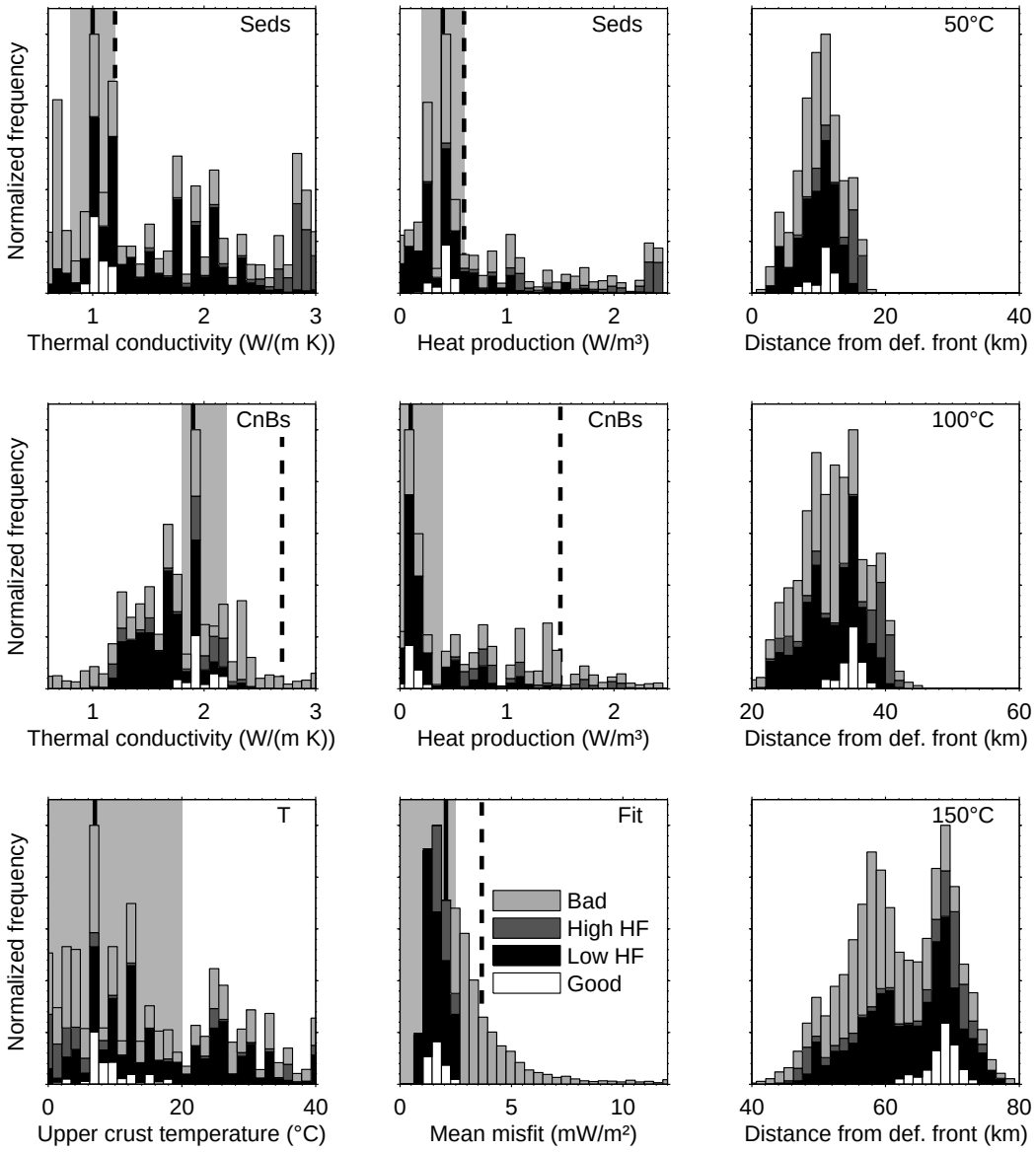

Fig. 8. Parameter and result distributions including all 7014 solutions obtained during different numerical experiments. White segments represent good models, which satisfy all constraints highlighted (gray areas) in the six panels of the first two columns. Black and dark gray segments satisfy only the constraint highlighted in the Fit panel in respect to the low and the high heat flux scenario, respectively. Models that do not meet the Fit criteria are symbolized by light gray segments. The solid vertical line represents the parameters of our initial model, while the dashed lines show the parameters chosen by Harris and Wang (2002).

in the model results. To do this, we altered the objective function of the first scenario by adding a penalty for chromosomes containing model parameters that are beyond the range of the parameter constraints. Doing this, more good models, complying with the parameter constraints and fitting the measured heat flux data at same time (white bar segments), are generated during the iterations of the GA. These additional models provide a good estimate about

Table 2
Spearman correlation coefficients of correlation between model parameters and resulting distances of intersection between the 50 °C, 100 °C, and 150 °C isotherms with the plate boundary sorted by magnitude of correlation.

	T_{in}	kCnBS	kSeds	QCnBs	QSeds
$x_{50°C}$	-0.85	0.56	0.48	-0.11	-0.16
$x_{100°C}$	-0.85	0.64	0.40	-0.20	-0.18
$x_{150°C}$	-0.80	0.63	0.38	-0.37	-0.17

how much the temperature field along the plate boundary can vary without violating any of the imposed parameter constraints. This is illustrated in the right column of Figure 8, where the white segments show the possible distances from the deformation front with the 50 °C, 100 °C, and 150 °C isotherms intersecting the plate boundary, respectively. Ranges of these distances are summarized in the constraints row of Table 1. Furthermore, parameters of the models satisfying all parameter constraints and providing the best fit, the shallowest isotherms, and the deepest isotherms are listed. The temperature in the subduction thrust increases from 50 °C ∼10 km landward of the trench axis to 150 °C at ∼20 km depth ∼65 km from the deformation front. As illustrated in Figure 1 and 6, the NEIC hypocenter coincides with the 150 °C isotherm within the given uncertainties.

To study how changes in different parameters effect the modeled results, we computed the Spearman rank correlation coefficients of the relations between the model parameters and the resulting distances of intersection between the 50 °C, 100 °C, and 150 °C isotherms with the plate boundary. The Spearman rank correlation is a nonparametric rank statistic proposed by Spearman in 1904 as a measure of the strength of the associations between two variables (Lehmann and D'Abrera, 1975). It assesses how well an arbitrary monotonic function describes the relationship between two variables, without making any assumptions about the frequency distribution of the variables. It does not require the assumption that the relationship between the variables is linear, nor does it require the variables to be measured on interval scales.

The correlation coefficients were computed along with their significance using Matlab® functions implemented by Schloegl (2003). All correlation coefficients, tabulated in Table 2, are significant with a probability of at least 98%. In our model, the temperature of the upper oceanic crust has the strongest correlation with the temperature distribution on the plate boundary, followed by the thermal conductivity off the CnBs and Seds domains. While the correlation of the temperature distribution an the model parameters generally decreases with increasing distance from the deformation front, the correlation with the radiogenic heat production in the CnBs domain is increasingly pronounced.

5 Discussion and conclusions

We presented a numerical model which is capable of predicting the temperature field at the seismogenic updip limit off Nicaragua, while integrating and satisfying all imposed constraints. We are, however, aware that the relatively simple model cannot fully represent the complex processes that are effect an active subduction zone. As is common practice and mentioned earlier, we used 0 °C as a constant value for the bottom water temperature. If the temperatures in the whole model domain were increased by 2 °C to account for the present bottom water temperatures, the 150 °C isotherm would be displaced by about 1 km down slap. Due to the lack of proper constraints, we also had to neglect many other processes with possibly large impact on the thermal state. Firstly, the subduction of sediments was ignored, even thought it is known that erosion takes place in the working area (Ranero and von Huene, 2000). Furthermore, we did not assign a specific thickness to the cooled layer of the upper oceanic crust as done by Harris and Wang (2002). These effects would lower the temperatures at the décollement, while other processes like frictional heating, which is supposed to be low (Harris and Wang, 2002), would increase the temperature. However, adding any of these effects to the model without supplying good constraints would not enhance the performance of the model since all constraints are already satisfied by a whole range of simpler models.

On the other hand, the uncertainty of the model could be reduced by refining the current constraints. Our numerical experiments demonstrated that reliable surface heat flux measurements provide very useful independent constraints on the model, and the analysis of the correlation coefficients suggest that a refinements of the constraints on the initial thermal state of the subducting oceanic plate and the thermal conductivity of the continental basement have the greatest potential to decrease the uncertainties in the modeled results.

Pelayo and Wiens (1992) investigated several tsunami earthquakes world-wide, including tsunami events in the Kurile trench. It is striking that the 1992 Nicaragua event mimics major features of the October 20, 1963 and June 10, 1975 Kurile tsunami earthquakes. Most important, all three earthquakes were followed by aftershocks arcward and down-dip of the main shock. In contrast to this observation, most large interplate earthquakes show aftershocks located seaward of the epicenter, consistent with up-dip rupture propagation (Kelleher and Sykes, 1973). To explain this behavior, (Pelayo and Wiens, 1992) suggested that tsunami earthquakes generally nucleate within the typically aseismic region between the updip limit of the seismogenic zone and the trench axis, and that seaward propagation of aftershocks is inhibited by the velocity strengthening behavior of this zone. In contrast, our results suggest that tsunami earthquakes may nucleate in the uppermost region of the seismogenic zone at temperatures of $\sim$150 °C.

Faults, like the San Andreas fault, show an upper and lower cutoff of seismicity (Marone and Scholz, 1988), indicating that earthquakes only nucleate over a limited depth range in a frictionally unstable region the seismogenic zone. In subduction zones, the upper transition is defined by the seismic front. No earthquake can nucleate seaward of the seismic front as a consequence of the frictional properties of sediment in the shallow fault zone. In this zone, the plate motion is accommodated by aseismic creep. If earthquakes propagate into this zone of stable sliding, a negative stress drop will occur, resulting in a rapid stop of rupture propagation (Scholz, 1998). However, very large earthquakes, that rupture the entire seismogenic zone, can propagate dynamically through the upper stability transition zone and breach the surface (Scholz, 1998, 2002). Thus, the main shock of a tsunami earthquake may release enough energy to propagate through this (velocity strengthening) region. In addition, up-dip propagation could be exacerbated by the presence of elevated fluid pressure that promotes rapid seismic slip at very low frictional resistance (Seno, 2002). For Northeast Japan, (Tanioka et al., 1997) propose an other mechanism. Off Japan, the incoming oceanic lithosphere is highly faulted and exhibits a well-developed horst and graben structure. The same features are observed off Nicaragua (Figure 1). Though the crust is covered with sediment, horsts and seamounts may breach the sediment blanket and create contact with the hanging wall, which may promote rupture propagation. Consequently, rupture propagation is not governed by the frictional properties of the sediment, but by the frictional properties of the outcropping basement and the overriding plate. Nevertheless, only very few aftershocks are located in this region (Figure 1). This suggests that although the rupture could propagate through this area, there is no or little nucleation of events possible seaward of the seismic front. Therefore, using the classification of Scholz (1998, 2002), the region may be characterized by conditionally stable friction behavior.

The majority of large and great subduction zone earthquakes nucleate near the downdip limit of the seismogenic zone and propagate up-dip (Kelleher and Sykes, 1973). Such patterns are particularly typical for interface events from the Kuriles, Kamchatka, Aleutians and Mexico (Tichelaar and Ruff, 1993) and suggest that confining pressure and temperature have rigidified sediments at depth and caused large and strong contact zones between both plates (Moore et al., 2001). During rupture propagation, most subduction thrust earthquakes lose their energy and stop near the up-dip limit. Tsunami earthquakes, in contrast, tend to nucleate near the up-dip limit of the coupling zone, where coupling might still be laterally heterogeneous along the thrust contact. In such an environment locked asperities of consolidated and cemented sediment patches are perhaps too small to accumulate stresses required to cause a $M_s > 7$ earthquake. Other processes may therefore contribute to increase normal stress along the plate interface.

Seamount subduction or the subduction of other topographic highs and ridges profoundly affects the state of stress in the subduction thrust. A seamount forced into a subduction zone will increase the normal stress on the subduction interface and hence will enhance seismic coupling (Scholz and Small, 1997). Seamounts are indeed abundant on the incoming Cocos plate offshore Nicaragua (Figure 1). We conclude that in addition to temperature-dependent induration of sediments, increased normal stress by seamount subduction may contribute to accumulate stress sufficient enough to support a $M_s > 7$ earthquake near the up-dip limit of the seismogenic zone. The resulting energy release may promote dynamic up-dip rupture propagation through the generally aseismic region seaward of the seismic front.

Acknowledgements

We are grateful to scientists, master, and crew of RV Meteor cruise M54-2 for having provided support, information and discussion. Special thanks to Norbert Kaul and Bernd Heesemann for assistance during the heat flow deployments. This study was funded by the Deutsche Forschungsgemeinschaft through grant Vi 133/7-1 to University of Bremen and the SFB 574 Volatiles and fluids in subduction zones at Christan-Albrechts University, Kiel.

References

Baptisa, A., Priest, G., Murty, T., 1993. Field survey of the 1992 Nicaragua tsunami. Mar. Geodesy 16, 169–203.

Barckhausen, U., Ranero, C. R., von Huene, R., Cande, S. C., Roeser, H. A., 2001. Revised tectonic boundaries in the Cocos Plate off Costa Rica: Implications for the segmentation of the convergent margin and for plate tectonic models. J. Geophys. Res. 106, 19207–19220.

Bilek, S. L., Lay, T., Jul. 2002. Tsunami earthquakes possibly widespread manifestations of frictional conditional stability. Geophys. Res. Lett. 29, 18–1.

Bookman, C. A., Malone, I., Langseth, M. G., 1972. Sea floor geothermal measurements from conrad cruise 13. Tech. Rept. 5-CU-5-72, Columbia University, in global heat-fux compilation by Pollack 1991.

Buecker, C., Rybach, R., 1996. A simple method to determine heat production from gamma-ray logs. Mar. Petrol. Geol. 13, 373–375.

Byrne, D. E., Davis, D. M., Sykes, L. R., 1988. Loci and maximum size of thrust earthquakes and the mechanics of the shallow region of subduction zones. Tectonics 7, 833–857.

Casciola, G., Romani, L., 2004. A generalized conversion matrix between non-

uniform b-spline and bezier representations with applications in CAGD. In: Multivariate Approximation: Theory and Applications.
URL http://amsacta.cib.unibo.it/archive/00000853/

Chipperfield, A., Fleming, P. J., Pohlheim, H., Fonseca, C. M., 1994. Genetic algorithm toolbox for use with matlab. Tech. Rep. 512, Department of Automatic Control and Systems Engineering, University of Sheffield, version 1.2.
URL http://www.shef.ac.uk/acse/research/ecrg/gat.html

Christensen, D. H., Ruff, L. J., Aug. 1983. Outer-rise earthquakes and seismic coupling. Geophysical Research Letters 10, 697–700.

Comsol, 2005. Comsol Modeling Guide. 3rd Edition.

DeMets, C., 2001. A new estimate for present-day cocos-caribbean plate motion: Implications for slip along the central american volcanic arc. Geophys. Res. Lett. 28 (21), 4043–4046.

Divins, D. L., 2005. NGDC total sediment thickness of the world's oceans & marginal seas. Tech. rep., NGDC.
URL http://www.ngdc.noaa.gov/mgg/sedthick/sedthick.html

Geist, E. L., May 2002. Complex earthquake rupture and local tsunamis. Journal of Geophysical Research (Solid Earth) 107, 2–1.

Geist, E. L., Bilek, S. L., 2001. Effect of depth-dependent shear modulus on tsunami generation along subduction zones. Geophys. Res. Lett. 28 (7), 1315–1318.

Geist, E. L., Bilek, S. L., Arcas, D., Titov, V. V., 2006. Differences in tsunami generation between the december 26, 2004 and march 28, 2005 sumatra earthquakes. Earth Planets Space 58 (2), 185–193.
URL http://www.terrapub.co.jp/journals/EPS/abstract/5802/58020185.html

Grevemeyer, I., Diaz-Naveas, J. L., Ranero, C. R., Villinger, H. W., Aug. 2003. Heat flow over the descending nazca plate in central chile, 32[deg]s to 41[deg]s: observations from odp leg 202 and the occurrence of natural gas hydrates. Earth and Planetary Science Letters 213 (3-4), 285–298.
URL http://www.sciencedirect.com/science/article/B6V61-4983W07-3/2/f976b9fa60437b3976abe1eae5e8ae20

Grevemeyer, I., Kaul, N., Diaz-Naveas, J. L., Villinger, H. W., Ranero, C. R., Reichert, C., Jul. 2005. Heat flow and bending-related faulting at subduction trenches: Case studies offshore of nicaragua and central chile. Earth and Planetary Science Letters 236 (1-2), 238–248.
URL http://www.sciencedirect.com/science/article/B6V61-4GHRC6N-2/2/9786953d05ca4beb29b1886434d16c28

Grevemeyer, I., Villinger, H., 2001. Gas hydrate stability and the assessment of heat flow through continental margins. Geophysical Journal International 145 (3), 647–660.
URL http://www.blackwell-synergy.com/doi/abs/10.1046/j.0956-540x.2001.01404.x

Harris, R. N., Wang, K., Nov. 2002. Thermal models of the Middle America

Trench at the Nicoya Peninsula, Costa Rica. Geophys. Res. Lett. 29, 6–1.

Hartmann, A., Villinger, H., 2002. Inversion of marine heat flow measurements by expansion of the temperature decay function. Geophysical Journal International 148 (3), 628–636.
URL http://www.blackwell-synergy.com/doi/abs/10.1046/j.1365-246X.2002.01600.x

Hyndman, R. D., Davis, E. E., Wright, J. A., Dec. 1979. The measurement of marine geothermal heat flow by a multipenetration probe with digital acoustic telemetry and insitu thermal conductivity. Marine Geophysical Researches V4 (2), 181–205.
URL http://dx.doi.org/10.1007/BF00286404

Hyndman, R. D., Wang, K., Feb. 1993. Thermal constraints on the zone of major thrust earthquake failure - the cascadia subduction zone. J. Geopyhs. Res. 98, 2039–2060.

Ide, S., Imamura, F., Yoshida, Y., Abe, K., 1993. Source characteristics of the Nicaraguan tsunami earthquake of September 2, 1992. Geophys. Res. Lett. 20, 863–866.

Ihmle, P. F., 1996a. Frequency-dependent relocation of the 1992 nicaragua slow earthquake: an empirical green's function approach. Geophysical Journal International 127 (1), 75–85.
URL http://www.blackwell-synergy.com/doi/abs/10.1111/j.1365-246X.1996.tb01536.x

Ihmle, P. F., 1996b. Monte Carlo slip inversion in the frequency domain: Application to the 1992 Nicaragua slow earthquake. Geophys. Res. Lett. 23, 913–916.

Kanamori, H., 1972. Mechanism of tsunami earthquakes. Physics of the Earth and Planetary Interiors 6, 346–359.

Kanamori, H., Kikuchi, M., Feb. 1993. The 1992 nicaragua earthquake: a slow tsunami earthquake associated with subducted sediments. Nature 361 (6414), 714–716.
URL http://dx.doi.org/10.1038/361714a0

Kelleher, J. L., Sykes, J. O., 1973. Possible criteria for predicting earthquake locations and their applications to major plate boundaries of the pacific and caribbean. J. Geophys. Res. 78, 2547–22585.

Kimura, G., Silver, E., Blum, P., Shipboard Scientific Party, 1997. Init. repts. In: Proc. ODP. Vol. 170. College Station, TX (Ocean Drilling Program).

Langseth, M. G., Malone, I., Berger, D., 1971. Sea floor geothermal measurements from vema cruise 24. Tech. Rept. 3-CU-3-71, Columbia University, in global heat-fux compilation by Pollack 1991.

Langseth, M. G., Silver, E. A., 1996. The Nicoya convergent margin-a region of exceptionally low heat flow. Geophys. Res. Lett. 23 (8), 891–894.

Lehmann, E. L., D'Abrera, H. J. M., 1975. Nonparametrics : statistical methods based on ranks.

Marone, C., Scholz, C. H., Jun. 1988. The depth of seismic faulting and the upper transition from stable to unstable slip regimes. Geophysical Research

Letters 15, 621–624.

Mayer, L., Pisias, N., Janecek, T., Shipboard Scientific Party, 1992. Init. repts. In: Proc. ODP. No. 138. College Station, TX (Ocean Drilling Program).

Moore, G. F., Taira, A., Klaus, A., Shipboard Scientific Party, 2001. Init. repts. In: Proc. ODP. Vol. 190 [Online]. Available from World Wide Web:http://www-odp.tamu.edu/publications/190_IR/190ir.htm.

Morris, J. D., Villinger, H. W., Klaus, A., Shipboard Scientific Party, 2003. Init. repts. In: Proc. ODP. Vol. 205 [Online]. Available from World Wide Web:http://www-odp.tamu.edu/publications/205_IR/205ir.htm.

Newman, A. V., Schwartz, S. Y., Gonzalez, V., DeShon, H. R., Protti, J. M., Dorman, L. M., Oct. 2002. Along-strike variability in the seismogenic zone below nicoya peninsula, costa rica. Geophys. Res. Lett. 29, 38–1.

NGDC, 2005. Global digital elevation model (ETOPO2). National Geophysical Data Center.

Nielsen, H. B., 2005. immoptibox: A Matlab toolbox for optimization and data fitting. Informatics and Mathematical Modelling, Technical University of Denmark.
URL `http://www2.imm.dtu.dk/~hbn/immoptibox/`

Pelayo, A. M., Wiens, D. A., 1992. Tsunami earthquakes - Slow thrust-faulting events in the accretionary wedge. Journal of Geophysical Research 97 (B11), 1532115337.

Pfender, M., Villinger, H., 2002. Miniaturized data loggers for deep sea sediment temperature gradient measurements. Mar. Geol. 186, 557–570.

Polet, J., Kanamori, H., 2000. Shallow subduction zone earthquakes and their tsunamigenic potential. Geophysical Journal International 142, 684–702.

Pollack, H. N., Hurter, S. J., Johnston, J. R., 1992. Global heat flow data set. Tech. rep., World Data Center A for Solid Earth Geophysics, NOAA E/GCI, 325 Broadway, Boulder, CO 80303, USA.

Pribnow, D., Kinoshita, M., Stein, C., 2000. Thermal data collection and heat flow recalculations for ODP Legs 101-180. Tech. rep., Institute for Joint Geoscientific Research, Institute for Joint Geoscientific Research, GGA, Hannover, Germany, 0120432.
URL `http://www-odp.tamu.edu/publications/heatflow/`

Ranero, C. R., von Huene, R., 2000. Subduction erosion along the Middle America convergent margin. Nature 404, 748–752.

Ranero, C. R., von Huene, R., Flueh, E., Duarte, M., Baca, D., McIntosh, K., 2000. A cross section of the convergent Pacific margin of Nicaragua. Tectonics 19, 335–357.

Satake, K., 1994. Mechanics of the 1992 Nicaragua tsunami earthquake. Geophys. Res. Lett. 21, 2519–2522.

Satake, K., Abe, K., Abe, K., Bourgeois, J., Estrada, F., Iio, Y., Imamura, F., Katao, H., Noguera, E., Tsuji, Y., 1993. Tsunami field survey of the 1992 nicaragua earthquake. EOS Transactions 74, 145–145.

Satake, K., Tanioka, Y., May 1999. Sources of tsunami and tsunamigenic earthquakes in subduction zones. Pure and Applied Geophysics V154 (3),

467–483.
URL http://dx.doi.org/10.1007/s000240050240

Schloegl, A., October 2003. The NaN-toolbox: A statistic-toolbox for Octave and Matlab. Version 1.52.
URL http://www.dpmi.tu-graz.ac.at/~schloegl/matlab/NaN/

Scholz, C. H., Jan. 1998. Earthquakes and friction laws. Nature 391 (6662), 37–42.
URL http://dx.doi.org/10.1038/34097

Scholz, C. H., 2002. The mechanics of earthquakes and faulting. Cambridge [u.a.]: Cambridge Univ. Press, 2002.

Scholz, C. H., Small, C., Jun. 1997. The effect of seamount subduction on seismic coupling. Geology 25 (6), 487–490.
URL http://dx.doi.org/10.1130/0091-7613(1997)025<0487:TEOSSO>2.3.CO;2

Sclater, J. G., G., R. U., Dixon, F. S., 1970. Heat flow in the southwestern pacific. J. Geophys. Res. 75, 333–348, in global heat-fux compilation by Pollack 1991.

Seno, T., 2002. Tsunami earthquakes as transient phenomena. Geophys. Res. Lett. 29 (10), 1419.

Stein, C. A., Stein, S., Sep. 1992. A model for the global variation in oceanic depth and heat flow with lithospheric age. Nature 359 (6391), 123–129.
URL http://dx.doi.org/10.1038/359123a0

Tanioka, Y., Ruff, L., Satake, K., 1997. What controls the lateral variation of large earthquake occurrence along the japan trench. The Island Arc 6, 261–266.

Tichelaar, B. W., Ruff, L. J., Feb. 1993. Depth of seismic coupling along subduction zones. Journal of Geophysical Research 98, 2017–2037.

UNAVCO, 2006. Plate motion calculator.
URL http://sps.unavco.org/crustal_motion/dxdt/model/

Vaquier, V., Sclater, J. G., Corry, C. E., 1967. Studies of the thermal state of the earth, the 21st paper - heat flow, eastern pacific. Bull. Earthq. Res. Inst. Tokyo Univ. 45, 375–393, in global heat-fux compilation by Pollack 1991.

Velasco, A. A., Ammon, C. J., Lay, T., Zhang, J., 1994. Imaging a slow bilateral rupture with broadband seismic waves: The September 2, 1992 Nicaraguan tsunami earthquake. Geophys. Res. Lett. 21, 2629–2632.

von Herzen, R., Maxwell, M. E., 1959. The measurement of thermal conductivity of deep sea sediments by a needle probe method. J. Geophys. Res. 64, 1557 1563.

Walther, C. H. E., Flueh, E. R., Ranero, C. R., von Huene, R., Strauch, W., Jun. 2000. Crustal structure across the pacific margin of nicaragua:evidence for ophiolitic basement and a shallow mantle sliver. Geophysical Journal International 141, 759–777.

Whitley, D., 1994. A genetic algorithm tutorial. Statistics and Computing 4, 65–85.

URL http://samizdat.mines.edu/ga_tutorial/
Wilson, D., Teagle, D., Acton, G., Shipboard Scientific Party, 2003. Init. repts. In: Proc. ODP. No. 206. College Station, TX (Ocean Drilling Program).

A Supplementary material

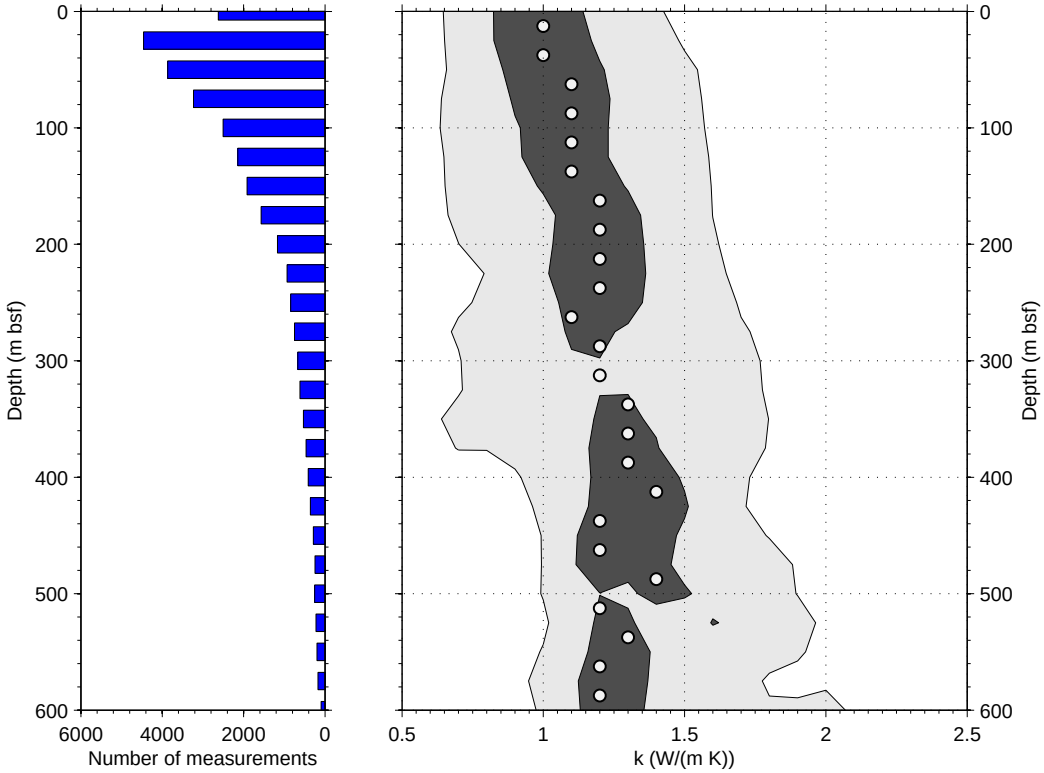

Fig. A.1. Distribution off thermal conductivities measured during ODP Legs 101-180 which were compiled by Pribnow et al. (2000). Data were first binned into depth intervals of 25 m (left) and consecutively into thermal conductivity intervals of 0.1 W/(m K). Based on the resulting matrix of binned data, a normalized frequency distribution of thermal conductivity measurements was computed (right). Assuming a Gaussian distribution of the measurements per depth interval, the shaded contour intervals (0.242 light gray, and 0.054 dark gray) highlight the areas which contain 68%, and 95% of the measurements in the given depth interval, respectively. Circles mark the bins containing most thermal conductivity measurements per depth interval.

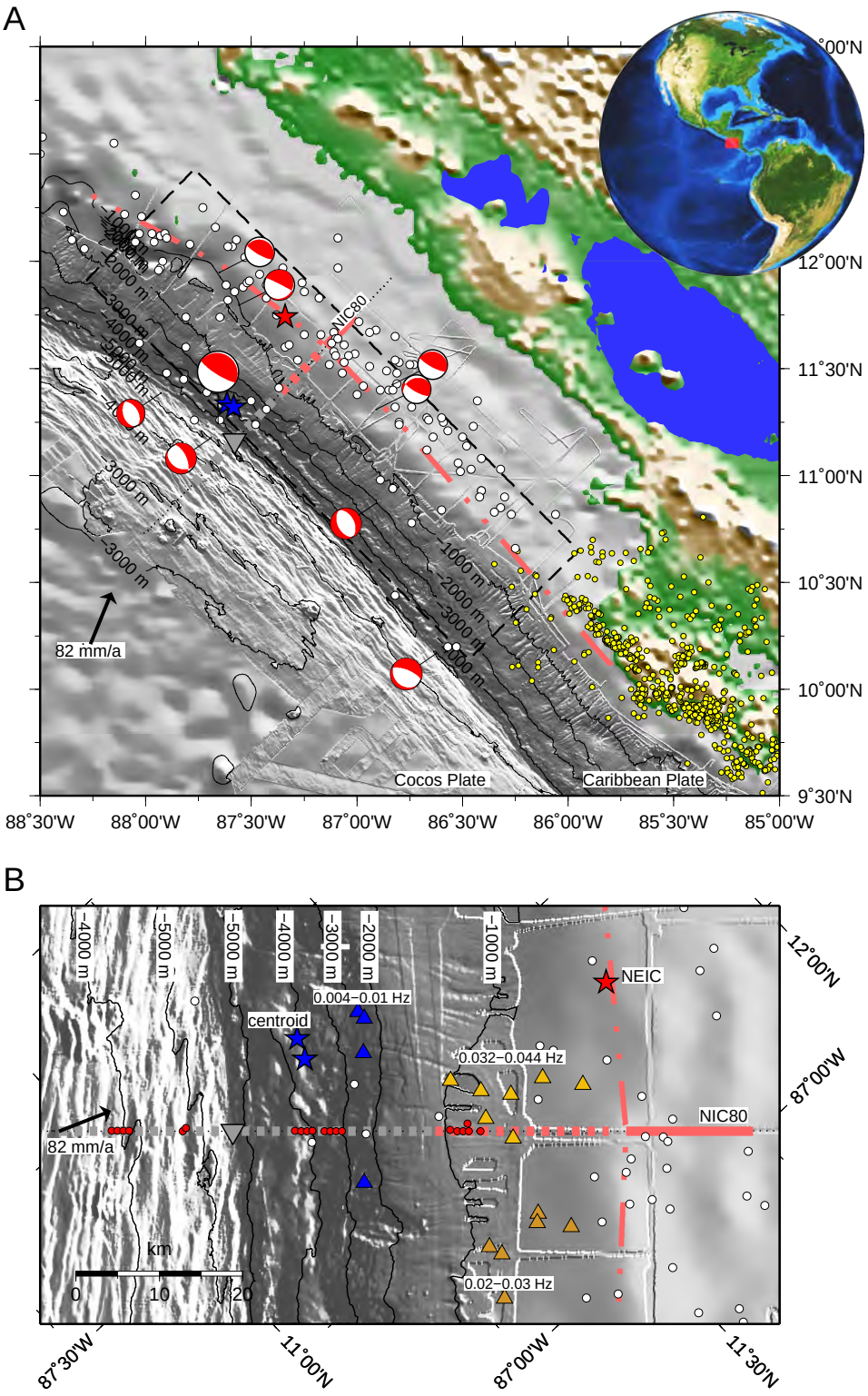

Fig. A.2. See Fig.1

C.2 Alteration of the subducting oceanic lithosphere at the southern central Chile trench-outer rise

Artikel in Geochemistry, Geophysics, Geosystems veröffentlicht (*Contreras-Reyes et al.*, 2007).

Alteration of the subducting oceanic lithosphere at the southern central Chile trench–outer rise

Eduardo Contreras-Reyes, Ingo Grevemeyer, Ernst R. Flueh, and Martin Scherwath
Leibniz-Institute of Marine Sciences (IFM-GEOMAR), Wischhofstrasse 1-3, D-24148 Kiel, Germany (econtreras-reyes@ifm-geomar.de; igrevemeyer@ifm-geomar.de; eflueh@ifm-geomar.de; mscherwath@ifm-geomar.de)

Martin Heesemann
Department of Earth Sciences, University of Bremen, Postfach 330440, D-28334 Bremen, Germany (heesema@uni-bremen.de)

[1] Hydrothermal circulation and brittle faulting processes affecting the oceanic lithosphere are usually confined to the upper crust for oceanic lithosphere created at intermediate to fast spreading rates. Lower crust and mantle rocks are therefore relatively dry and undeformed. However, recent studies at subduction zones suggest that hydration of the oceanic plate is most vigorous at the trench–outer rise, where extensional bending-related faulting affects the hydrogeology of the oceanic crust and mantle. To understand the degree of hydration, we studied the seismic velocity structure of the incoming Nazca plate offshore of southern central Chile (~43°S); here the deep-sea trench is heavily filled with up to 2 km of sediments. Seismic refraction and wide-angle data, complemented by seismic reflection imaging of sediments, are used to derive a two-dimensional velocity model using joint refraction and reflection traveltime tomography. The seismic profile runs perpendicular to the spreading ridge and trench axes. The velocity model derived from the tomography inversion consists of a ~5.3-km-thick oceanic crust and shows P wave velocities typical for mature fast spreading crust in the seaward section of the profile, with uppermost mantle velocities as fast as ~8.3 km/s. Approaching the Chile trench, seismic velocities are significantly reduced, however, suggesting that the structures of both the oceanic crust and uppermost mantle have been altered, possibly due to a certain degree of fracturing and hydration. The decrease of the velocities roughly starts at the outer rise, ~120 km from the deformation front, and continues into the trench. Even though the trench is filled with sediment, basement outcrops in the outer rise frequently pierce the sedimentary blanket. Anomalously low heat flow values near outcropping basement highs indicate an efficient inflow of cold seawater into the oceanic crust. Hydration and crustal cracks activated by extensional bending-related faulting are suggested to govern the reduced velocities in the vicinity of the trench. Considering typical flow distances of 50 km, water might be redistributed over most of the trench–outer rise area. Where trapped in faults, seawater may migrate down to mantle depth, causing up to ~9% of serpentinization in at least the uppermost ~2 km of the mantle between the outer rise and the trench axis.

Components: 10,027 words, 9 figures.

Keywords: trench–outer rise; bending-related faulting; seismic tomography.

Index Terms: 8170 Tectonophysics: Subduction zone processes (1031, 3060, 3613, 8413); 8150 Tectonophysics: Plate boundary: general (3040); 7220 Seismology: Oceanic crust.

Received 15 March 2007; **Accepted** 4 May 2007; **Published** 7 July 2007.

Contreras-Reyes, E., I. Grevemeyer, E. R. Flueh, M. Scherwath, and M. Heesemann (2007), Alteration of the subducting oceanic lithosphere at the southern central Chile trench–outer rise, *Geochem. Geophys. Geosyst.*, *8*, Q07003, doi:10.1029/2007GC001632.

1. Introduction

[2] Oceanic lithosphere created at moderate to fast spreading mid-ocean ridges is characterized by a ridge-parallel fault pattern. Pervasive fracturing and hydrothermal activity, however, are largely confined to crustal levels [e.g., *Carbotte and Scheirer*, 2004; *Karson*, 1998]. As the crust ages, cracks and pore spaces inherently related to the formation of crust are clogged by precipitation of secondary hydrothermal alteration products in the extrusive lava pile [e.g., *Alt et al.*, 1986; *Wilkens et al.*, 1991; *Grevemeyer and Bartetzko*, 2004]. Global compilations of seismic refraction velocities for the uppermost oceanic crust [*Grevemeyer and Weigel*, 1996; *Carlson*, 1998] and dedicated seismic refraction experiments [e.g., *Grevemeyer and Weigel*, 1997; *Grevemeyer et al.*, 1999] have established an empirical relationship between lithospheric age and seismic velocity. The global trend suggests that uppermost P wave velocities of layer 2 increase rapidly close to the spreading axis and within ~8 Ma reach values of mature oceanic crust (>4.5 km/s) [*Carlson*, 1998; *Grevemeyer and Bartetzko*, 2004]. Within this context, we will refer to "normal" mature oceanic lithosphere typical of fast spreading structures if (1) hydration is confined to the permeable upper lava pile, (2) the ridge flank hydrothermal circulation system has largely ceased, and (3) the oceanic lithosphere is positioned away from anomalous regions such as fracture zones and hot spots regions [e.g., *White et al.*, 1992].

[3] Growing observational evidence in subduction zones suggest that this condition of "normal" and "unaltered" ocean lithosphere can be dramatically perturbed at the outer rise seaward of deep-sea trenches [e.g., *Peacock*, 2004; *Ranero et al.*, 2003]. The outer rise is formed when the ocean lithosphere approaches a subduction zone and bends into the trench, thus producing a prominent outer bulge seaward of the trench axis. Here, outer rise earthquakes are linked to bending-related normal faulting [*Chapple and Forsyth*, 1979] and possibly rupture the oceanic mantle [e.g., *Kanamori*, 1971; *Christensen and Ruff*, 1983], creating a pervasive tectonic fabric that may cut across the crust, penetrating deep into the uppermost mantle [e.g., *Peacock*, 2001; *Ranero et al.*, 2003]. Moreover, new crustal cracks and fissures are caused by bending-related faulting seaward of the trench axis, modifying the structure of the crust. Therefore bending-related faulting plays a crucial role for the alteration of oceanic lithosphere; it affects the porosity and permeability structure of the entire oceanic crust and consequently generates pathways for fluids down to mantle depth.

[4] One key factor controlling the local hydrogeological regime of the oceanic lithosphere is the thickness of the sedimentary blanket. Convergent margins such as Central America and north Chile are poorly sedimented, and seawater can easily enter the igneous oceanic crust where the permeable basement rocks are widely exposed (e.g., surface-cutting tectonic faults or outcropping basement highs). These subduction zones have been suggested to be characterized by a high degree of hydration at the outer rise [*Ranero et al.*, 2003; *Ranero and Sallares*, 2004; *Grevemeyer et al.*, 2005, 2007]. In contrast, in well sedimented margins (Cascadia and southern central Chile), a thick sedimentary cover is believed to hinder interaction between the ocean and the basement. Therefore the degree of hydration is expected to be lower than in poorly sedimented trenches, although mechanisms by which fluids may bypass thick sediments remain still under debate. In general, the hydrothermal activity in the oceanic crust is controlled by faulting and the presence of outcropping basement highs. Heat flow data suggest that hydrothermal circulation is more vigorous at trenches where bending-related normal faults breach the seafloor and thus facilitate fluid flow into the crust [*Grevemeyer et al.*, 2005]. Outcropping basement also play a crucial role, since it may act as transmissive pathway for fluids and heat in areas where the surrounding basement is blanketed by sediments, as it has been evidenced by anomalous low heat flow values near seamounts, indicating an efficient inflow of cold seawater into the oceanic crust [*Villinger et al.*, 2002; *Fisher et al.*, 2003a, 2003b]. Isolated basement outcrops penetrating through thick sediments might guide hydrothermal circulation between sites separated by large distances [*Fisher et al.*, 2003a]. Once cold seawater

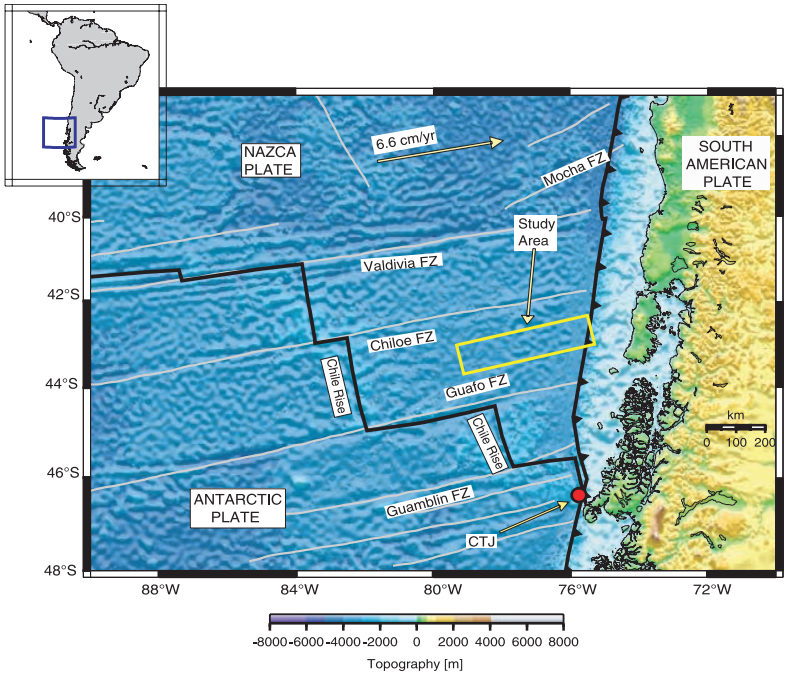

Figure 1. Geodynamic setting of Nazca, Antarctic, and South American plates. These plates join at the Chile Triple Junction (CTJ), where the Chile Rise is currently subducting at ~46.5°S. The oceanic Nazca plate is segmented by several fracture zones (FZs), resulting in a strong variability of the age of the subducting plate. The study area is located between two Fracture Zones, Chiloe FZ and Guafo FZ, and its plate age ranges from 18.5 to 10 Ma along the Chile trench.

is infiltrated and bounded in the upper oceanic crust, tectonic faulting may allow fluids trapped within crustal pores spaces to enter the lower crust and perhaps even the upper mantle [e.g., *Grevemeyer et al.*, 2005].

[5] To better understand the transition from "normal" and "dry" to deformed and hydrated subducting lithosphere and its degree of hydration in the trench–outer rise area, we studied the velocity structure of the incoming oceanic Nazca plate offshore of south central Chile. Seismic wide-angle reflection and refraction data are used to derive an accurate 2-D tomography velocity model of a ~250 km long seismic profile located oceanward from the Chile trench axis. We present new geophysical evidence documenting changes in the seismic structure of the incoming oceanic plate from the outer rise to just before its subduction in the deep-sea trench. A nonlinear Monte Carlo uncertainty analysis is performed to estimate a posteriori model variance of the tomography velocity model. In addition, heat flow data recorded at the outer rise are used to study the distribution of temperature along the sediment/crust boundary. The data were acquired during the R/V *Sonne* cruise SO181 as part of the TIPTEQ (from The Incoming Plate to Mega-thrust EarthQuake processes) project [*Flueh and Grevemeyer*, 2005].

2. Tectonic Setting

[6] Along the south central Chile trench the southern Nazca plate subducts at a relatively high convergence rate of ~6.6 cm/yr beneath the South American plate, with a convergence azimuth of ~78°E [*Angermann et al.*, 1999] (Figure 1). The southern Nazca plate has been formed at the Chile Rise (a fast mid-ocean spreading ridge). Fracture zones (FZs) cut the Chile Rise into several segments (Figure 1), resulting in abrupt changes of thermal states along the plate boundary. The spreading center segments bounded by these fracture zones are roughly parallel to the trench strike (Figure 1). At ~46.5°S the Chile Rise is currently subducting, defining the Chile Triple Junction (CTJ) of the subducting Nazca and Antarctic plates, and the continental South American plate. North of the CTJ occur a series of age jumps across several fracture zones, from 0 Myr up to 18.5 Myr at the Valdivia FZ (Figure 1). The south central Chile trench is filled by terrigenous sediments sourced from the Andes [*Thornburg and Kulm*,

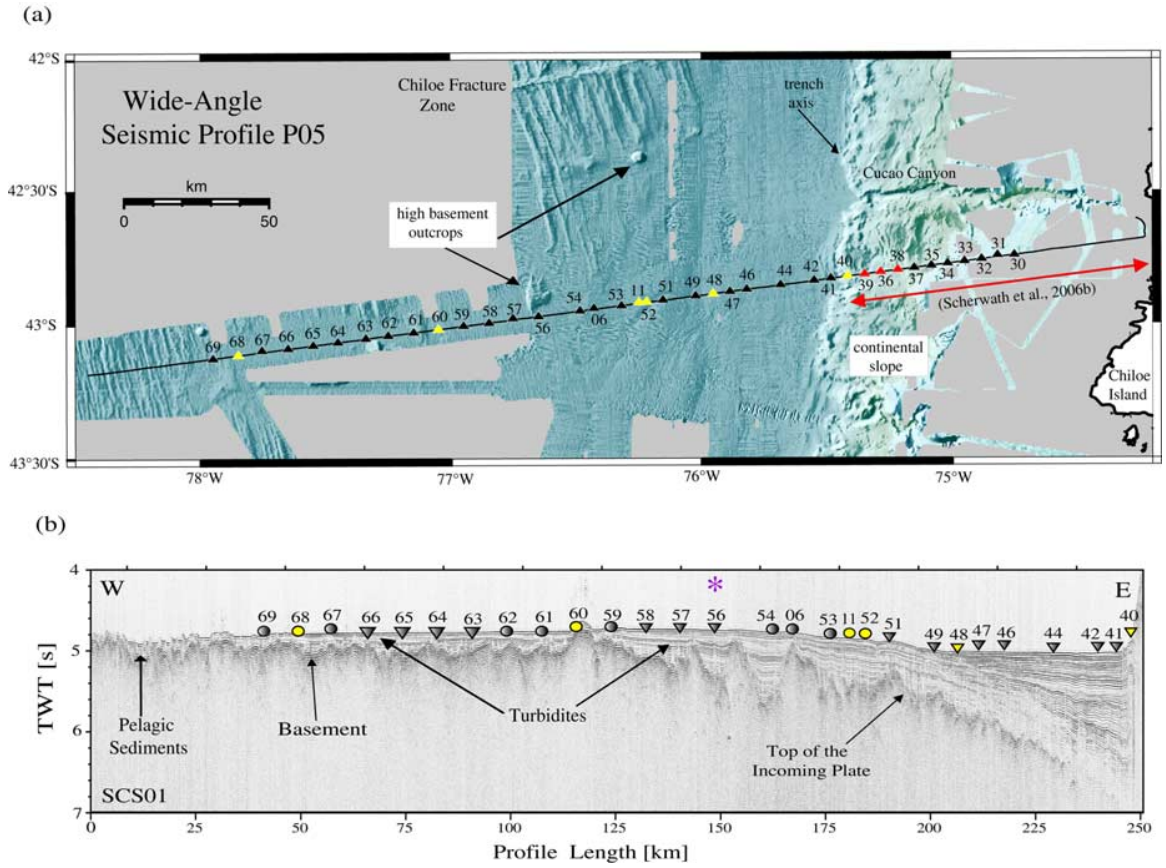

Figure 2. (a) High-resolution bathymetric image and wide-angle seismic profile P05. The seismic line begins ~280 km from the Chile Rise (see Figure 1), and it extends up to the deep-sea trench and part of the continental slope. Yellow triangles indicate the six stations of which data examples are shown in Figures 3 and 8. Red dots indicate the three stations positioned on the continental slope [*Scherwath et al.*, 2006b], which are included in our tomographic model. (b) High-resolution seismic line SCS01 coincident with wide-angle seismic profile P05. Locations of OBH are shown by solid circles, and locations of OBS are shown by solid triangles. Location of the high basement outcrop is denoted by asterisk. Some tensional normal faults are reflected by offsets in the trench–outer rise region.

1987]. Sediment within the trench are redistributed from south to the north [*Thornburg et al.*, 1990], which is explained by the slight northward dip of the trench floor [e.g., *Thornburg et al.*, 1990]. Trench fans (33–41°S) are built at the mouths of major submarine canyons and channels which act as point sources of sediment supply [*Thornburg and Kulm*, 1987]. South of 41°S, sheet turbidites extend across the entire width of the trench [*Thornburg and Kulm*, 1987].

[7] The westward terminus of the seismic wide-angle profile studied here is located approximately 280 km eastward of the Chile Rise on 9 Myr old crust [*Tebbens et al.*, 1997], the line orientation being parallel to the plate motion vector (Figure 1). The profile is located between Chiloe and Guafo FZs (Figure 1), where the plate age decrease from 18.5 to 10 Myr along the Chile trench, and the half-spreading rate ranges between 45 and 35 mm/yr [*Tebbens et al.*, 1997]. The trench basin is broad, owing to the large extension of turbidite deposits seaward [*Voelker et al.*, 2006]. Further to the west, the Nazca plate is covered by a few hundred meters of hemipilagic and pelagic sediments, whereas toward the trench, the sedimentary cover becomes thicker due to the turbiditic deposits filling the trench with a total thickness of ~2 km [*Scherwath et al.*, 2006a]. The continental slope is steep and is characterized by the presence of the submarine Cucao Canyon (Figure 2a), while the continental shelf is broad and probably trapped large volume of Pliocene sediments [*Reichert et al.*, 2002].

3. Seismic Data

[8] From December 2004 to February 2005, the TIPTEQ project investigated the subduction zone

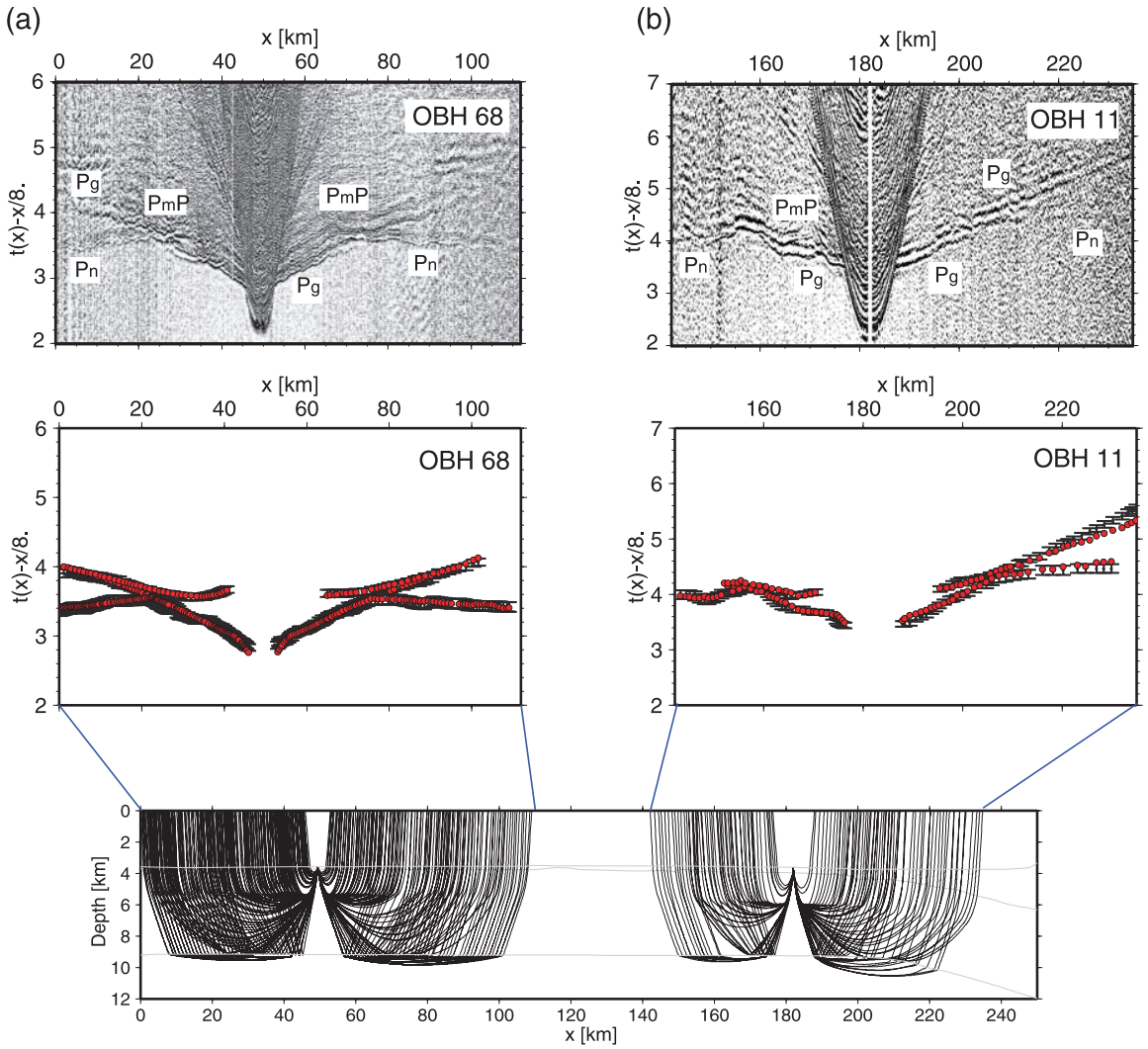

Figure 3. Examples of wide-angle seismic data with picked (solid circle with pick error) and predicted (red circles) traveltimes. Calculated traveltimes are based on the velocity model presented in Figure 7a, and corresponding raypaths are also plotted at the bottom. (a) OBH 68, (b) OBH 11, (c) OBH 60, (d) OBH 48, and (e) OBH 40.

offshore south-central Chile between 35° and 48°S aboard of the German R/V *Sonne*. During the cruise seismic wide-angle reflection and refraction data, high-resolution seismic reflection data, multibeam bathymetry, heat flow, and seismological data were acquired in this region [*Flueh and Grevemeyer*, 2005; *Scherwath et al.*, 2006a] to study the physical properties of the incoming Nazca plate and its impact on seismogenesis, offshore of the rupture area of the 1960 Chile megathrust earthquake. In this paper, we present seismic wide-angle data that were collected along the profile P05 located seaward of the trench axis on the oceanic Nazca plate, supplemented by high-resolution swath bathymetric images of the surrounding seafloor (Figure 2a). Shots were recorded with 38 OBS (Ocean Bottom Seismometers) [*Bialas and Flueh*, 1999] and OBH (Ocean Bottom Hydrophones) [*Flueh and Bialas*, 1996] spaced at a distance of ∼5.5 km. Coincident seismic reflection data were also collected along this profile (Figure 2b). For the reflection investigation a 100-m-long 16-channel streamer and a Generator/Injector (GI) gun with a volume of 1.5 liters were used, providing high-resolution images of the sedimentary sequences blanketing the incoming plate. From the 38 seismic ocean bottom stations, 28 were deployed on the oceanic plate and the rest

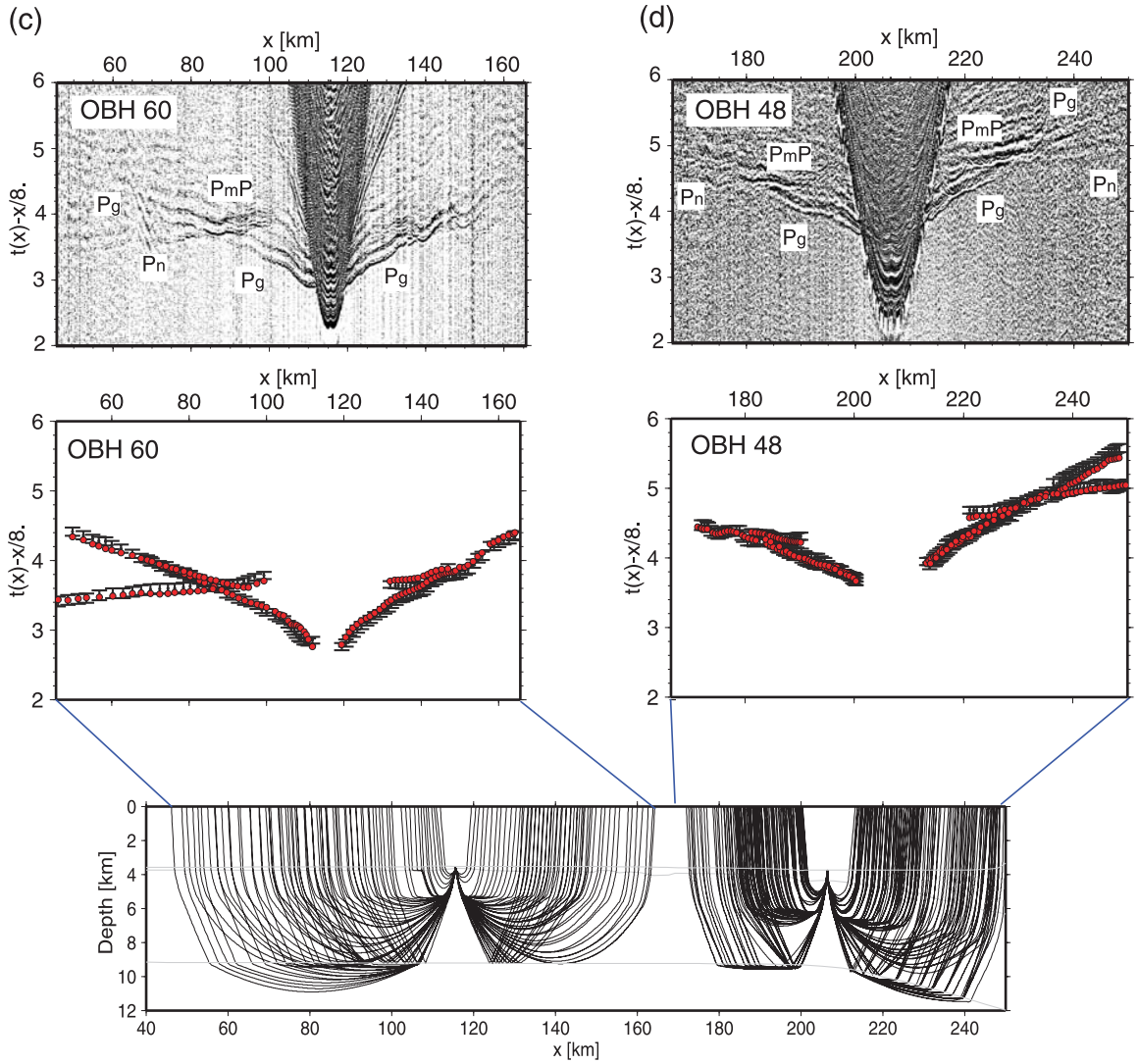

Figure 3. (continued)

along the continental slope. In order to study the seismic structure of the oceanic Nazca plate, we used the OBH/S deployed seaward of the trench. Three stations on the continental slope were also included in the inversion approach to constrain the velocity structure and Moho depth below the trench (see Figure 2a).

[9] The seismic source for the refraction work was a cluster of 8x8-liters G-guns, providing a total volume of 64 liters for each shot. This source was fired at a time interval of 60 s, which corresponds to an average shot spacing of ~150 m. The record sections were interpreted after bandpass filtering and predictive deconvolution. The signal-to-noise ratio obtained for most of the stations is high (Figure 3). Crustal refractions (P_g), Moho reflections (P_mP) and upper mantle refractions (P_n) were recorded on almost all stations with excellent quality. Five examples of seismic record sections are shown in Figure 3, with their respective seismic phases identified. Apparent velocities, which are influenced by the trench-sediment, decrease toward the trench. Refractions through trench-sediment (P_s), and reflections from the top of the igneous crust (P_bP) start to appear at approximately profile-km 200 and hence 50 km from the trench axis. Figure 3e shows P_s and P_bP of good quality at OBH 40 at the trench. Those traveltimes complement the high-resolution seismic reflection data

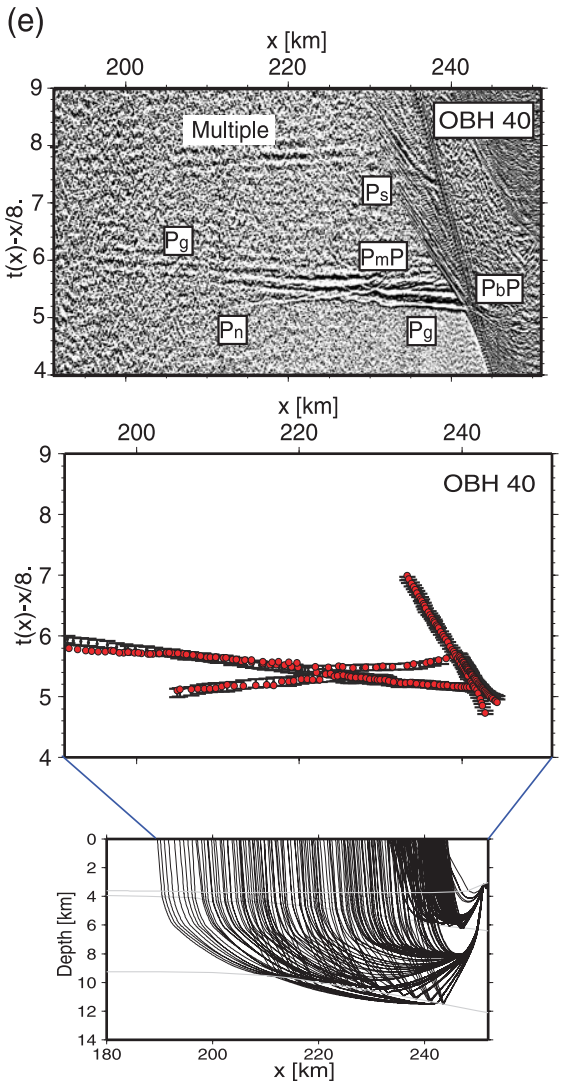

Figure 3. (continued)

(Figure 2b) and are used to constrain the sedimentary section in this part of the model.

[10] Picking of the seismic phases was done manually, and picking errors were assigned on the basis of the dominant period of the phase. A total of 5048 first arrivals (P_g and P_n), and 1721 Moho reflections (P_mP) were picked from 31 record sections. For the sedimentary section only stations located to the east of x = 200 km were utilized, because clear P_s and P_bP phases are confined to the trench basin. A total of 1456 P_s and 654 P_bP were picked from these stations. Typically, errors were assumed to be half a period of one arrival, to account for a possible systematic shift in the arrival identification, and were weighted according to the phase quality. Average picking uncertainties are ~50 ms at near offsets and ~70 ms at far offsets for refracted arrivals, and ~50 ms and ~70 ms for P_bP and P_mP phases, respectively.

4. Traveltime Tomography Scheme

[11] The velocity-depth model was derived using the joint refraction and reflection traveltime inversion method of *Korenaga et al.* [2000]. This method allows simultaneous refraction and reflection traveltimes inversion for a 2-D velocity field that is parameterized as a sheared mesh hanging beneath the seafloor and where node spacings can vary laterally and vertically. The floating reflector is represented as an array of linear segments whose nodal spacing is independent of that used in the velocity grid and it has just one degree of freedom (vertical direction). Traveltimes and raypaths are calculated by utilizing a hybrid ray-tracing scheme based on the graph method and local ray-bending refinement [*van Avendonk et al.*, 1998]. Smoothing constraints using predefined correlation lengths (average-smoothness window) and optimized damping constraints for the model parameters are employed to regularize an iterative linearized inversion [*Korenaga et al.*, 2000]. We use a hybrid approach of multistep tomography using four layers, (1) water, (2) sedimentary section, (3) oceanic crust, and (4) upper mantle. To derive the velocity depth model, the water depths were taken from the multibeam bathymetry, which remained fixed during the inversion. The vertical incidence reflection data, sediment refracted P_s and reflected P_bP phases were used to invert for the velocities and thickness of the sedimentary trench fill and hence the geometry of the top of the downgoing plate. Sedimentary velocities and basement depth were then held fixed in the following iterative inversions. The oceanic crust was inverted using P_g and P_mP phases in order to derive the velocity field and Moho depth, and similarly, the crustal velocities and Moho depth remained fixed for the next inversion. Finally, the upper mantle velocities were inverted using P_n phases. The applied hybrid scheme uses both first and second arrivals to constrain the velocity model, without the need to disregard for example secondary arrivals such as lower crustal P_g, phases which become secondary arrivals where P_n arrivals overtake P_g.

[12] Horizontal grid spacing of the model used for the velocity inversion is 0.5 km, whereas the vertical grid spacing is varied from 0.05 km at the top of the model to 0.5 km at the bottom.

Depth nodes defining the reflectors are spaced at 2 km. We used horizontal correlation lengths ranging from 2 km at the top to 10 km at the bottom of the model, and vertical correlation lengths varying from 0.4 km at the top to 2.5 km at the bottom. Depth and velocity nodes are equally weighted in the joint refraction and reflection traveltime inversion.

4.1. Sedimentary Section Tomography

[13] Seaward from the trench, the basement was derived by picking and converting the vertical incidence reflections from two-way-time (TWT) data to depth using a constant velocity of 1.7 km/s. Approaching the trench (up to profile distance km 200), a 2-km deep trench basin has been developed with incoming pelagic sediments and turbidites (Figure 2b). Here, refracted P_s phases and reflected P_bP phases (Figure 3e) were used to invert the velocity structure of the sediments in the trench and the top of the oceanic crust. The starting model for the sedimentary trench fill and lower continental slope is shown in Figure 4a and was set up using the semi forward modeling approach of *Zelt and Smith* [1992]. The starting model includes the known bathymetry; the velocity at the top of the sedimentary layer is set to 1.7 km/s. Below the seafloor the velocity varies depending on the depth using a constant vertical velocity gradient of 1 s^{-1}. The starting reflector is directly computed by converting the TWT data of the corresponding basement reflector to depth. For this reference model, the initial root-mean square (RMS) traveltime misfits for P_s and P_bP are 407 ms and 567 ms, respectively. As the crustal phases were omitted in this step, the input model still contains sedimentary velocity below the sediment-crust boundary (Figure 4a).

[14] Tests with several starting models converge to nearly the same final model. In order to study the accuracy of the final model, we employed the Monte Carlo method [e.g., *Korenaga et al.*, 2000]. The uncertainty of a nonlinear inversion can be expressed in terms of the posterior model covariance matrix [e.g., *Tarantola*, 1987], which can be approximated by the standard deviation of a large number of Monte Carlo realizations assuming that all the realizations have the same probability [e.g., *Tarantola*, 1987]. The uncertainty estimated by this method should be interpreted as the uncertainty for our model parameters (i.e., starting velocity model and smoothing constraints). The procedure to estimate velocity uncertainties consisted of randomly perturbing velocities of our reference model (Figure 4a). We generated 100 random initial velocity models by adding smooth perturbations randomly distributed (maximum velocity perturbations of ±0.1 km/s at the top and ±0.4 km/s at the bottom of the model, with wavelength perturbations of 5 km horizontally and 0.5 km vertically). The basement reflector depth was found by converting the TWT data of the reflector into depth using the velocity distribution of every initial model. In addition to the perturbed reference models we produced 100 so-called noisy arrival time sets constructed by adding random phase errors (±50 ms) and common receiver errors (±50 ms) to the original data set [*Korenaga et al.*, 2000]. Then we performed a tomographic inversion for each velocity model with one noisy data set, in order to estimate not only the dependence of the solution on the reference model but also the effect of phase arrival time picking errors. The mean deviation of all realizations of such an ensemble is considered to be a statistical measure of the model parameter uncertainties [e.g., *Tarantola*, 1987]. All of the Monte Carlo inversions converged in less then 10 iterations to $\chi^2 = 1$, where χ^2 is the normalized sum of the RMS misfits divided by the corresponding picking uncertainties; a value of 1 means that the model error is equal to the data uncertainty. Figure 4b shows the average model from the 100 final models. The RMS error was reduced to ∼50 ms for refractions and ∼55 ms for reflections. Figure 4c shows the derivative weight sum (DWS), which is a statistical parameter indicating the model resolution and ray density. The standard deviation of the calculated velocities for most of the model is below 0.1 km/s and for the reflector depth <0.1 km, except at the eastern edge of the model (Figure 4d) where the velocity uncertainty increases to values larger than 0.2 km/s and for the depth uncertainty to values of ∼0.3 km due to the reduced data coverage.

4.2. Oceanic Crust Tomography

[15] For the determination of the crustal part of the velocity model we held the previously determined sedimentary section fixed by using spatial damping [*Korenaga et al.*, 2000]. We inverted the oceanic crust by including all crustal phases (first and later arrivals) to their maximum offset, and the depth of the floating reflector (Moho) was identified using the mantle phases P_mP simultaneously in the tomographic inversion [*Korenaga et al.*, 2000]. As with the inversion of sedimentary layer, we use the Monte Carlo scheme for determining the

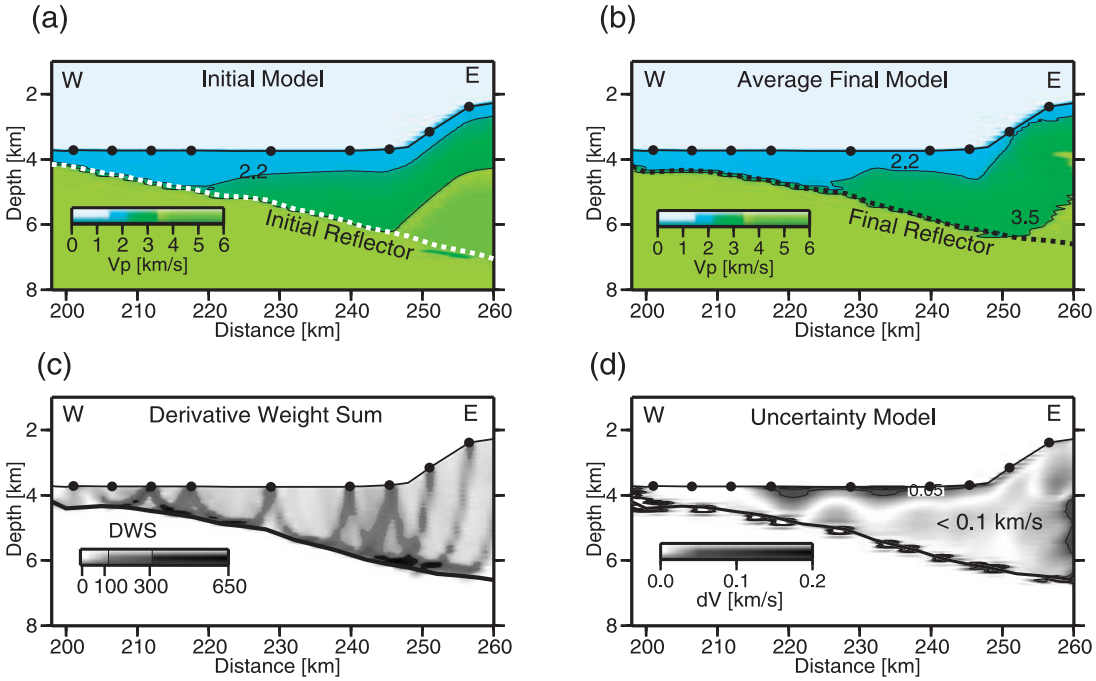

Figure 4. Result of sedimentary tomographic inversion using P_s and P_bP phases, and reflection data. (a) Initial velocity model used as a reference for the Monte Carlo analysis and for velocity inversion. (b) Final average model of the Monte Carlo ensembles. (c) Derivative Weight Sum (DWS) for rays traveling throughout model shown in Figure 4b. (d) Velocity depth uncertainty model after Monte Carlo type realizations.

crust velocities and thicknesses, and therefore a suite of starting models was required.

4.2.1. Reference Model

[16] The 2-D starting velocity models were obtained by hanging 1-D crustal velocity profiles beneath the basement (see Figure 5c). The reference 1-D velocity depth model was composed of oceanic upper crust (layer 2) and the lower crust (layer 3). Minimum values for top, mid, and bottom velocities were 3.0, 6.0, and 6.5 km/s, while corresponding maximum values were 5.0, 7.0, and 7.5 km/s, respectively. The upper crustal thickness could vary from 1 to 3 km, and the lower crustal thickness could vary from 3 to 5 km. The initial geometry of the Moho boundary was chosen as the sum of the obtained smoothed basement geometry in the previous sedimentary modeling and a given crustal thickness, which allowed variations between 4 and 8 km. Different tests showed that variation of the starting model within this model space did not affect significantly the solution. Figure 5a shows the final velocity model derived by averaging all Monte Carlo ensembles.

4.2.2. Model Uncertainty, Monte Carlo–Type Analysis

[17] Velocity and Moho-depth uncertainties of the model parameters in the oceanic plate were estimated by performing a Monte Carlo–type analysis [e.g., *Tarantola*, 1987], as we described above. Figure 5c shows the area covered for the 100 initial two-layer crustal velocity profiles and the 100 starting Moho reflectors underneath the basement.

[18] Initial RMS traveltime misfits were generally higher than 900 ms, and χ^2 was initially greater than 100. The stopping criterion for each inversion was $\chi^2 \sim 1.0$, which was reached typically after 5 iterations. Using the 100 realizations, the final average crustal velocity model and its standard deviation were computed (Figure 5d). The standard deviation of the velocities is lower than 0.1 km/s in the upper crust and the main part of the lower crust as well, increasing to values of 0.1–0.15 km/s in the deepest region of the lower crust. Velocity and Moho depth uncertainties are larger at the western edge of the model where the ray coverage is poor. Moho depth uncertainties in the middle of the model are as low as 0.15 km and reach 0.4 km at

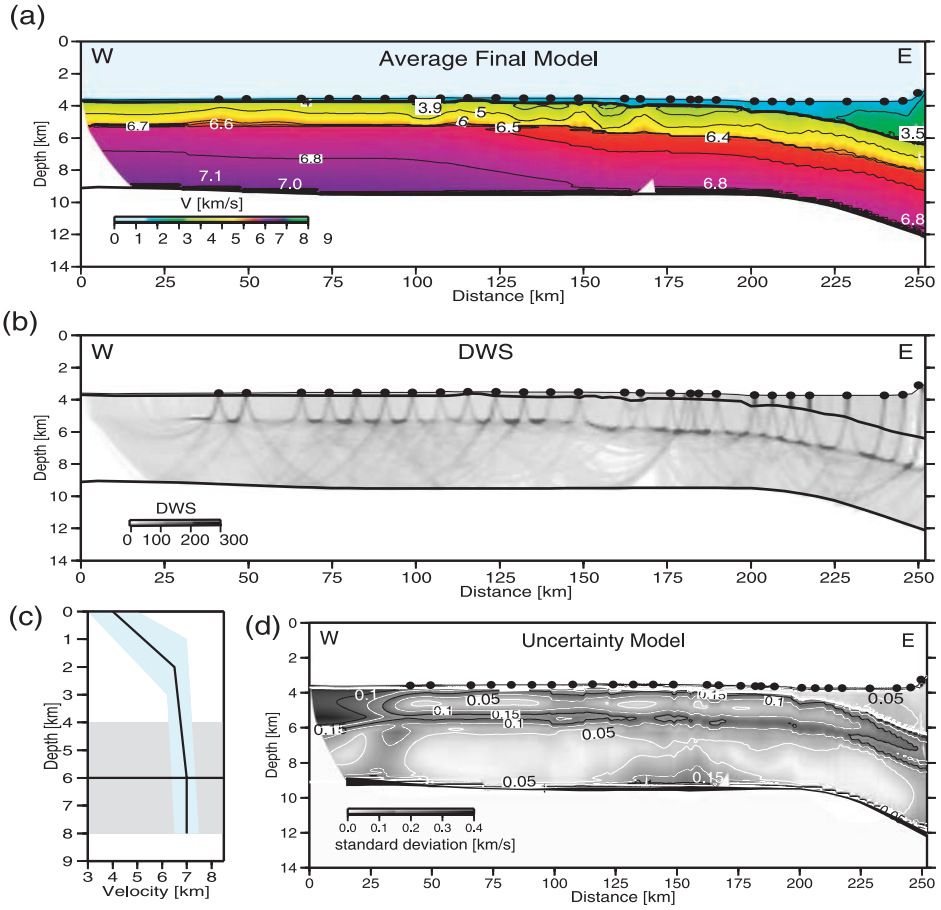

Figure 5. Result of crustal tomographic inversion using P_g and P_mP phases. (a) Final velocity model derived by averaging all Monte Carlo ensembles. (b) Derivative weight sum. (c) Range of parameters for Monte Carlo ensembles. A starting model consists of a 1-D crustal velocity profile; the Moho depth is the sum of the previously obtained smoothed basement and a given crustal thickness. Gray and light blue regions show possible variations in Moho depth and velocity randomization, respectively. (d) Corresponding standard deviation for velocity and depth nodes; contour interval is at 0.05 km/s.

the edges of the velocity model. At the trench, velocities and Moho depth are well constrained with the inclusion of stations on the continental slope [*Scherwath et al.*, 2006b]. The DWS for the model is shown in Figure 5b, which shows excellent ray coverage.

4.2.3. Resolution Test

[19] To check the resolvability of the obtained velocity model, in particular the anomalous low-velocity zones in the trench–outer rise region (Figure 5a), we have created a synthetic model consisting of four sinusoidal anomalies located in the oceanic crust (see Figure 6a), which are superimposed onto the final average velocity model. The maximum amplitude of each Gaussian anomaly is ±6% (Figure 6). Synthetic traveltime data with the same source-receiver geometry as in the real data set have been generated with the perturbed model, and they were inverted using an initial unperturbed model to see how well given perturbations are recovered. The recovery model is plotted in Figure 6b, which was gained after 3 iterations. The result shows that position, shape and amplitude of the velocity anomalies are reasonably well recovered within the uncertainty limits. Despite a certain deterioration in the shape of the anomalies, the result indicates that the geometry and instrument spacing yields a sufficiently high resolution for these structural anomalies, discerning between positive and negative variations along the oceanic crust. The tomographic inversion scheme used here is able to resolve structures with size and amplitude similar to the normal and low-velocity zone at this depth range. This shows that the crustal velocity reduction of the oceanic crust when approaching the trench

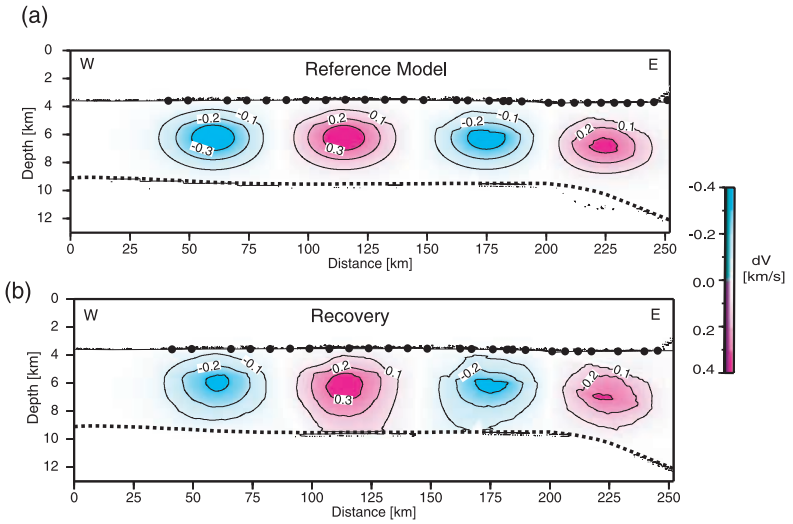

Figure 6. Results of resolution test. (a) Synthetic reference velocity model, consisting of three single sinusoidal anomalies superimposed onto the final velocity model of Figure 5a. (b) Recovery obtained after four iterations.

shown in Figure 5a is not an artifact of the seismic tomographic inversion procedure but a real feature.

4.3. Upper Mantle Tomography

[20] For the subsequent tomographic inversion of the mantle refraction P_n, a "layer-stripping" procedure was chosen, preserving the structural and velocity information above the Moho interface gained before. For the Monte Carlo inversion approach, we constructed several initial models by varying the uppermost mantle velocity between 7.5 to 8.5 km/s and the mantle velocity gradient between 0 and 0.04 s^{-1} respectively. The final average model and its uncertainties are plotted in Figure 7. The results exhibit a clear trend of velocity-reduction toward the trench, which is well correlated with the location of the outer rise but landward of the crustal velocity reduction. Uncertainties of the upper mantle velocity in the outer rise region range between 0.1–0.2 km/s and are well constrained in the seaward part (~0.1 km/s) where the plate geometry is relatively flat and the sediments are thin.

[21] To survey the robustness of our tomographic results, we conducted independent forward modeling seeking a minimum-structure model that satisfies the data. Model features common to the tomographic and forward-modeling output may be assessed without using subjective a priori information [e.g., *Zelt and Smith*, 1992]. We studied uppermost mantle velocity and different velocity gradients by keeping the structural and velocity information above the Moho interface gained for the crustal tomography (Figure 5a). Figure 8a shows the record section of OBH 68, which displays an example of the onset of the P_g, P_mP and P_n phases. "Normal" crustal velocities fit the crustal phases well, and the best-fitting uppermost mantle velocity is about 8.3 km/s. A comparison with a reduced upper mantle velocity of 8.0 km/s produces a large P_n traveltime misfit (Figure 8a), and so we conclude that the seismic data can only be explained with uppermost velocities as fast as 8.3 km/s. Toward the trench the situation changes; a "delay" of P_n arrivals is observed (Figure 8b). These delayed P_n arrivals are already apparent in most of the trenchward branches of seismic stations. A large amount of the total delay in P_n arrivals can be attributed to the thick sedimentary sequence, which covers the deflected downgoing plate (see Figure 4b). However, as our previous sedimentary tomography constrains the sediment structure, a remaining delay of 150 ms is still required to fit P_n arrivals within the uncertainty of the picked arrivals. A better P_n traveltime fit occurs with uppermost mantle velocities ranging between 7.7–8.0 km/s. We also plotted the predicted traveltimes for P_n with an uppermost mantle velocity of 8.2 km/s; the arrivals are predicted up to 150 ms earlier than observed (Figure 8b). In conclusion, the high-quality P_n phases clearly define a reduction of upper mantle velocities toward the trench.

5. Discussion

[22] The data presented in this paper show systematic changes of crustal and upper mantle seismic

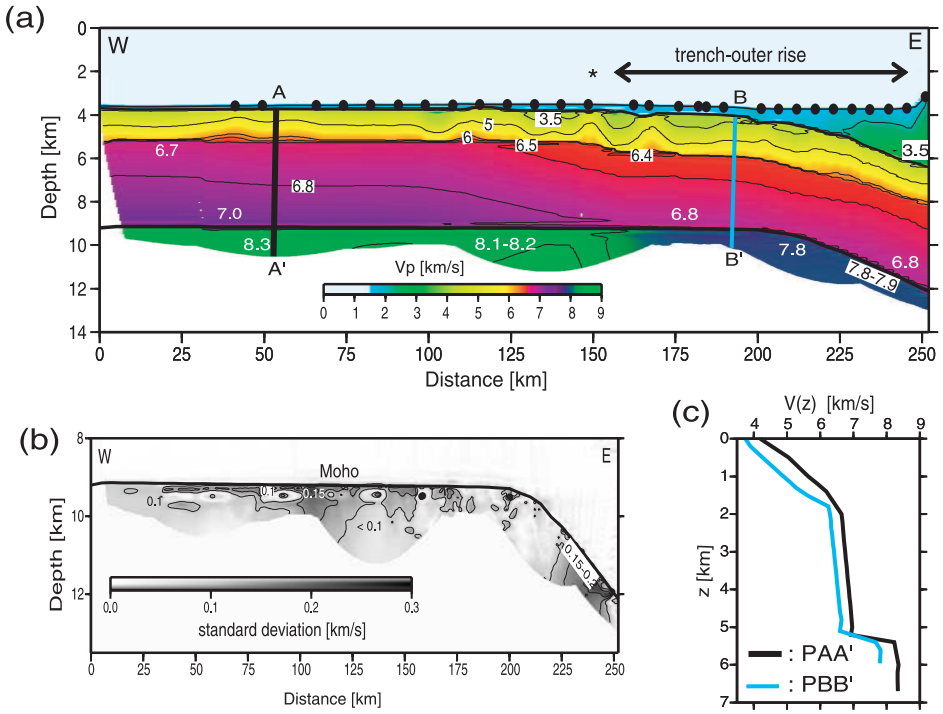

Figure 7. Result of mantle tomographic inversion using refracted P_n phases. (a) Final velocity model derived by averaging all Monte Carlo ensembles (see text for details). (b) Corresponding standard deviation for upper mantle velocity model; contours are drawn at 0.05 km/s interval. Velocity uncertainty is higher between x = 220–250 km below the thick sediments at the trench. (c) Comparison of velocity depth structure for extracted profile from our velocity model shown in Figure 7a. Black line shows velocity structure *V*(*z*) away from the trench, and blue line shows *V(z)* beneath the trench–outer rise.

structure in the form of velocity reduction in the oceanic Nazca plate while it approaches the Chile trench. In this section, we discuss the transition from "normal" to deformed and altered oceanic subducting lithosphere and its possible causes within the geodynamic framework.

5.1. Seismic Structure of the Oceanic Lithosphere

5.1.1. Sediments and Basement Topography

[23] Seaward from the trench (>200 km) the southern Nazca plate is covered by a thin sequence of pelagic and hemipelagic sediments (<150 m). Here, high-resolution multibeam bathymetric mapping shows the typical topographic pattern of the tectonic fabric formed at the spreading center, which is obscured toward the trench due to turbidites deposits (Figure 2b). From profile km x ~ 50 to 200, turbidites fill the half-graben structure and overlay pelagic sediments, forming a mix-sedimentary sequence of 200–400 m thickness. Further to the east (in the trench basin), the sedimentary-cover becomes thicker, resulting in a total thickness of ~2.000 m (Figure 4b). Trench sediments were mainly delivered during the Pleistocene glaciation with a rapid sedimentation rate [*Bangs and Cande*, 1997]. At the bottom of the trench basin, compressional velocities of 3.0–3.5 km/s were detected at 2 km-depth below seafloor. These velocities are because of compaction processes and the increase of sediment size from top to bottom (graded bedding), associated to sedimentary deposit events.

[24] The basement topography is in general rough, and it is characterized by the presence of outcrops of basement highs (Figure 2a). In the outer-rise (x ~ 150 km), and approximately 5 km to the north of the seismic profile a basement outcrop rises ~200 m above the surrounding seafloor (Figure 9a), while its associated basaltic edifice rises ~400 m above regional basement. Ten kilometers to the north of this basement outcrop, several abyssal hills generated at the spreading

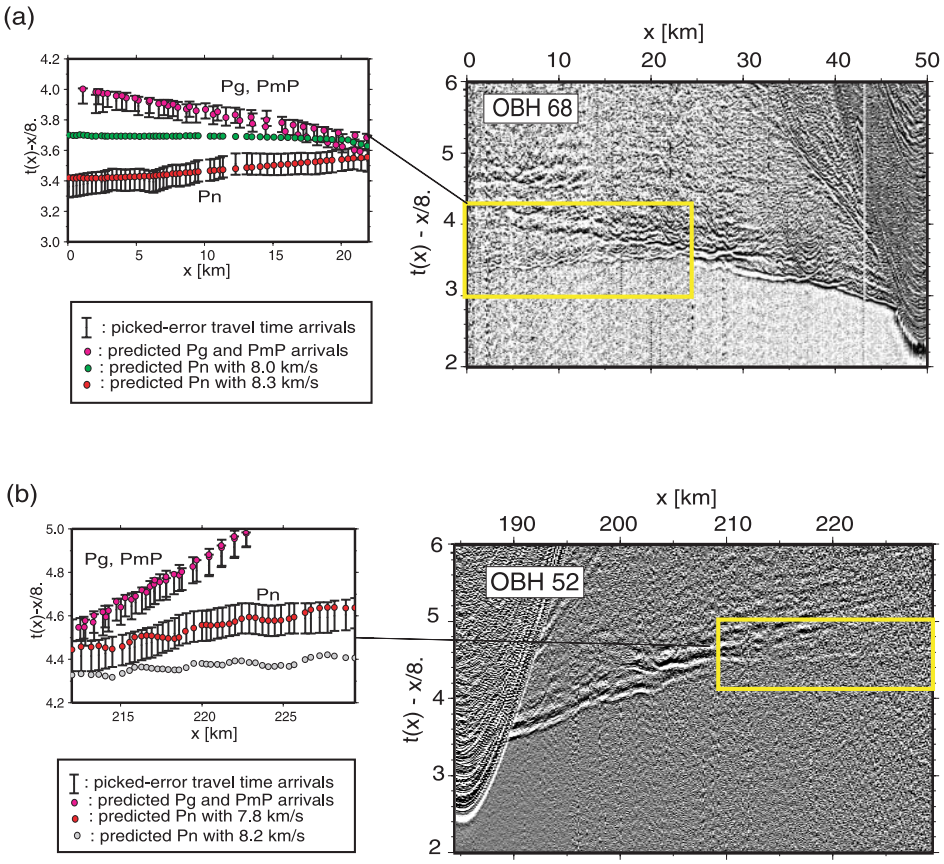

Figure 8. Detailed forward analysis of P_n traveltimes for (a) oceanward branch of OBH 68 and (b) trenchward branch of seismic record section of OBH 52. Predicted P_g and P_mP arrivals are based on the final crustal model shown in Figure 5a. (a) P_n oceanic phases can only be predicted with values as fast as 8.3 km/s (red dots); uppermost velocities values of 8.0 km/s produce a misfit >250 ms (green dots). (b) P_n arrivals are predicted up to 150 ms earlier than observed using an uppermost velocity of 8.2 km/s (gray dots); a better P_n traveltime fit occurs with uppermost mantle velocity of 7.8 km/s (red dots).

center with pervasive faulting and large offsets strike approximately parallel to the trench axis (Figure 2a). This area is characterized by pervasive normal faults exposing basement caused by plate bending. Southward and trenchward of the seismic profile, this fault pattern is not visible on the multibeam bathymetry owing to the thicker sedimentary cover. Under the trench fill, however, multichannel data reveal that as the plate approaches the trench, basement topography becomes rougher and the oceanic crust is probably pervasively fractured due to bending-related faulting (Figure 2b).

5.1.2. Oceanic Crust

[25] Two distinct zones of the oceanic crust can be identified in the final model: (1) the oceanward section, away from the trench, and (2) the trench–outer rise region just prior of the subduction of the oceanic plate. Figure 7c compares the velocity structure beneath the sediments for well resolved velocity-depth profiles of zones 1 and 2.

[26] In the oceanward section of the velocity model, the velocity structure below basement roughly follows the basement topography. Velocities in the ~1.7 km thick layer are between 4.0–4.2 km/s at the top and ~6.6 km/s at the bottom and correspond to oceanic layer 2; a typical sequence of extrusive basalts on top of a sheeted dike complex and high velocity gradient of about 1.4 s^{-1}. Both seismic velocity and gradient are similar to the seismic structure obtained off-axis in the upper crust of the southern East Pacific Rise [*Grevemeyer et al.*, 1998]. These values are in good agreement with mature oceanic crust sufficiently far way from the ridge crests so that strong hydrothermal circulation has largely ceased [*Grevemeyer et al.*, 1999]. Layer 2 overlies a ~3.6 km thick layer with velocities increasing from 6.6 km/s to ~7.0–7.1 km/s. This

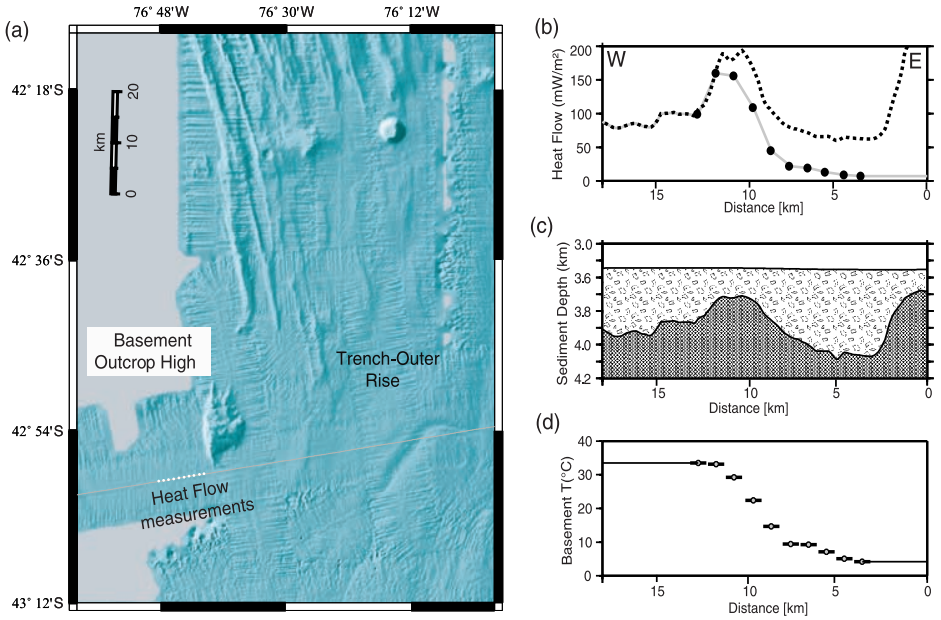

Figure 9. (a) Location of heat flow stations along seismic profile. (b) Heat flow measurements (black dots). Predicted heat flow values using a basement temperature of T_b = 40°C (dotted line). Predicted heat flow values incorporating hydrothermal cooling (gray line). (c) Basement topography obtained from seismic reflection data. (d) Temperature distribution at the basement used in our heat flow model with cooling. For Figures 9b, 9c, and 9d, distance is measured from the location of the basement outcrop high.

seismic structure is typical of oceanic layer 3 normally associated with gabbro and layered gabbro rocks (layer 3A and 3B) [e.g., *Vera et al.*, 1990]. The velocity range of 6.6–7.1 km/s is consistent with lower crust relative anhydrous in composition, which is typical for oceanic crust formed at fast spreading ridges [e.g., *Carbotte and Scheirer*, 2004; *Karson*, 1998]. The bulk porosity of the crust should be rather low due to the closure of cracks and fissures by hydrothermal mineralization [e.g., *Grevemeyer and Bartezko*, 2004].

[27] Approaching the trench, velocities for the igneous crust start to decrease 100 – 150 km from the deformation front (Figure 5a). The uppermost crustal velocities decrease to values lower than 3.7 km/s (Figure 7c), which are much lower than typical uppermost layer 2 velocities of mature oceanic crust (>4.5 km/s) [*Carlson*, 1998; *Grevemeyer and Bartetzko*, 2004]. Lowermost crustal velocities decrease to values lower than 6.9 km/s (Figure 5a), implying the likely presence of hydrous minerals, such as chlorite and amphibolites [e.g., *Hess*, 1962; *Christensen and Salisbury*, 1975]. The decrease of velocities is accompanied with an increase in roughness of the basement topography, and probably coincides with activation of new cracks and normal extensional faults induced by plate bending [e.g., *Ranero and Sallares*, 2004]. This process suggests a significant alteration of the porosity structure of the entire subducting oceanic crust.

[28] Moho reflections (P_mP) constrain the transition from "crustal" gabbros to "mantle" ultramafic rocks, which occurs at ~5.3 km depth below the top of the basement. Crustal thickness is therefore less than the average value of 6.48 ± 0.75 km reported by *White et al.* [1992] for Pacific crust younger than 30 Ma. *McClain and Atallah* [1986], however, estimated that Pacific crust averages 5.67 ± 0.88 km for crust of the same age, and *Walter et al.* [2000] and *Grevemeyer et al.* [2007] found in more recent studies that crust of the Cocos plate is 5.0–5.5 km thick.

5.1.3. Uppermost Oceanic Mantle

[29] Seaward from the trench, compressional velocity of 8.3 km/s was detected in the uppermost 2–2.5 km of the mantle (Figure 7a). Typical mature oceanic mantle velocities are faster than 8.1 km/s, which is usually associated to an anhydrous composition of mantle peridotite [e.g., *Peacock*, 1990]. Thus oceanic Nazca plate approaches the subduction zone with a mantle comparatively undeformed and dry (Figure 7a). Closer to the trench, however, a progressive velocity-reduction in the upper mantle

occurs. The velocity reduction is visible ~80 km from the deformation front (Figure 7a), and they decrease to minimum values of ~7.8 km/s, which is significantly lower than the velocity of mantle peridotite (>8.1 km/s). P_n phases image only the first ~2 km of the uppermost mantle in the outer rise area (Figure 7a). Thus the maximum depth of possible hydration in the mantle remains unconstrained.

[30] It has been documented that the uppermost mantle velocity reduction is even larger in poorly sedimented margins. In north Chile, for example, upper-mantle velocities in the trench–outer rise area reach values as low as 7.6 km/s [*Ranero and Sallares.*, 2004]. Offshore of Costa Rica, seismic velocities under the trench at the Moho are even lower (7.3–7.4 km/s), with velocities increasing to ~7.5–7.8 km/s at about 3–4 km below the Moho [*Grevemeyer et al.*, 2007]. Offshore of south central Chile, upper mantle velocity reduction is slightly lower and solely restricted to the trench–outer rise area (Figure 7a), where bending-related faulting is suggested to lead to hydration of the upper mantle [*Ranero et al.*, 2003]. Since water is required to alter mantle peridotite to serpentinite, pervasive fracturing of the entire crust is suggested for the lithosphere entering the Chilean subduction zone offshore Chiloe Island.

5.2. Water Pathways

[31] The efficiency of fluid percolation depends on the sedimentary thickness and faulting history. Faults constitute the possible water pathways but they can be blocked by insulating sediments. Therefore slab hydration prior to subduction is believed to be largest where outcropping basement relief facilitates the flow of seawater into the crust [*Grevemeyer et al.*, 2005]. The abyssal hill fabric inherently related to the formation process of the oceanic lithosphere at the mid-ocean ridge is well imaged just 5 km to the north of the seismic line (Figure 2a). Therefore reactivation of fractures by bending-related normal faulting in this region might be an important mechanism for plate hydration.

[32] High-resolution seismic data provides evidence for some extensional faults reflected by offsets in the trench–outer rise region (Figure 2b), suggesting the trenchward increase of fracturing intensity. This indicates that the bending-related faulting is active in the outer rise, and it fractures the oceanic crust beneath the sedimentary bed. High-resolution multibeam bathymetry shows, though, that surface-cutting faults are not visible on the seafloor along this profile (Figure 2a). As the insulating sediments are several hundreds of meters thick (Figure 2b) an efficient inflow of seawater is unlikely to explain the reduced velocities in the outer rise. However, the onset of velocity reduction in the oceanic crust is well correlated with the location of an outcropping basement high or seamount (Figures 7a and 9), suggesting a relationship between plate hydration and basement outcrop. Seamounts or basement highs provide the necessary pathways to move huge volumes of fluid through oceanic crust over large distances, even when the crust is insulated by thick sediments [*Fisher et al.*, 2003a, 2003b].

[33] In order to study the hydrothermal activity in the outer rise, we have directly measured heat flow values on the outer bulge offshore of Chiloe Island [*Flueh and Grevemeyer*, 2005]. Figure 9a shows the location of 10 heat flow stations immediately at the seaward flank of the basement outcrop (see also the bathymetry in Figure 2a). The heat flow values decrease from 100–150 to ~7 mW/m^2 over a distance of less than 10 km toward the trench (Figure 9b). We computed two predicted heat flow models using two different temperature distributions at the top of the igneous basement. In the first model basement temperature is isothermal. In the second model basement temperatures varies as a function of distance from the basement high and hence mimics cooling by inflow of cold seawater. Crucial parameters are the temperature at the basement T_{bas} and at the seafloor T_{sea}, and the thermal conductivity structure k between the basement and the seabed. We use a linear temperature gradient and the simple conductive heat transport relation

$$q = k\ dT/dz$$

where q is the heat flow, $dz = z_{bas} - z_{sea}$ is the thickness of the sediments, and $dT = T_{bas} - T_{sea}$. The sedimentary thickness comes directly from the high-resolution reflection data and is plotted in Figure 9c. The seafloor temperature is assumed T_{sea} = 0°C, and thermal conductivity k was measured in situ. Testing with different $T_{bas}(x)$ distributions, the extreme low values toward the trench can only be predicted by the cooling model (Figures 9b and 9d). This finding suggests a very efficient inflow of cold seawater into the oceanic crust through the basement outcrop feature located just 5 km north of the profile.

[34] The flanks of the high outcrop basement probably act as an important and primary entry of cold seawater into the igneous oceanic crust. This process accompanied by the opening of new cracks and activation of extensional faults due to bending-related faulting increases the permeability and hence facilitates a deeper fluid inflow, probably, reaching mantle depths, as supported by our tomographic results (Figure 7a). We see a number of other mounds and basement ridges imaged in the multibeam bathymetry to the north of the profile, which may act as recharge and discharge sites and therefore fuel a hydrothermal circulation in the outer rise. Cold seawater might be transported laterally between separated basement outcrops for distances of more than 50 km [*Fisher et al.*, 2003a], which implies that fluids may circulate through most of the studied trench–outer rise area. Here, bending-related faulting might increases the permeability of the oceanic crust, and consequently facilitates and reactivates hydrothermal circulation.

[35] Moreover, the incoming plate may laterally carry water already percolated in the oceanward part of the outer rise (70–40 km from the trench axis), where plate bending is strongest, igneous basement is more exposed, and due to a higher water/rock ratio hydration might be more vigorous. In this part of the outer rise, the sedimentary thickness is comparable with the outer rise in Middle America (200–400 m thick), which is highly hydrated [*Ranero et al.*, 2003]. Once cold seawater is stored in cracks and/or faults and faulting continues toward the deformation front, water trapped within the crust may migrate deeper where larger faults cut into the mantle.

5.3. Volatiles Stored in the Oceanic Subducting Lithosphere

[36] The amount of volatiles stored in the subducting oceanic lithosphere consists mainly of three components: volatiles stored (1) in subducting sediments, (2) in the oceanic crust, and (3) in the oceanic mantle. Recent studies, however, suggest that most of the bound water enters subduction zones within the oceanic crust and mantle [*Peacock*, 1990; *Ranero et al.*, 2003].

[37] The observed crustal velocity reduction beneath the trench–outer rise is caused in part by cracks and fissures induced by plate bending. The similar trend for upper and lower crustal velocities has been observed in the northern Chile trench, which was explained as consequence of fracturing rather than hydration [*Ranero and Sallares*, 2004]. The amount of chemically bound water in the crust is therefore not straightforward to estimate by the magnitude of velocity reduction. *Peacock* [1990] concludes from chemical analysis of drill cores of oceanic crust that a 2.5-km-thick basaltic layer contains in average 2 wt.% H_2O and ~0.1 wt.% CO_2, and a 3- to 5-km-thick oceanic gabbro layer contains roughly 1% H_2O and ~0.1 wt.% CO_2. *Hacker et al.* [2003] calculated a maximum water content of 1.3 wt% H_2O for partially hydrated lower oceanic crust based on a global compilation of physical properties of minerals. *Carlson* [2003] shows that, based on the modal mineralogy and seismic properties of oceanic diabase and gabbro samples, gabbros with velocities typical for the lower oceanic crust (6.7–7.0 km/s) already contain a mean water content near 0.5 wt%. This value could be much larger if lower oceanic crust has been altered by tectonic processes, as is probably the case in our study area.

[38] Quantifying the amount of serpentine in subducting oceanic mantle is also difficult because relatively modest amounts of serpentine can represent a major H_2O input into the subduction factory [*Peacock*, 2001]. Following *Carlson and Miller* [2003], an approximate formula to estimate water content in the partially-serpentinized peridotites is $w(\%) \approx -0.33\Delta V$, where w is the water content (in weight percentage) and ΔV is the percent difference between the observed velocity and the velocity in unaltered peridotite. The upper mantle P wave velocity in our study region ranges between 7.8 to 8.3 km/s, corresponding to serpentinite contents of roughly 0 to 9%; and the corresponding range of water contents of 0 to 3.0% (0 to 4 moles/m^3). These values are lower compared to estimates in Central America (>20% of serpentinization) [*Ranero et al.*, 2003], the erosional margin in northern Chile (~17% of serpentinization) [*Ranero and Sallares*, 2004], and offshore Costa Rica (10–25% of serpentinization) [*Grevemeyer et al.*, 2007]. Nevertheless, the total amount of hydration and thus the total volume of fluids entering the subduction zone in south central Chile should be larger than the 9% bound in the upper mantle because of the volatile stored in the entire oceanic crust plus subducting sediments. Moreover, this degree of hydration can be even larger if the oceanic plate continues to hydrate during subduction [*Ranero et al.*, 2003].

6. Conclusions

[39] Joint inversion of seismic refraction and wide-angle data offshore of south-central Chile yields

the P wave velocity structure of the subducting oceanic Nazca plate. This information and the tectonic features obtained from high-resolution seismic data, multibeam bathymetry and heat flow measurements suggest that the structure of the incoming plate changes systematically within ~120 km off the trench axis as the lithosphere approaches the deep-sea trench. This work leads to the following conclusions:

[40] 1. The 2-D velocity model derived from tomographic traveltime inversion consist of a ~5.3 km thick oceanic crust and shows a classical mature fast spreading P wave velocity structure in the seaward part outside of the influence of plate bending at the trench–outer rise. Seismic analysis of P_n arrivals reveals fast uppermost mantle velocities of ~8.3 km/s, >120 km seaward of the trench. The velocity structure found in this zone indicates that the oceanic lithosphere is relatively dry and undeformed.

[41] 2. Approaching the Chile trench, seismic velocities decrease, indicating an evolutionary process changing the structure of the lithosphere, likely to be related to an increase in fracture porosity and hydration of both the oceanic crust and the uppermost mantle. Reduced velocities are only located in the trench and outer-rise area. The decrease of velocities is accompanied by an increase of basement-relief roughness and also by the amount of stress induced by the plate bending.

[42] 3. In spite of the thick sedimentary blanket on the incoming plate, an efficient inflow of cold seawater into the oceanic crust through outcropping basement highs or seamounts is supported by anomalously low heat flow values, which are spatially well correlated with the onset of velocity reduction in the crust and upper mantle. Cold seawater might be laterally transported between high basement outcrops over large distances (>50 km) in the vicinity of the trench–outer rise area. This primary water pathway could extend to mantle depth through bending induced trench parallel normal faults, and thus cause a hydration of the upper mantle.

[43] 4. Assuming that the mantle velocity reduction is produced only by hydration, serpentinization of the uppermost mantle from the outer rise to the trench axis is ~9% in the uppermost 2 km of the mantle, where seismic data provide enough resolution. This degree of hydration in the uppermost mantle is about 10% less than observed in poorly sedimented margins.

[44] In summary, seismic data of high resolution reveal a clear alteration of the oceanic lithosphere at the outer rise just prior to its subduction, showing that the alteration occurs where strong plate bending is likely to modify the large scale porosity and permeability structure of oceanic lithosphere, and simultaneously nurtures the migration of cold seawater through crustal faults down to mantle depth, resulting in hydration of both oceanic crust and upper mantle. Infiltration of cold seawater, and consequently hydration of the subducting oceanic lithosphere may also occur at heavily sedimented trenches through high basements outcrops where igneous crust is exposed.

Acknowledgments

[45] We are grateful to Masters Kull and Mallon and their officers and crew of R/V *Sonne* and all scientists who assisted in data collection during cruise SO181. This is publication GEOTECH-276 of the R&D-Programme GEOTECHNOLOGIEN funded by the German Ministry of Education and Research (BMBF) and German Research Foundation (DFG), grants 03G0181A, 03G0594E, and 03G0594F. One of the authors (E.C.-R.) gratefully acknowledges a scholarship granted by the German Academic Exchange Service (DAAD).

References

Alt, J. C., J. Honnorez, C. Laverne, and R. Emmermann (1986), Hydrothermal alteration of a 1 km section through the upper oceanic crust, Deep Sea Drilling Project Hole 504B: Mineralogy, chemistry, and evolution of seawater-basalt interactions, *J. Geophys. Res.*, *91*, 10,309–10,335.

Angermann, D., J. Klotz, and C. Reigber (1999), Space-geodetic estimation of the Nazca–South America Euler vector, *Earth Planet. Sci. Lett.*, *171*(3), 329–334.

Bangs, N. L., and S. C. Cande (1997), Episodic development of a convergent margin inferred from structures and processes along the Southern Chile margin, *Tectonics*, *16*, 489–503.

Bialas, J., and E. R. Flueh (1999), Ocean bottom seismometers, *Sea Technol.*, *40*(4), 41–46.

Carbotte, S., and D. S. Scheirer (2004), Variability of ocean crustal structure created along the global mid-ocean ridge, in *Hydrogeology of Oceanic Lithosphere*, edited by E. E. Davis and H. Elderfield, pp. 128–150, Cambridge Univ. Press, New York.

Carlson, R. L. (1998), Seismic velocities in the uppermost oceanic crust: Age dependence and the fate of layer 2A, *J. Geophys. Res.*, *103*(B4), 7069–7078.

Carlson, R. L. (2003), Bound water content of the lower oceanic crust estimated from modal analyses and seismic velocities of oceanic diabase and gabbro, *Geophys. Res. Lett.*, *30*(22), 2142, doi:10.1029/2003GL018213.

Carlson, R. L., and D. J. Miller (2003), Mantle wedge water contents estimated from seismic velocities in partially serpentinized peridotites, *Geophys. Res. Lett.*, *30*(5), 1250, doi:10.1029/2002GL016600.

Chapple, W. M., and D. W. Forsyth (1979), Earthquakes and bending plates at trenches, *J. Geophys. Res.*, *84*, 6729–6749.

Christensen, D. H., and L. J. Ruff (1983), Outer-rise earthquakes and seismic coupling, *Geophys. Res. Lett.*, *10*, 697–700.

Christensen, N. I., and M. H. Salisbury (1975), Structure and constitution of the lower oceanic crust, *Rev. Geophys.*, *13*, 57–86.

Fisher, A. T., C. A. Stein, R. N. Harris, K. Wang, E. A. Silver, M. Pfender, M. Hutnak, A. Cherkaoui, R. Bodzin, and H. Villinger (2003a), Abrupt thermal transition reveals hydrothermal boundary and role of seamounts within the Cocos Plate, *Geophys. Res. Lett.*, *30*(11), 1550, doi:10.1029/2002GL016766.

Fisher, A. T., et al. (2003b), Hydrothermal recharge and discharge across 50 km guided by seamounts on a young ridge flank, *Nature*, *421*, 618–621.

Flueh, E. R., and J. Bialas (1996), A digital, high data capacity ocean bottom recorder for seismic investigations, *Int. Underwater Syst. Design*, *18*(3), 18–20.

Flueh, E. R., , and I. Grevemeyer (Eds.) 2005. TIPTEQ SONNE Cruise SO-181, from the Incoming Plate to mega Thrust EarthQuakes, *Geomar Rep. 102*, Geomar, Kiel, Germany.

Grevemeyer, I., and A. Bartetzko (2004), Hydrothermal ageing of oceanic crust: Inferences from seismic refraction and bore hole studies, in *Hydrogeology of Oceanic Lithosphere*, edited by E. E. Davis and H. Elderfield, pp. 128–150, Cambridge Univ. Press, New York.

Grevemeyer, I., and W. Weigel (1996), Seismic velocities of the uppermost igneous crust versus age, *Geophys. J. Int.*, *124*, 631–635.

Grevemeyer, I., and W. Weigel (1997), Increase of seismic velocities in upper oceanic crust: The ''superfast'' spreading East Pacific Rise at 14°14′S, *Geophys. Res. Lett.*, *24*(3), 217–220.

Grevemeyer, I., W. Weigel, and C. Jennrich (1998), Structure and ageing of oceanic crust at 14°S on the East Pacific Rise, *Geophys. J. Int.*, *135*, 573–584.

Grevemeyer, I., N. Kaul, H. Villinger, and W. Weigel (1999), Hydrothermal activity and the evolution of the seismic properties of upper oceanic crust, *J. Geophys. Res.*, *104*(B3), 5069–5080.

Grevemeyer, I., N. Kaul, J. L. Diaz-Naveas, H. Villinger, C. R. Ranero, and C. Reichert (2005), Heat flow and bending-related faulting at subduction trenches: Case studies offshore of Nicaragua and Central Chile, *Earth Planet. Sci. Lett.*, *236*, 238–248.

Grevemeyer, I., C. R. Ranero, E. R. Flueh, D. Klaeschen, and J. Bialas (2007), Passive and active seismological study of bending-related faulting and mantle serpentinization at the Middle America trench, *Earth Planet. Sci. Lett*, doi:10.1016/j.epsl.2007.04.013.

Hacker, B. R., G. A. Abers, and S. M. Peacock (2003), Subduction factory: 1. Theoretical mineralogy, densities, seismic wave speeds, and H_2O contents, *J. Geophys. Res.*, *108*(B1), 2029, doi:10.1029/2001JB001127.

Hess, H. H. (1962), History of ocean basins, in *Petrological Studies: A Volume in Honor of A. F. Buddington*, edited by A. E. Engel, H. L. James, and B. F. Leonard, pp. 599–620, Geol. Soc. of Am., Boulder, Colo.

Kanamori, H. (1971), Seismological evidence for lithospheric normal faulting: The Sanriku earthquake of 1933, *Phys. Earth Planet. Inter.*, *4*, 289–300.

Karson, J. A. (1998), Internal structure of oceanic lithosphere: A perspective from tectonic windows, in *Faulting and Magmatism at Mid-Ocean Ridges*, *Geophys. Monogr. Ser.*, vol. 106, edited by W. R. Buck et al., pp. 177–218, AGU, Washington, D. C.

Korenaga, J., W. S. Holbrook, G. M. Kent, P. B. Kelemen, R. S. Detrick, H. C. Larsen, J. R. Hopper, and T. Dahl-Jensen (2000), Crustal structure of the southeast Greenland margin from joint refraction and reflection seismic tomography, *J. Geophys. Res.*, *105*, 21,591–21,614.

McClain, J. S., and C. A. Atallah (1986), Thickening of oceanic crust with age, *Geology*, *14*, 574–805.

Peacock, S. (1990), Fluid processes in subduction zones, *Science*, *248*, 329–337.

Peacock, S. (2001), Are the lower planes of double seismic zones caused by serpentine dyhydration in subducting oceanic mantle?, *Geology*, *29*, 299–302.

Peacock, S. M. (2004), Insight into the hydrogeology and alteration of oceanic lithosphere based on subduction zones and arc volcanism, in *Hydrogeology of Oceanic Lithosphere*, edited by E. E. Davis and H. Elderfield. pp. 659–676, Cambridge Univ. Press, New York.

Ranero, C. R., and V. Sallares (2004), Geophysical evidence for alteration of the crust and mantle of the Nazca Plate during bending at the north Chile trench, *Geology*, *32*, 549–552.

Ranero, C. R., J. Phipps Morgan, K. McIntosh, and C. Reichert (2003), Bending, faulting, and mantle serpentinization at the Middle America trench, *Nature*, *425*, 367–373.

Reichert, C., B. Schreckenberger. and SPOC Team (2002), Fahrtbericht SONNE-Fahrt SO-161 Leg 2&3 SPOC, Subduktionsprozesse vor chile-BMBF-Forschungsvorhaben 03G0161A- Valparaiso 16.10.2001–Valparaiso 29.11.2001, Bundesanst. für Geowissenschaften und Rohstoffe, Hannover, Germany.

Scherwath, M., E. R. Flueh, I. Grevemeyer, F. Tilmann, E. Contreras-Reyes, and R. W. Weinrebe (2006a), Investigating subduction zone processes in Chile, *Eos Trans. AGU*, *87*(27), 265–272.

Scherwath, M., E. Contreras-Reyes, I. Grevemeyer, E. R. Flueh, W. Weinrebe, and the TIPTEQ Working Group (2006b), Structural images of the southern Chile subduction zone system offshore, paper presented at Third EGU General Assembly, European Geosciences Union, Vienna2 -7 April .

Tarantola, A. (1987), *Inverse Problem Theory: Methods for Data Fitting and Model Parameter Estimation*, 613 pp., Elsevier, New York.

Tebbens, S. F., S. C. Cande, L. Kovacs, J. C. Parra, J. L. LaBrecque, and H. Vergara (1997), The Chile ridge: A tectonic framework, *J. Geophys. Res.*, *102*(B6), 12,035–12,060.

Thornburg, T. M., and D. M. Kulm (1987), Sedimentation in the Chile Trench: Depositional morphologies, lithofacies, and stratigraphy, *Geol. Soc. Am. Bull.*, *98*, 33–52.

Thornburg, T. M., D. M. Kulm, and D. M. Hussong (1990), Submarine-fan development in the southern Chile trench: A dynamic interplay of tectonics and sedimentation, *Geol. Soc. Am. Bull.*, *102*, 1658–1680.

van Avendonk, H. J. A., A. J. Harding, and J. A. Orcutt (1998), A two-dimensional tomographic study of the Clipperton transform fault, *J. Geophys. Res.*, *103*, 17,885–17,899.

Vera, E. E., J. C. Mutter, P. Buhl, J. A. Orcutt, A. J. Harding, M. E. Kappus, R. S. Detrick, and T. M. Brocher (1990), The structure of 0- to 0.2-m.y.-old oceanic crust at 9°N on the East Pacific Rise from expanded spread profiles, *J. Geophys. Res.*, *95*(B10), 15,529–15,556.

Villinger, H., I. Grevemeyer, N. Kaul, J. Hauschild, and M. Pfender (2002), Hydrothermal heat flux through aged oceanic crust: Where does the heat escape?, *Earth Planet. Sci. Lett.*, *202*, 159–170.

Voelker, D., M. Wiedicke, S. Ladage, C. Gaedicke, C. Reichert, K. Rauch, W. Kramer, and C. Heubeck (2006), Latitudinal variation in sedimentary processes in the Peru-Chile Trench off Central Chile, in *The Andes—Active Subduction Orogeny*, *Frontiers in Earth Sciences*, edited by O. Oncken et al., pp. 193–216, Springer, Berlin.

Walter, C., E. R. Flueh, C. R. Ranero, R. von Heune, and W. Strauch (2000), Crustal structure across the Pacific margin of Nicaragua: Evidence for ophiolitic basement and a shallow mantle sliver, *Geophys. J. Int.*, *141*, 759–777.

White, R. S., and D. McKenzie (1992), Oceanic crustal thickness from seismic measurements and rare earth element inversions, *J. Geophys. Res.*, *97*, 19,683–19,715.

Wilkens, R. H., G. J. Fryer, and J. Karsten (1991), Evolution of porosity and seismic structure of upper oceanic crust: Importance of aspect ratios, *J. Geophys. Res.*, *96*(B11), 17,981–17,995.

Zelt, C. A., and R. B. Smith (1992), Seismic traveltime inversion for 2-D crustal velocity structure, *Geophys. J. Int.*, *108*, 16–34.